TECHNISCHE UNIVERSITÄT MÜNCHEN
LEHRSTUHL FÜR AERODYNAMIK UND
STRÖMUNGSMECHANIK

Simulation of Complex Turbulent Flows on Cartesian Adaptive Grids

Michael Meyer

Vollständiger Abdruck der von der Fakultät für Maschinenwesen der Technischen Universität München zur Erlangung des akademischen Grades eines

Doktor-Ingenieurs

genehmigten Dissertation.

Vorsitzender:	Univ.-Prof. Wolfgang H. Polifke Ph.D. (CCNY)
Prüfer der Dissertation:	1. Univ.-Prof. Dr.-Ing. Nikolaus A. Adams
	2. Univ.-Prof. Dr.-Ing. Wolfgang Schröder, Rheinisch-Westfälische Technische Hochschule Aachen

Die Dissertation wurde am 14.01.2013 bei der der Technischen Universität München eingereicht und durch die Fakultät für Maschinenwesen am 29.04.2013 angenommen.

“Nichts trägt einen Sinn in sich. Der wirkliche Sinn der Dinge liegt im Gefüge.”

Antoine de Saint-Exupry: Ein Lächeln ist das Wesentliche.

Abstract

The generation of suitable body-fitted grids for Large-Eddy Simulation (LES) of complex flows can be time-consuming and difficult. Contradictory requirements, such as adequate local resolution and minimum number of grid points, can deteriorate the grid quality and therefore adversely affect accuracy and numerical convergence properties. Unstructured grids without rather severe constraints on cell size and aspect ratio, however, are known to be not well suited for time-resolving turbulent flow computations, in particular for LES. An alternative approach is to use Cartesian grids, which also facilitates automatic grid generation and local grid refinement. Cartesian grids imply fewer computational operations per grid point than body-fitted or unstructured grids. On the other hand, bounding surfaces of the flow or immersed obstacles need to be accounted for by mapping the boundaries onto the grid.

For mapping the boundaries onto the grid an immersed interface method is proposed that maintains conservation and second-order accuracy. This Conservative Immersed Interface Method (CIIM) is based on a finite-volume discretization of the incompressible Navier-Stokes equations on a staggered Cartesian grid. A level-set technique is used for description and tracking of the interface geometry, so that an extension of the method to moving boundaries and flexible walls is straightforward. Numerical stability is ensured for small cells by a conservative mixing procedure. Discrete conservation and sharp representation of the fluid-solid interface render the method particularly suitable for LES of turbulent flows.

Accuracy, second-order grid convergence, robustness and computational performance of CIIM are demonstrated for several validation test cases: inclined channel flow, flow over a square cylinder, laminar and turbulent flow over a circular cylinder, as well as turbulent channel flow with periodic constrictions. CIIM in combination with a wall-model is also applied in the investigation of two industrially relevant flows: the flow over the RA16SC-1 3-element highlift airfoil and the flow over the VFE-2 delta wing. To the author's knowledge, these are the first LES to predict the flow for these test cases. The promising results underline the suitability of CIIM for predicting complex turbulent flows in industrial applications.

Contents

List of Figures

List of Tables

Abbreviations

1-D	one-dimensional
2-D	two-dimensional
3-D	three-dimensional
AVT	**A**pplied **V**ehicle **T**echnology
ALDM	**A**daptive **L**ocal **D**econvolution **M**ethod
BC	**B**oundary **C**ondition
BiCGstab	stabilized **Bi**-**C**onjugate **G**radient method
CDS	**C**entral **D**ifference **S**cheme
CFL	**C**OURANT-**F**RIEDRICHS-**L**EWY; COURANT number
CIIM	**C**onservative **I**mmersed **I**nterface **M**ethod
CPU	**C**entral **P**rocessing **U**nit
CTU	**C**onvective **T**ime **U**nit
DLR	**D**eutsches Zentrum für **L**uft- und **R**aumfahrt
DES	**D**etached **E**ddy **S**imulation
DEHS	**D**i-2-**E**thyl**H**exyl-**S**ebacat
DDES	**D**elayed **D**etached **E**ddy **S**imulation
DNS	**D**irect **N**umerical **S**imulation
FDM	**F**inite **D**ifference **M**ethod
FEM	**F**inite **E**lement **M**ethod
FFA	**F**ast **F**OURIER **A**nalysis
FFT	**F**ast **F**OURIER **T**ransform
FV	**F**inite **V**olume
FVM	**F**inite **V**olume **M**ethod
IDDES	**I**mproved **D**elayed **D**etached-**E**ddy **S**imulation

IBM	**I**mmersed **B**oundary **M**ethod
IIM	**I**mmersed **I**nterface **M**ethod
ILES	**I**mplicit **L**arge-**E**ddy **S**imulation
INCA	**I**ncompressible **N**AVIER-STOKES solver on **C**artesian **A**daptive grids
LES	**L**arge-**E**ddy **S**imulation
LE	**L**eading **E**dge
LESOCC2	**L**arge-**E**ddy Simulation **O**n **C**urvilinear **C**oordinates 2
LR	**L**arge **R**adius
LSWT	**L**ow **S**peed **W**ind **T**unnel
MAC	**M**ean-**A**erodynamic **C**hord
MPI	**M**essage **P**assing **I**nterface
MR	**M**edium **R**adius
ONERA	**O**ffice **N**ational d'tudes et de **R**echerches **A**rospatiales
PDE	**P**artial **D**ifferential **E**quation
PIV	**P**article **I**mage **V**elocimetry
RANS	**R**EYNOLDS-**A**veraged **N**AVIER-STOKES
Re	**R**EYNOLDS-number
rms	**r**oot of **m**ean **s**quare
RTO	**R**esearch-**T**echnology **O**rganization
S	**S**harp
SALD	**S**implified **A**daptive **L**ocal **D**econvolution
SGS	**S**ub-**G**rid-**S**cale
SR	**S**mall **R**adius
St	**S**TROUHAL-number
TBLE	**T**urbulent **B**oundary **L**ayer **E**quations
TKE	**T**urbulent **K**inetic **E**nergy
VFE-2	**V**ortex **F**low **E**xperiment 2
ZDES	**Z**onal **D**etached-**E**ddy **S**imulation

Symbols

Roman Symbols

a	natural number
$\boldsymbol{b}$	vector
b	real value
$\mathbf{C}$	momentum exchange force
C_D	drag coefficient
C_f	friction coefficient
C_L	lift force coefficient
C_p	pressure coefficient
c	retracted chord length
$\mathbf{D}$	friction force
d	diameter, projected cylinder width or distance
e	natural number
F	cell faces
$\mathbf{F}$	nonlinear flux function
f	frequency
h	distance
$\mathbf{I}$	unit matrix
l	length
$\mathbf{M}$	matrix
M	conserved mixing quantity
N	number of cells
$\boldsymbol{n}_\perp$	normal vector

$\boldsymbol{n}_{\parallel}$	tangential vector
$\boldsymbol{q}$	solution
P'	projection point of the interpolation point
P''	interpolation point
p	dimensionless pressure
q	solution
Re	$\textsc{Reynolds} - number$
St	$\textsc{Strouhal} - number$
t	time
tke	turbulent kinetic energy
$\tilde{U}$	velocity magnitude
$\mathbf{u}$	velocity vector
u	streamwise velocity component
v	wall-normal velocity component
V	cell volume
w	spanwise velocity component
$\mathbf{X}$	conserved exchanged quantity
x	first coordinate component (streamwise)
y	second coordinate component (wall-normal)
z	third coordinate component (spanwise)

Greek Symbols

α	angle (of attack)
β	(channel inclination) angle
γ	integer power
Γ	immersed interface surface
δ	walldistance measured in wallnormal direction to the immersed interface
Δt	time step size
Δh	grid spacing
Δx	spatial extent of a computational cell in the first spatial direction
Δy	spatial extent of a computational cell in the second spatial direction

Δz	spatial extent of a computational cell in the third spatial direction
ϵ	relative error
ζ	volume fraction
θ	angle position/azimuth in cylindrical coordinate system
κ	mixing fraction
λ	length scale
ν	kinematic viscosity
ρ	density
ϕ	pressure correction
τ	shear stress
$\mathbf{\Phi}$	conserved quantity
ω	vorticity
Ω	domain

Other Symbols

$\langle\cdot\rangle$	mean value (Reynolds filter)
$\cdot'$	fluctuation with respect to the mean value of a quantity
$\tilde{\cdot}$	magnitude of quantity
$\bar{\cdot}$	volume-averaged quantity
∞	free-stream value of a quantity
$\star$	intermediate value of a quantity

Subscripts

ave	average (time)
b	bulk property
ba	property at the base (of a cylinder)
crit	critical value of a quantity
D	drag
f	friction
i	cell index
j	cell index

k	cell index
L	lift
max	maximum value of a property
min	minimum value of a property
$\parallel$	parallel/colinear to the interface
$\perp$	perpendicular to the interface
p	pressure
r	root chord
rec	recirculation zone property
reatt	property at reattachment
ref	reference property
retr	retracted
rms	root-mean-square value of a property
sep	property at separation
stag	property at the stagnation point
tgt	property of the target cell
w	property at the wall
x	first coordinate component (streamwise)
y	second coordinate component(wall-normal)
z	third coordinate component (spanwise)
∞	free-stream property

Superscripts

n	time step number
$\star$	intermediate value of a quantity
$+$	normalized , frequently for scaling in wall units

Dedicated to the people supporting me.

Chapter 1

Introduction

Fluid flows being a key element of this thesis are involved in many processes in nature and technology, e.g. smoke rising from a chimney, blood transportation in the veins of creatures or the waves in the wake of a sailing boat.

In 1757 Leonhard Euler [38] formulated a first set of Partial Differential Equations (PDE) describing the motion of inviscid fluid flow. These equations were extended in 1823 by Claude Louis Marie Henri Navier [112] and, in 1845 by George Gabriel Stokes [155] independently of each other to viscid fluid flow. These so-called Navier-Stokes equations are based on Newton*'s Second Law* applied to fluid motion and presume a continuous, viscous, Newtonian fluid [6, 122]. They follow these three conservation principles of mechanics: conservation of mass, momentum and energy.

At first glance, it seems astonishing that even nowadays the Navier-Stokes equations have not been fully understood and the existence and regularity of unique solutions for problems in the three-dimensional space cannot be proven [39, 85]. However, the Navier-Stokes equations are widely used for fluid motion description and will be also used in this thesis. Other sets of equations such as the discrete (Lattice-) Boltzmann equation [18, 60] are not treated here.

The complexity of the flow, as to be understood in this thesis, is characterized by the fluid properties, the flow velocity, and involved geometrical objects. Even higher complexity can be expected when thermal or chemical processes as well as deforming geometries or compressibility effects are involved but these will be not investigated here.

In a turbulent flow state a flow is much more complex then in a laminar flow state. The state of turbulent flow is characterized by a significant and irregular variation of the velocity and the pressure field in space and time [132]. It was Ludwig Prandtl in 1914 who used the expression critical Reynolds number to distinguish between these two flow states [133]. However, the terminus Reynolds number itself was introduced in 1908 by Arnold Sommerfeld when presenting the Orr-Sommerfeld equation [151]. It is named after Osborne Reynolds in recognition of his achievements in this field of research. Above the critical Reynolds number, i.e. in the turbulent regime, the flow is characterized by a wide range of scales [132]: the flow geometry influence the large scales which control transport and mixing. On the other hand, the small scales are not affected by the flow geometry and show a universal character. The small-scale motion is determined by the dissipation rate at which they receive energy from the large scales and the viscosity [132]. Turbulent flows are prevalent in both, nature and industrial applications.

Yet, due to its high complexity, turbulence is not fully understood and a precise, generally accepted definition of turbulence does not exist so far [47].

For a better understanding of turbulent flow phenomena experiments and numerical simulation are used. In comparison to experiments numerical simulations offer a better repeatability, observationability, non-intrusiveness and are usually cheaper. The improvement of computational resources in the past decades further stimulated the interest in studying and understanding turbulent flows with numerical simulations [40]. The numerical simulation of complex turbulent incompressible flows based on the Navier-Stokes equations also gives the framework of this thesis. The focus is on the industrial applicability.

1.1 Motivation: Cartesian Grids and Immersed Interface Methods in Flow Simulations

In numerical flow simulations the Navier-Stokes equations are discretized in space on a computational grid and in time for computing a solution.

Requirements In the industrial context simulations require [52]:

- a straightforward set-up of computations,
- low computational resource needs, and
- sufficiently accurate results.

The setup of a computation consists of the geometry creation, the grid generation and the setting of flow-parameters and boundary conditions. Computational resources are determined by Central Processing Unit (CPU) time, so the time to solve the problem, and Resident Memory requirements, i.e. the amount of storage needed in the solving process. Sufficiently accurate results and computational resources are conflicting requirements. In the industrial context numerical simulations should use the least possible computational resources to produce sufficiently accurate results for the optimization processes in product development.

With respect to these requirements common numerical methods will be evaluated in the following part. The evaluation is summarized in Table 3.9. According to Peric [40] all numerical methods require

- *Consistency*: with decreasing grid spacing Δh and time step Δt, the discrete operator converges to the continuous operator of the PDE, where the difference decreases with $\mathcal{O}(\Delta h^a, \Delta t^e)$. a and e are the respective orders in space and in time.
- *Stability*: numerical errors should not amplify during the computation.
- *Convergence*: if both consistency and stability are provided, convergence can be achieved according to the Lax Equivalence Theorem [84] for "properly posed linear initial problems and a finite difference approximation". The numerical solution then converges to the analytical solution with increasing resolution in time and space. In this context the order of convergence is an expression for the decay of the truncation error. According to Peric [40] the Lax Equivalence Theorem is also conditionally valid for non-linear problems provided that all approximations of the discretization process are consistent.

Another important property for accurate turbulent flow simulation is the discrete conservation of mass, momentum and energy [57, 110, 128].

Grids The discretization can be either on a *body-fitted structured grid*, *body-fitted unstructured grid* or a *Cartesian grid*.

Body-fitted structured grids consist of families of grid lines with the property that members of a single family do not cross each other and cross each member of the other families only once. Structured grids can be mapped uniquely onto Cartesian grids and have a regular algebraic equation structure allowing the usage of efficient numerical solvers. On the other hand the generation of structured grids is time-consuming and difficult. Contradictory requirements, such as adequate local resolution and minimum number of grid points, can deteriorate the grid quality and therefore adversely affect accuracy and numerical convergence properties.

Body-fitted unstructured grids consist of elements or volume of arbitrary shape filling the fluid part of the computational domain. Generally tetrahedra and hexahedra are possible. The vertices of the elements must be associated with a connectivity list. Unstructured grids have no severe constraints on cell size and aspect ratio and can therefore be created automatically and easily refined in important regions [121]. Since the algebraic equation system of unstructured grids is not regular, efficient solvers are not applicable [40] and more resident memory is required then for structured grids [47]. Above all, unstructured grids are known to be not well suited for time-resolving turbulent-flow computations. Accurate turbulent flow computations require capturing of the fine flow features, i.e. the small scales. To achieve the same level of accuracy, computations on unstructured grids, especially those with tetrahedra elements, generally show that due to numerical damping more computational elements are required compared to computations on structured grids, see e.g. Refs. [46, 180]. Higher-order methods often suffer from insufficient robustness for industrial applications [115, 180].

Cartesian grids are the simplest form of a structured grid. They are similar to body-fitted structured grids except that line crossings are always perpendicular and the grid is not aligned with the geometry. As with structured body-fitted grids efficient numerical solvers can be used. At the same time, Cartesian grids can be generated automatically like unstructured grids. The full strength of Cartesian grids is exploited in block-structured grids where the computational domain can be subdivided into sub-level blocks with non-matching interfaces. Sub-level blocks in physically important regions can be refined as desired. Since Cartesian grids are generally not aligned with the geometry, the wall boundary condition is imposed by an Immersed Boundary Method [129]. Immersed Boundary Methods have

TABLE 1.1: Suitability of different numerical approaches for turbulent flow simulation in an industrial context (evaluation standard: -(worst) 0 +(best).

Discretization/Grid	Unstructured	Structured(curvilinear)	Cartesian
Finite Difference Method	-	0	+
Finite Element Method	+	-	-
Finite Volume Method	+	+	+

been successfully used for canonical configurations in the academic environment, e.g. Refs. [35, 78, 126], but it is still an open question whether they can model near-wall physics accurately enough for complex turbulent flows in an industrial context.

Discretization methods The discretization is realized by either

- Finite Difference Method (FDM),
- Finite Element Method (FEM),
- Finite Volume Method (FVM), or
- (spectral method[1])

The *Finite Difference Method* uses finite differences to approximate partial derivatives of the PDEs [164] and can be applied to any type of grid. At each grid point these finite differences are part of an algebraic equation, in which variable values at that point and a certain number of neighbor points appear as unknowns. The accuracy is determined by the finite difference function, e.g. TAYLOR series expansion or polynomial fitting. FDM is very simple and effective [40] on body-fitted structured grids and for simple geometries. For complex geometries with industrial relevance automatically generated unstructured grids would be more desirable but this would deteriorate the effectiveness. Modern implementations use Cartesian grids with their aforementioned special features. However, a general problem of FDM remains: mass and momentum are not conserved [40, 88] and this is crucial for accurate results in turbulent flow simulations [3, 20, 110, 176].

[1]For completeness *spectral methods* should be mentioned here, too. In spectral methods the solution is expanded in global, and generally orthogonal polynominals, e.g. FOURIER series [53]. For simple geometries and computational domains without corners spectral methods are highly efficient [15, 99]. However, they lose their exceptional properties for complex geometries. In this case they can be used in suitable sub-zones of the domain if desired [43]. All in all, spectral methods are less suitable for complex turbulent flows in an industrial context [43]

In the *Finite Element Method* an unstructured grid is built up by finite elements, e.g. usually tetrahedra and/or hexahedra. On these elements the PDEs are approximated by basis functions constructed with variable values at the corners [28]. After being multiplied with weight functions the equations are integrated over the entire domain. The result is a set of non-linear algebraic equations. The common combination of the FEM with unstructured grids brings the usual problem of less efficient solvers and rather high memory-consumption into play [47]. Even with higher-order approximations, e.g. piecewise-polynomial approximations, numerical damping and the lack of conservation are still a problem in turbulent flow simulations [88].

The *Finite Volume Method* uses the integral form of the PDE applied to finite control volumes filling the computational domain. The solution is to be understood as an control volume average. Surface and volume integrals are determined by quadrature formulae [40]. In contrast to the other methods, the FVM is generally conservative by construction making this method highly suitable for turbulent flow simulations. Body-fitted grids show their typical problems: unstructured grids do not allow for efficient solvers and structured grids are difficult to be generated. A good alternative is the usage of Cartesian grids along with the aforementioned Immersed Boundary Method to impose the wall boundary condition. Cartesian grids imply fewer computational operations per grid point than body-fitted grids.

Concluding remarks on employed discretization and grid It can be concluded, that for this thesis, a finite-volume discretization on a Cartesian grid is the most adequate approach. Grids can be both automatically generated and adapted to the flow problems, efficient solving methods can be applied and discrete conservation is generally ensured. This motivates the proposal of an Immersed Boundary Method (IBM), or more generally an Immersed Interface Method (IIM), to impose the wall boundary condition in an effective and efficient way. It must be ensured that the proposed method is also valid for complex turbulent flows of industrial relevance.

1.2 State of the Art: Immersed Interface Methods

On Cartesian grids bounding surfaces of the flow or immersed obstacles need to be accounted for by mapping the boundaries onto the grid. The formulation of accurate interface conditions at boundaries that are not aligned with the grid is a major challenge. Approaches, which have been proposed in literature, can be classified into continuous and discrete forcing approaches [103].

In the continuous forcing approach [129], a distributed forcing function is inserted into the momentum equations to mimic the interaction at the interface. The forcing function contains model parameters that have to be adapted to the flow configuration. Various extensions and adaptations have been proposed [55, 77, 83, 130, 137]. Disadvantages of this approach are that sharp interfaces are smeared over an area corresponding to the local mesh width [129], and that discrete conservation is not guaranteed. An application to solid boundaries can lead to stability and accuracy issues due to the stiffness of the forcing function [83, 154].

Mohd-Yosuf [108] and Verzicco et al. [177] developed a predictor-corrector formulation for enforcing a wall boundary condition with a discrete forcing function in the momentum equations. Whereas the accurate representation of the boundary has been demonstrated, the approach lacks discrete conservativity. Ghost-cell approaches [168] and reconstruction methods [74, 77, 95, 126] both use interpolation to impose the boundary conditions at the interface. While the former extrapolates velocity and pressure field to ghost cells based on nearby fluid points to enforce the boundary condition, the latter reconstructs the velocity field near the immersed boundary. Both methods are attractive because of their simplicity. However, in general these methods do not conserve discrete momentum and mass in the vicinity of the interface [74, 77].

Another discrete forcing approach is the cut-cell method introduced first for inviscid flows by Clarke [26], later extended to viscous flows [170–172, 182]. Cells cut by the immersed interface are truncated so that they conform to the shape of the boundary surface. The cut-cell method is based on a finite-volume discretization and generally maintains discrete conservation. A sharp representation of the immersed interface can be achieved. A common problem of cut-cell methods is the creation of very small fluid cells that lead to numerical instability if left

untreated [78]. However, this approach seems the most appropriate for dealing with turbulent flows when an accurate representation of the flow in the vicinity of the immersed interface is required. Collela et al.[27, 73] applied the cut-cell method to free surface flows in three dimensions on a collocated grid. Ye et al. [182] proposed a finite-volume collocated-grid formulation for incompressible fluid-flows, where the fluid part of cut cells, whose center is located within the solid, is merged with adjacent fluid cells. To ensure second-order accuracy, the flux calculation requires an interpolation of the cell variables and their gradients at the cell faces near the boundary. The method has been applied to simulate various two-dimensional flows with stationary and moving boundaries [105, 106]. Chung [23] modified the cell merging approach of Ye et al. [182] to improve the shape resolution of the immersed interface. However, second-order grid convergence has not been achieved.

For the incompressible Navier-Stokes equations pressure-velocity coupling is an essential concern [97]. Unlike collocated grids, approaches based on staggered grids allow for a consistent finite-volume discretization of the divergence-free constraint and have favorable stability properties [40]. Only few cut-cell methods for staggered grids have been reported in literature: Tau [159] and Tucker [169] addressed two-dimensional problems with first-order accuracy at the boundaries. Kirckpatrick et al. [78] presented a three-dimensional method on staggered grids, where advective fluxes and diffusive fluxes of the cut cells are modified. The small-cell problem is addressed by linking small cells and adjacent fully fluid cells to form a master-slave pair. Boundary conditions for the pressure at the immersed boundary are not imposed directly but by the projection method of Bell et al. [8], requiring several inner and outer iteration loops. Dröge and Verstappen [35, 36] propose a method motivated by preserving the symmetry of the convective and diffusive operators. The authors emphasize that boundary conditions at the immersed interfaces cannot be defined without adversely effecting either the symmetry of the operators or the global accuracy. Both the method of Kirckpatrick et al. and the method of Dröge and Verstappen achieve second-order spatial accuracy and show good results for flows with simple solid boundaries.

However, for moving boundaries, fluid-structure interaction problems and turbulent flows of industrial relevance not only conservativity [3, 20, 110, 176] but also a simpler representation of the geometry are desirable. A simple representation

of geometries is likewise useful for complex three-dimensional bodies of arbitrary shape.

1.3 Accomplishments of this Work

The accomplishments of this work are[2]:

1. **Immersed Interface Method Development** The objective is to develop a Cartesian cut cell method for the incompressible NAVIER-STOKES equations which is applicable to any finite-volume discretization on three-dimensional staggered Cartesian grids. Cut cell methods **retain the discrete mass and momentum conservation** of finite-volume discretizations by construction. The method should **be second-order accurate** and **offer a simple geometry representation** allowing for a straightforward extension to moving boundaries. The method should **efficiently work** with **stretched or locally-refined grids** to meet industrial requirements [40]. All desired features should be validated. The question whether this method can **accurately model near-wall physics** of turbulent flows is addressed.

2. **Application to Complex Turbulent Flows with Industrial Relevance** The novel Conservative Immersed Interface Method (CIIM) in combination with a wall-modeling approach [19] is applied to two complex turbulent flow simulations on adaptively refined grids. The test cases should prove that the Immersed Interface Method can accurately predict complex turbulent flows bounded by geometries of arbitrary shape and industrial relevance.

1.4 Outline

This thesis consists of six chapters including this introductional Chapter 1. For the fast reader each chapter is summarized at its end. In Chapter 2 the governing equations, i.e. the NAVIER-STOKES equations, are introduced and discretized in time and space. Notions will be given on boundary conditions and conservation. Different ways of turbulence modeling will be considered. The novel Conservative

[2]Requirements are in bold letters

Immersed Interface Method (CIIM) is developed in detail. In Chapter 3 a broad spectrum of test cases is used to validate the CIIM with respect to the desired characteristics. After this validation CIIM is applied in combination with a wall-modeling approach and an adaptive grid refinement approach to two test cases with industrial relevance: (1) a turbulent flow over a three-element highlift airfoil in Chapter 4 and (2) a turbulent flow over the VFE-2 delta wing in Chapter 5. In Chapter 6 final conclusions are drawn.

Chapter 2

Numerical Method

In *numerical simulations* the part of reality relevant to a specified problem is expressed by a *mathematical model* which is further translated into a *numerical model* for computing dedicated solutions. Already implied by the word model, this is an abstraction of the reality and to be understood as the best possible compromise between completeness and complexity. The complexity determines the feasibility of a numerical simulation and the completeness determines whether the reality is represented sufficiently.

In the *mathematical model*, one necessary restriction of complexity is that not the entire reality but a limited domain of it is represented. With respect to the boundary of the represented domain (realistic) *boundary conditions* are necessary. Similarly proper initial conditions, must be defined for a well-posed problem.

In the *numerical model*, the equations of the *mathematical model*, here the Navier-Stokes equations, are included in a discretized fashion using *numerical methods*. For *numerical simulations* of fluid flows the *governing equations* are discretized in space and time. Further *modeling* is included to cope with *turbulence* and, in this thesis, to impose the wall boundary condition with an *Immersed Interface Method*.

2.1 Mathematical Model

2.1.1 Governing Equations

A generic conservation equation in differential form on the domain Ω is considered

$$\partial_t \mathbf{\Phi} + \nabla \cdot \mathbf{F} = 0, \tag{2.1}$$

where $\mathbf{\Phi}$ represents a conserved quantity and $\mathbf{F}$ is a flux function. The Navier-Stokes equations for incompressible fluid flows are recovered if $\mathbf{\Phi}$ equals the velocity $\mathbf{u} = [u, v, w]$ and $\mathbf{F}$ is the nonlinear flux function

$$\mathbf{F} = \mathbf{uu} + \mathbf{I}p - \frac{1}{Re}\nabla\mathbf{u}, \tag{2.2}$$

where p is the pressure and $\mathbf{I}$ is the unity tensor. The Reynolds number Re is defined as

$$Re = \frac{u_{ref} l_{ref}}{\nu}, \tag{2.3}$$

where ν represents the kinematic viscosity, l_{ref} is a reference length scale and u_{ref} a reference velocity. The integral form of the transport equation Eq. 2.1 is

$$\partial_t \int_\Omega \mathbf{u}\, d\Omega + \int_S \mathbf{uu}\, \mathbf{dS} = -\int_S \mathbf{I}p\, \mathbf{dS} + \frac{1}{Re}\int_S \nabla\mathbf{u}\, \mathbf{dS}, \tag{2.4}$$

where S denotes the faces of Ω and $\mathbf{dS}$ the product of S and its normal vector. Mass conservation of Ω is ensured by

$$\nabla \cdot \mathbf{u} = 0, \tag{2.5}$$

or in the integral form by

$$\int_S \mathbf{u}\, \mathbf{dS} = 0. \tag{2.6}$$

In incompressible flows the energy equation is not an independent transport equation but can be derived from the momentum transport equation above.

2.1.2 Boundary Conditions

For obtaining a unique solution to the NAVIER-STOKES equations additional information is required at the boundaries of Ω. With respect to the solution either a specified value (DIRICHLET boundary conditions), the gradient orthogonal to the boundary of the domain (NEUMANN boundary condition) or a linear combination of them (ROBIN boundary condition) must be given. The standard inlet, outlet, periodic and wall boundary conditions are explained in detail in [40] and [178].

Since the incompressible NAVIER-STOKES equations are incompletely parabolic coupled with an elliptic set of equations, boundary conditions for the velocity must be prescribed at all boundaries. Because of the coupling of pressure and velocity a condition for the pressure is possible at open boundaries (inlet or outlet) [40].

While wall boundary conditions on a body-fitted grid are straightforward, for Cartesian grids an Immersed Interface condition must be employed. With the presence of diffusion the wall tangential velocities of the flow are zero, which implies a no-slip boundary condition, and the wall normal velocity of the flow is zero, signifying the non-permeability of the wall. According to the homogeneous NEUMANN condition [40], the pressure gradient normal to the wall vanishes.

2.2 Numerical Model

2.2.1 Turbulence Modeling

The NAVIER-STOKES equations can be used in numerical simulation to fully describe laminar and turbulent flows. However, existing computational resource constraints still restrict the spectrum of the time and length scales that can be resolved [40].

Direct Numerical Simulation To solve the NAVIER-STOKES equations for all scales, in so-called Direct Numerical Simulations (DNS) is restricted to moderate REYNOLDS numbers. Yet, DNS is an important approach to understand fundamental physical processes in scientific problems.

Reynolds-Averaged Navier-Stokes equations Simulation In approaches based on the Reynolds-Averaged Navier-Stokes equations not the instantaneous velocity field but the mean velocity field is calculated with the help of statistical turbulence models. The high level of abstraction makes Reynolds-Averaged Navier-Stokes Simulation (RANS) suitable for industrial application. However, both RANS and also its extension to Unsteady RANS (URANS) often fail to predict massively separated and reattached flows, as reported by many authors e.g. Refs. [114, 144, 152].

Large-Eddy Simulation Large-Eddy Simulation (LES) resolves the large energy-containing structures but does not resolve down to the smallest scales, i.e. the Kolmogorov scales [79, 80]. Small scale-motions are neglected, however, LES uses Sub-Grid-Scale (SGS) Models to account for the nonlinear interaction between the resolved and non-resolved turbulent scales. Yet, in attached turbulent boundary layer simulations, SGS models like the eddy-viscosity based and commonly-used Smagorinsky model [148] do not correctly reproduce the sub-grid stresses of the near-wall regions [72]. Alternatively, to fully resolve the near-wall physics leads to prohibitively fine resolutions being[3] the biggest counter-argument against the industrial application of LES [5, 72]. Since the outer boundary layer resolution is Reynolds number independent significant efforts have been made to find appropriate ways to cope with the Reynolds-number dependent near-wall physics. In this context, hybrid RANS-LES [152] and LES in combination with wall-models or wall-functions [131] have been developed.

Hybrid RANS/LES or Detached-Eddy Simulation Hybrid RANS/LES approaches like Detached-Eddy Simulation (DES) have been developed with the objective to efficiently and accurately predict massively separated flows while exploiting the efficiency of RANS for the attached shear layer and the accuracy of LES for the separated shear layer

Detached Eddy Simulation is originally understood as "a three-dimensional unsteady numerical solution using a single turbulence model, which functions as a SubGrid-Scale model in regions where the grid density is fine enough for a Large-Eddy Simulation, and as a Reynolds-averaged model in regions where it is not [166]. Traditional DES uses the Spalart-Allmaras model on the RANS

[3] computational cost for resolving the viscous sublayer scale with $Re^{2.4}$

side and the SMAGORINSKY model on the LES side, however, several derivatives with different turbulence models [156] and RANS/LES interface treatments have been proposed [127]. The possibility to use and adopt different turbulence models in different flow regions is the greatest advantage of DES but also the main source for controversy and problems.

The key practical issues using DES are grid-induced separation, modeled stress depletion and logarithmic-layer mismatch [152]. To overcome grid-induced separation and modeled stress depletion in Zonal DES (ZDES) the user explicitly marks regions for RANS and LES [31]. Good results have been achieved by various research groups [14, 17, 145, 147], however, in complex flows with numerous possible RANS or LES regions the decision for explicit marking is questionable. With the same motivation but with different implementation Delayed Detached Eddy Simulation (DDES) [153] employs a DES limiter also depending on the eddy viscosity instead of the grid spacing only to switch between the turbulence modeling modes. Improved Delayed Detached Eddy Simulation (IDDES) [143] even tries to overcome logarithmic-layer mismatch with additional REYNOLDS-number based empirical functions. Although these approaches achieved good results for simple configurations a convincing (comprehensive) calibration for DES of complex flows is still out of reach [152]. Practically in DES the RANS and the LES models are adjusted based on results rather than explicit tests like the CLARK-test [25] or a priori studies.

To the author an even more severe problem for turbulent flow prediction is the reported uncertainty of solutions [50, 152], linked to the chosen initial conditions and the selection of the turbulence model.

Implicit Large-Eddy Simulations In this thesis an Implicit Large-Eddy Simulation (ILES) based on the Adaptive Local Deconvolution Method (ALDM) is applied. The theoretical background of implicit LES with ALDM [1, 64] follows from the formal equivalence between cell-averaging and reconstruction in finite-volume discretizations, and top-hat filtering and deconvolution in explicit SGS-modeling. With ALDM, a local reconstruction of the unfiltered solution is obtained from a solution-adaptive combination of approximation polynomials. Deconvolution and interpolation are done simultaneously using LAGRANGIAN polynomials as proposed by HARTEN [58]. Deconvolution is regularized by limiting the degree of

local approximation polynomials and by permitting all polynomials up to a certain degree to contribute to the approximately deconvolved solution. Adaptivity of the deconvolution operator is achieved by dynamically weighing the respective contributions. A suitable consistent numerical flux function operates on the approximately deconvolved solution. The solution-adaptive stencil-selection scheme and the numerical flux function contain free parameters which can be used to adjust the spatial truncation error of the discretization.

Free parameters of ALDM are selected such that the truncation error of the discretization functions as physically motivated SGS model. Given that the primary purpose of a SGS model is to provide the correct spectral distribution of the dissipation of resolved scales through interactions with modeled SGS stresses, free discretization parameters were calibrated by constraining the numerical dissipation to the physical SGS dissipation obtained from the analysis of nonlinear interactions in homogeneous isotropic turbulence [64]. The general validity of the determined model has been demonstrated for various canonical flow configurations [62–65].

In LES the chosen grid size essentially defines the smallest represented physical scale. At finite grid size, the numerical truncation errors interfere with the SGS model and modeling errors. In particular for implicit LES, the numerical discretization and the turbulence model are indistinguishable. For non-turbulent flows ALDM corresponds to a standard central second-order finite-volume scheme, whereas for turbulent flows it provides a SGS model implicitly. With respect to ALDM Cartesian grids offer the favorable feature to easily calibrate the truncation error.

2.2.2 Discretization in Space and Time

A finite-volume discretization of Eq. (2.4) is obtained by

$$\frac{1}{V_{i,j,k}\Delta t}\int_{t_n}^{t_{n+1}} dt \int_{V_{i,j,k}\cap\Omega} dx\ dy\ dz \left(\frac{\partial \mathbf{u}}{\partial t} + \nabla\cdot\mathbf{F}\right) = 0, \tag{2.7}$$

where $V_{i,j,k} \cap \Omega$ is a computational cell (i,j,k) of a Cartesian Grid with a volume $V_{i,j,k}$. Time integration is performed from step t_n to t_{n+1} with the time step size

$\Delta t = t_{n+1} - t_n$. Volume-averaged quantities $\overline{\mathbf{u}}$ are defined as

$$\overline{\mathbf{u}}_{i,j,k} = \frac{1}{V_{i,j,k}} \int_{V_{i,j,k} \cap \Omega} \mathbf{u}_{i,j,k} \; dx \; dy \; dz. \tag{2.8}$$

Discretizing Eq. (2.7) in time with an EULER forward scheme, which corresponds to a substep of the RUNGE-KUTTA scheme [142] used later, results in

$$\frac{\overline{\mathbf{u}}^{n+1}_{i,j,k} - \overline{\mathbf{u}}^{n}_{i,j,k}}{\Delta t} = \frac{1}{V_{i,j,k}} \int_{V_{i,j,k} \cap \Omega} \nabla \cdot \mathbf{F}(\overline{\mathbf{u}}^n, \overline{p}^n)_{i,j,k} \; dx \; dy \; dz. \tag{2.9}$$

The divergence-free condition Eq. (2.6) is enforced by a fractional-step method with the intermediate velocity

$$\overline{\mathbf{u}}^{\star}_{i,j,k} = \overline{\mathbf{u}}^{n}_{i,j,k} + \frac{\Delta t}{V_{i,j,k}} \int_{V_{i,j,k} \cap \Omega} \nabla \cdot \mathbf{F}(\overline{\mathbf{u}}^n, \overline{p}^n)_{i,j,k} \; dx \; dy \; dz, \tag{2.10}$$

where $\mathbf{F}(\overline{\mathbf{u}}^n_{i,j,k}, \overline{p}^n)$ includes a predictor for the pressure gradient using the pressure at time step n. For pressure projection a POISSON equation

$$\nabla^2 \overline{\phi}_{i,j,k} = -\nabla \cdot \; \overline{\mathbf{u}}^{\star}_{i,j,k}, \tag{2.11}$$

is solved, leading to a divergence-free velocity field

$$\overline{\mathbf{u}}^{n+1}_{i,j,k} = \overline{\mathbf{u}}^{n}_{i,j,k} - \nabla \overline{\phi}_{i,j,k}. \tag{2.12}$$

Finally the pressure is updated by

$$\overline{p}^{n+1}_{i,j,k} = \overline{p}^{n} + \frac{\overline{\phi}_{i,j,k}}{\Delta t}. \tag{2.13}$$

By the GAUSS theorem, the right-hand side of Eq. (2.10) becomes

$$\overline{\mathbf{u}}^{\star}_{i,j,k} = \overline{\mathbf{u}}^{n}_{i,j,k} + \frac{\Delta t}{V_{i,j,k}} \int_{\partial(V_{i,j,k} \cap \Omega)} \mathbf{F}(\overline{\mathbf{u}}^n, \overline{p}^n)_{i,j,k} \cdot \mathbf{n}_{\perp} dS, \tag{2.14}$$

where $\partial(V_{i,j,k} \cap \Omega)$ is the surface of $V_{i,j,k} \cap \Omega$, i.e. the six finite-volume cell faces intersecting with the Cartesian grid at $(x_i \pm \Delta x/2, y_i, z_i)$, $(x_i, y_i \pm \Delta y/2, z_i)$, and $(x_i, y_i, z_i \pm \Delta z/2)$. The normal vector on the cell faces is $\mathbf{n}_{\perp}$. Eq. (2.14) finally

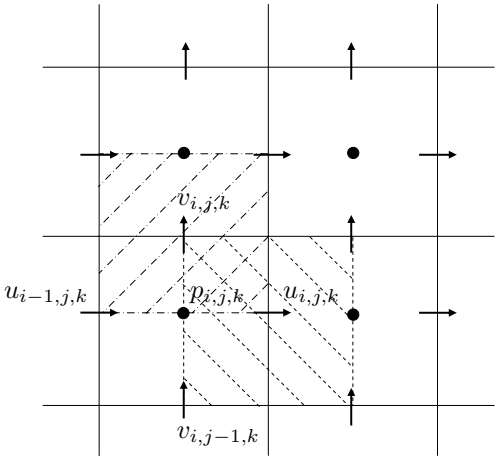

FIGURE 2.1: u control volume (——), v control volume ($\cdot - \cdot$) and p control volume of a cell on a staggered grid in 2D; arrows indicate locations of velocity components, circles locations of pressure.

becomes

$$\begin{aligned}\overline{\mathbf{u}}^{\star}_{i,j,k} = \overline{\mathbf{u}}^{n}_{i,j,k} &\\ &+ \frac{\triangle t}{\triangle x}\left[\overline{\mathbf{F}}_{i+1/2,j,k} - \overline{\mathbf{F}}_{i-1/2,j,k}\right]\\ &+ \frac{\triangle t}{\triangle y}\left[\overline{\mathbf{F}}_{i,j+1/2,k} - \overline{\mathbf{F}}_{i,j-1/2,k}\right]\\ &+ \frac{\triangle t}{\triangle z}\left[\overline{\mathbf{F}}_{i,j,k+1/2} - \overline{\mathbf{F}}_{i,j,k-1/2}\right], \end{aligned} \tag{2.15}$$

where $\overline{\mathbf{F}}_{i\pm1/2,j,k}$, $\overline{\mathbf{F}}_{i,j\pm1/2,k}$, $\overline{\mathbf{F}}_{i,j,k\pm1/2}$ are the face-averaged fluxes at the cell faces. Eq. (2.15) corresponds to a standard finite-volume discretization on a three-dimensional Cartesian grid. For the following section it is important to keep in mind that the momentum equations are discretized on a staggered grid (see Fig. 2.1). In this work, fluxes in Eq. (2.15) are computed with ALDM.

2.3 Conservative Immersed Interface Method (CIIM)

The flux balance in Eq. (2.15) must be modified appropriately for cells that are cut by an interface, see Fig. 2.2. For cut cells the wetted surface is defined by the unity of the fraction of the six cell faces wetted by the fluid and the subset of the interface contained in the cell $V_{i,j,k} \cap \Omega$. The latter is approximated by a planar element $\Gamma_{i,j,k}$. At the interface $\Gamma_{i,j,k}$ the no-slip conditions for the normal velocity

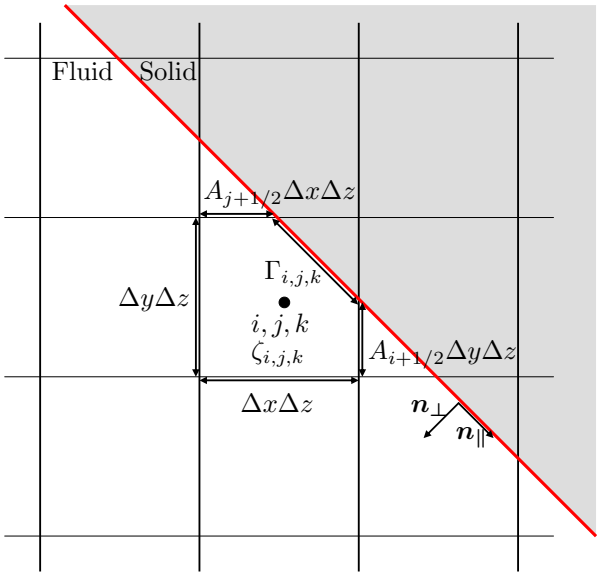

FIGURE 2.2: Fluid volume fraction $\zeta_{i,j,k}$, intersection of $\partial(V_{i,j,k} \cap \Omega)$ and interface with cell $\Gamma_{i,j,k}$, for the cut cell i,j,k.

$\overline{\mathbf{u}}_\perp = (\overline{\mathbf{u}} \cdot \mathbf{n}_\perp)\mathbf{n}_\perp = 0$ and the tangential velocity components $\overline{\mathbf{u}}_\parallel = \overline{\mathbf{u}} - \overline{\mathbf{u}}_\perp = \mathbf{0}$ and the NEUMANN condition for pressure $\nabla\overline{p} \cdot \mathbf{n}_\perp = \mathbf{0}$ must be satisfied.

Volume balance For the cut cells the finite-volume formulation is maintained by taking into account face apertures, volume fraction and the interface segment $\Gamma_{i,j,k}$. The fluid volume fraction of a cut cell is denoted as $\zeta_{i,j,k}$ with $0 \leq \zeta_{i,j,k} \leq 1$. The wetted segment of the cell faces can be written as $A_{i\pm1/2,j,k}\triangle y\triangle z$, $A_{i,j\pm1/2,k}\triangle x\triangle z$, and $A_{i,j,k\pm1/2}\triangle x\triangle y$, where $0 \leq A_{l,m,n} \leq 1$ are the face apertures. Accordingly, the fluid volume of a cell is $V_{i,j,k} = \zeta_{i,j,k}\triangle x\triangle y\triangle z$. Eq. (2.15) can be rewritten as

$$\begin{aligned}\overline{\mathbf{u}}^\star_{i,j,k} = \overline{\mathbf{u}}^n_{i,j,k} &\\ &+ \frac{\triangle t}{\zeta_{i,j,k}\triangle x}\left[A_{i+1/2,j,k}\overline{\mathbf{F}}_{i+1/2,j,k} - A_{i-1/2,j,k}\overline{\mathbf{F}}_{i-1/2,j,k}\right]\\ &+ \frac{\triangle t}{\zeta_{i,j,k}\triangle y}\left[A_{i,j+1/2,k}\overline{\mathbf{F}}_{i,j+1/2,k} - A_{i,j-1/2,k}\overline{\mathbf{F}}_{i,j-1/2,k}\right]\\ &+ \frac{\triangle t}{\zeta_{i,j,k}\triangle z}\left[A_{i,j,k+1/2}\overline{\mathbf{F}}_{i,j,k+1/2} - A_{i,j,k-1/2}\overline{\mathbf{F}}_{i,j,k-1/2}\right]\\ &+ \frac{\triangle t}{\zeta_{i,j,k}\triangle x\triangle y\triangle z}[\mathbf{C} + \mathbf{D}],\end{aligned} \tag{2.16}$$

where the friction term $\mathbf{D}$ represents the friction force at $\Gamma_{i,j,k}$ and is required to enforce the no-slip condition with respect to the interface-tangential velocity

components at $\Gamma_{i,j,k}$. $\mathbf{C}$ is a momentum exchange term which imposes the no-slip condition with respect to the normal velocity components at the interface. All terms on the right-hand-side of Eq. (2.16) are evaluated at time t^n. A more detailed description of these terms will be given below.

The face apertures, volume fractions and the interface segment (see Fig. 2.2) can be determined by any suitable approach. When the interface is represented by a zero level-set contour many efficient approaches for calculating these quantities are possible [119, 120]. The use of a level-set field description allows for the treatment of arbitrary geometries and for a straightforward extension to moving interfaces. Empty cells, i.e., cells with zero fluid volume fraction and zero face apertures, are initialized with $\overline{\mathbf{u}} = \mathbf{0}$ and are left unmodified during time advancement in fluid-solid interaction problems.

Friction term The friction force on $\Gamma_{i,j,k}$ is accounted for by adding

$$\mathbf{D} = -\int_{\Gamma_{i,j,k}} \boldsymbol{\tau} dS, \tag{2.17}$$

to the flux balance of Eq. (2.16). Similarly to [78] the velocity gradients in tangential direction are neglected because they are zero for rigid immersed boundaries. Furthermore the continuity condition in Eq. (2.6) must be satisfied, therefore the wall shear stress $\boldsymbol{\tau}$ can be expressed in a local frame of reference (see Fig. 2.3) as

$$\boldsymbol{\tau} = \nu \left(\nabla \overline{\mathbf{u}}\right) \cdot \mathbf{n}_{\perp}, \tag{2.18}$$

using the kinematic viscosity ν Eq. (2.17) becomes

$$\mathbf{D} = -\int_{\Gamma_{i,j,k}} \nu \left(\nabla \overline{\mathbf{u}}\right) \cdot \mathbf{n}_{\perp} dS. \tag{2.19}$$

For a linear approximation of the wall-normal velocity gradient the difference of the interface velocity $\overline{\mathbf{u}}_{\boldsymbol{\Gamma}}(P')$ and the tangential velocity $\overline{\mathbf{u}}_{\parallel}(P'')$ in point P'' is used, see Fig. 2.3. P'' is located in the interface normal direction at the distance Δh from the foot point P'. P' is the normal projection of the cell center of cell (i,j,k) on $\Gamma_{i,j,k}$. The velocity in P'' is calculated by trilinear LAGRANGIAN interpolation of the velocities at the eight neighboring velocity-cell centers. The final form of $\mathbf{D}$ is

$$\mathbf{D} = -\frac{\nu \Gamma_{i,j,k}}{\Delta h} \left(\overline{\mathbf{u}}_{\parallel} - \overline{\mathbf{u}}_{\Gamma}\right). \tag{2.20}$$

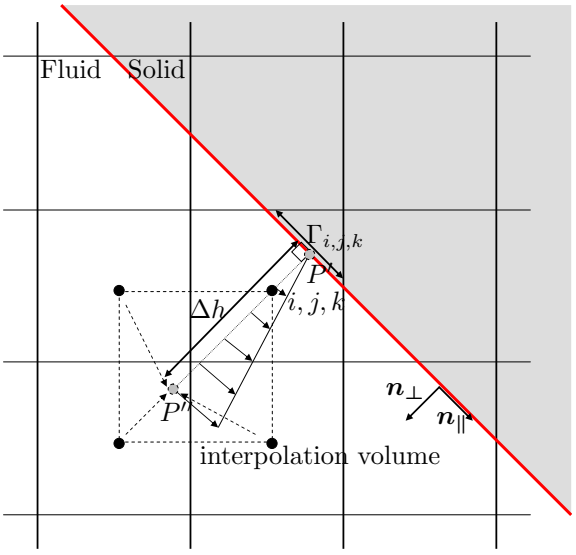

FIGURE 2.3: Linear approximation of the velocity gradient of a velocity cell.

The velocity $\overline{\mathbf{u}}_{\Gamma}$ at the boundary is known and vanishes for non-moving boundaries. The distance Δh needs to be related to the cell volume so that

$$\Delta h = 0.5 \sqrt{(\triangle x \cdot n_{\perp,x})^2 + (\triangle y \cdot n_{\perp,y})^2 + (\triangle z \cdot n_{\perp,z})^2}. \tag{2.21}$$

$\triangle x$, $\triangle y$ and $\triangle z$ are the dimensions of the control volume i, j, k and $n_{\perp,x}$, $n_{\perp,y}$, $n_{\perp,z}$ are components of the normal vector on $\Gamma_{i,j,k}$. We note that the friction term in Eq. (2.16) can be extended in a straightforward way to include a wall model for turbulence [19]. However, no wall model will be used in the validation test cases to prevent any influence while investigating the Immersed Interface Method.

Momentum-exchange term C For impermeable interfaces the interface normal velocity of the fluid equals that of the interface. In the following it is assumed that the interface is impermeable and does not move so that the interface normal velocity $\overline{\mathbf{u}}_{\perp} = (\overline{\mathbf{u}} \cdot \mathbf{n}_{\perp})\mathbf{n}_{\perp}$ vanishes. This is achieved with a pressure-velocity coupling term, which is required because some small cut cells do not contribute to the discrete POISSON equation on a staggered grid. More details will be given in the following paragraphs of this subchapter. For small cells that do not contribute to the discrete POISSON equation we impose the zero-normal-velocity condition by

$$\mathbf{C} = -\overline{\mathbf{u}}_{\perp,i,j,k} \frac{V_{i,j,k}}{\triangle t}. \tag{2.22}$$

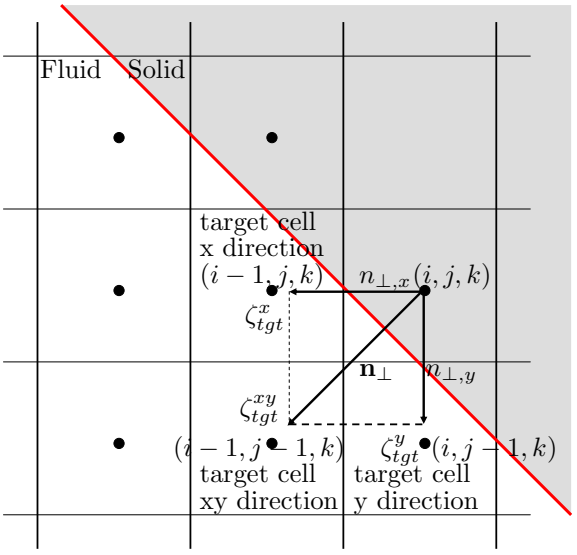

FIGURE 2.4: Mixing procedure for the small fluid cell (i,j,k).

C is added to the flux balance in Eq. (2.16). A generalization to moving boundaries is straightforward.

Small cell treatment Cut cell methods, such as the one presented in this thesis, can generate cells with a very small fluid volume fraction. A special treatment of such cells is necessary for numerical stability if excessively small time steps are to be avoided. For such purposes cell merging [182], cell linking [78], and mixed approaches [59] are reported in literature. Cell merging requires calculating additional fluxes with adjacent cells. Also, the formulation of merging algorithms in three dimensions tends to be cumbersome [78]. Cell linking [78] can avoid such problems. However, due to various conditional operations, this approach appears less suitable for the treatment of moving boundaries.

In the present method, the fluid of the small cells is mixed with that of the neighboring cells. The approach of Hu et al. [69] is adapted for three-dimensional staggered grids. Target cells for mixing are determined through an evaluation of the normal vector $\mathbf{n}_\perp = [n_{\perp,x}, n_{\perp,y}, n_{\perp,z}]$. Different from the original approach [69] all next neighbor cells are included in the mixing procedure. Suppose (i,j,k) is a cut cell, there are three target cells in two dimensions, as shown in Fig. 2.4, and seven target cells in three dimensions. The conservative exchange between the small cell (i,j,k) and the target cell in, e.g., x-direction, is calculated by

$$X^x = \frac{\kappa^x_{i,j,k}}{\kappa^x_{i,j,k} V_{i,j,k} + V_{tgt}} [V_{i,j,k}(Vq^\star)_{tgt} - V_{tgt}(Vq^\star)_{i,j,k}], \tag{2.23}$$

where tgt is the index of the target cell and $q^\star$ is the mixed conservative quantity. Terms for target cells in the other directions are formulated accordingly. $q^\star$ can be the flux divergence $\nabla \cdot \mathbf{F}$, the velocity $\overline{\mathbf{u}}$ or a scalar concentration. It has been found that mixing $\nabla \cdot \mathbf{F}$ results in a more accurate pressure approximation, see also the paragraph **Implementation**. $\kappa^x_{i,j,k}$ is the fraction of mixing with the target cell in x direction. The mixing fractions $\kappa_{i,j,k}$ are defined as

$$\begin{aligned}
\kappa^x_{i,j,k} &= n^2_{\perp,x} {\zeta^x_{tgt}}^\gamma, & \kappa^y_{i,j,k} &= n^2_{\perp,y} {\zeta^y_{tgt}}^\gamma, \\
\kappa^z_{i,j,k} &= n^2_{\perp,z} {\zeta^z_{tgt}}^\gamma, & \kappa^{xy}_{i,j,k} &= |n_{\perp,x} n_{\perp,y}| \zeta^{xy\gamma}_{tgt}, \\
\kappa^{xz}_{i,j,k} &= |n_{\perp,x} n_{\perp,z}| \zeta^{xz\gamma}_{tgt}, & \kappa^{yz}_{i,j,k} &= |n_{\perp,y} n_{\perp,z}| \zeta^{yz\gamma}_{tgt}, \\
\kappa^{xyz}_{i,j,k} &= |n_{\perp,x} n_{\perp,y} n_{\perp,z}|^{2/3} \zeta^{xyz\gamma}_{tgt}.
\end{aligned} \tag{2.24}$$

These mixing fractions are normalized subsequently in order to satisfy

$$\kappa^x_{i,j,k} + \kappa^y_{i,j,k} + ... + \kappa^{xyz}_{i,j,k} = 1. \tag{2.25}$$

The contributions of cells with large volume fraction are amplified by the integer power $\gamma \geq 1$. This leads to a stronger contribution of cells with a bigger volume fraction thus enhancing numerical stability. Throughout this thesis $\gamma = 5$ is used. Note that conservation is ensured since each conservative quantity $M_{i,j,k}$ that a small cell obtains from a target cell corresponds to a loss M_{tgt} in the target cell.

$$M^x_{i,j,k} = X^x = -M^x_{tgt}, \tag{2.26}$$

Once the mixing exchanges are determined for all small cells the solution q is obtained by

$$q_{i,j,k} = q^\star_{i,j,k} + \frac{1}{V_{i,j,k}} \left(\sum M^x + \sum M^y + ... + \sum M^{xyz} \right), \tag{2.27}$$

where $q^\star$ is the solution before mixing (see also the paragraph on **Implementation**. Since mixing is carried out before the final pressure projection, the solution after each time step is divergence free.

Homogeneous Neumann condition for pressure projection To satisfy the incompressible continuity equation (2.6), a Poisson equation is solved for the pressure correction $\overline{\phi}$

$$\nabla^2 \overline{\phi}_{i,j,k} = -\nabla \cdot \overline{\mathbf{u}}^\star_{i,j,k}. \tag{2.28}$$

For consistency it is necessary to use the same discrete gradient and divergence operators in the momentum equation Eq. (2.16) and for Eq. (2.28). Using a staggered grid formulation, the velocities at the cell faces of the pressure cell are known, so that the discretized POISSON equation can be written as

$$\begin{aligned}
&\frac{1}{\triangle x}\left[A_{i+1/2,j,k}\ \left.\frac{\partial\overline{\phi}}{\partial x}\right|_{i+1/2,j,k} - A_{i-1/2,j,k}\ \left.\frac{\partial\overline{\phi}}{\partial x}\right|_{i-1/2,j,k}\right] \\
+&\frac{1}{\triangle y}\left[A_{i,j+1/2,k}\ \left.\frac{\partial\overline{\phi}}{\partial y}\right|_{i,j+1/2,k} - A_{i,j-1/2,k}\ \left.\frac{\partial\overline{\phi}}{\partial y}\right|_{i,j-1/2,k}\right] \\
+&\frac{1}{\triangle z}\left[A_{i,j,k+1/2}\ \left.\frac{\partial\overline{\phi}}{\partial z}\right|_{i,j,k+1/2} - A_{i,j,k-1/2}\ \left.\frac{\partial\overline{\phi}}{\partial z}\right|_{i,j,k-1/2}\right] - \frac{\zeta_{i,j,k}\Gamma_{i,j,k}\ r_{p,\Gamma}}{V_{i,j,k}} \\
=&-\frac{1}{\triangle x}\left[A_{i+1/2,j,k}\ \overline{u}^{\star}_{i+1/2,j,k} - A_{i-1/2,j,k}\ \overline{u}^{\star}_{i-1/2,j,k}\right] \\
&-\frac{1}{\triangle y}\left[A_{i,j+1/2,k}\ \overline{v}^{\star}_{i,j+1/2,k} - A_{i,j-1/2,k}\ \overline{v}^{\star}_{i,j-1/2,k}\right] \\
&-\frac{1}{\triangle z}\left[A_{i,j,k+1/2}\ \overline{w}^{\star}_{i,j,k+1/2} - A_{i,j,k-1/2}\ \overline{w}^{\star}_{i,j,k-1/2}\right] + \frac{\zeta_{i,j,k}\Gamma_{i,j,k}\ r_{u,\Gamma}}{V_{i,j,k}},
\end{aligned} \tag{2.29}$$

where $\overline{u}^{\star}, \overline{v}^{\star}, \overline{w}^{\star}$ are the intermediate velocities at the cell faces and $r_{u,\Gamma}$ and $r_{p,\Gamma}$ are the velocity and pressure interface condition at $\Gamma_{i,j,k}$. The pressure gradient is discretized with second-order central differences. For non-moving boundaries $r_{u,\Gamma} = \overline{\mathbf{u}}^{\star}_{\Gamma} \cdot \mathbf{n}_{\perp}$ is set to zero. The homogeneous NEUMANN condition is imposed with $\nabla\overline{\phi} \cdot \mathbf{n}_{\perp} = \mathbf{0}$ and $r_{p,\Gamma} = 0$ at the interface. The interface treatment decouples the fluid domain from the interior of the obstacle. The discrete POISSON equation is solved for the fluid domain only. Note that with a staggered grid arrangement it is possible to have cells whose velocity control volumes are not zero but whose pressure control volume is zero and therefore does not contribute to Eq. (2.29). For such very small cells the momentum-exchange term in Eq. (2.22) ensures zero wall-normal velocity. Eq. (2.29) can be written as a linear equation system

$$\mathbf{M}\overline{\phi} = \mathbf{b} \tag{2.30}$$

and solved for $\overline{\phi}$ using a standard procedure.

Geometry representation The geometry representation is based on a level-set approach. According to [54] a level-set of the differentiable function $f : \mathbb{R}^n \to \mathbb{R}$

corresponding to a real value b is the set of points

$$\{(x_1, ..., x_n) \in \mathbb{R}^n \to \mathbb{R} : f(x_1, ..., x_n) = b\}. \tag{2.31}$$

The level-set function ϕ in the present work is discretized on the underlying numerical grid. For the cell (i, j, k) the level-set ϕ is defined as

$$\phi(x_i, y_j, z_k) = (x_i - x_{wall}) \cdot n_{\perp,x} + (y_j - y_{wall}) \cdot n_{\perp,y} + (z_j - z_{wall}) \cdot n_{\perp,z}, \tag{2.32}$$

where $(x_{wall}, y_{wall}, z_{wall})$ are the coordinates of the closest wall point. The zero-level-set iso-contour describes the immersed interface. Iso-contours with a negative sign are inside, iso-contours with a positive sign are outside the geometry. The level-set field is interpolated to the cell corners. Those cells whose corner points show a change in sign are defined to be cut cells. For the cut cells the interpolated level-set field is used to calculate the face apertures with the marching square approach [87] and volume fractions with standard tetrahedral decomposition.

Implementation At the initialization of a computation a level-set field is determined on the basis of a geometry input. Cut cells are subsequently identified and their face apertures and volume fractions are determined. For non-moving immersed interfaces this procedure is applied once at the beginning of the computation. For moving interfaces, the level-set field is transported and indicates the evolution of time interface location. The extension to moving interfaces is straightforward and not further discussed in this thesis. The general procedure for one EULER time step can be summarized as follows:

Step 1 The convective and diffusive fluxes are calculated for standard and cut cells in the same way.

Step 2 The fluxes across the cell faces of cut cells are scaled with the face apertures.

Step 3 Friction forces at the immersed interface are taken into account by adding **D** according to Eq. (2.20). **D** is added to the flux balance Eq. (2.16).

Step 4 The flux divergence is computed according to Eq. (2.16), where the volume fractions are required for a conservative formulation.

Step 5 The flux divergence of cells with a volume fraction $\zeta_{i,j,k} < 0.5$ is mixed with neighboring fluid cells of the immersed interface using the conservative mixing procedure, Eq. (2.27), with

$q^{\star}_{i,j,k} = \frac{1}{V_{i,j,k}} \int_{\partial(V_{i,j,k} \cap \Omega)} \mathbf{F} \cdot \mathbf{n}_{\perp} \, dS.$

Step 6 Zero wall-normal velocity for small cells is imposed by $\mathbf{C}$, see Eq. (2.22), and added to Eq. (2.16).

Step 7 The prediction for the pressure gradient is added to mixed flux divergence and the intermediate solution $\overline{\mathbf{u}}^{\star}_{i,j,k}$ is computed.

Step 8 In the subsequent pressure correction, the NEUMANN condition for pressure is ensured by locally changing the coefficient matrix close to the immersed boundary, see also Eq. (2.29). The resulting velocity is divergence free.

At the end of this procedure, mass and momentum conservation are locally and globally ensured. Mass conservation is ensured discretely according to the accuracy threshold chosen in the POISSON solver, up to machine precision if desired. Discrete conservation is monitored throughout a computation. A third-order RUNGE-KUTTA time integration scheme [142] is used in this thesis. In each RUNGE-KUTTA sub-step, all the steps above are invoked once. After the first RUNGE-KUTTA sub-step the mixing procedure is invoked, which improves stability and allows for the use of a COURANT-FRIEDRICHS-LEWY (CFL) number of 1.0 based on the full cell sizes. For moving interfaces the level-set field needs to be advanced in time. After each time step cut cells are identified with the instantaneous zero-level-set, and their face apertures and volume fractions are updated.

2.4 Summary

In this chapter the applied numerical simulation approach has been described. The approach uses the incompressible NAVIER-STOKES equations discretized on a staggered Cartesian grid. Turbulence is accounted for by the Adaptive Local Deconvolution Method (ALDM) [62, 64, 66]. The Wall boundary condition is applied with the Conservative Immersed Interface Method (CIIM) which is a cut cell approach. Finite-volume fluxes for cut cells and fluid cells are initially treated in

the same manner, then only cut cells are subjected to subsequent modification. Friction forces are accounted for by a friction term. The pressure boundary condition is imposed directly without computational overhead in the pressure-Poisson solver. To ensure numerical stability for small cells, the conservative mixing procedure proposed by Hu et al. [69] is employed. A level-set field describes the interface geometry, so that an extension to moving boundaries and more complex configurations is straightforward. Further details on CIIM can be also found in Ref. [100].

Chapter 3

Validation

In this chapter numerical examples are provided to illustrate the performance of the new method. Test cases have been chosen such that proof can be given with respect the requirements defined in Subchapter **1.3 Accomplishments of this Work**. All test cases are single-phase flows and have non-moving fluid-solid interfaces.

3.1 Computational Setup

For the spatial discretization ALDM is used for the convective terms, and a second-order accurate Central Difference Scheme (CDS) for the viscous terms and the pressure gradient. Note that for non-turbulent flow ALDM [64] recovers a central second-order finite-volume scheme. No wall-modeling is used within the validation part to offer an unbiased view on CIIM and its performance. Time advancement is performed using a third-order explicit three step Runge-Kutta scheme [142]. The pressure Poisson equation is solved using a Bi-Conjugate Gradient Stabilized (BiCGStab) iterative solver. All computations are carried out at a CFL number of 1.0 based on the full cell scale. More computational details are given in the corresponding test case sections.

3.2 Definition of Reference Quantities

Incompressible flows with constant density and without heat transfer are primarily characterized by the REYNOLDS number, defined as

$$Re = \frac{\rho_{ref} u_{ref} l_{ref}}{\mu_{ref}}, \tag{3.1}$$

where ρ_{ref} is the reference density and μ_{ref} is the reference dynamic viscosity. The test case related reference velocity u_{ref} and the reference length scale l_{ref} are given in each corresponding test case section. The velocity vector is defined to be

$$\mathbf{u} = \begin{pmatrix} u \\ v \\ w \end{pmatrix}, \tag{3.2}$$

where u, v, w are the streamwise, crossflow and spanwise velocity components. Instantaneous velocities are normalized with u_{ref}

$$\frac{u}{u_{ref}}, \ \frac{v}{u_{ref}}, \ \frac{w}{u_{ref}}. \tag{3.3}$$

Time averaged quantities are indicated by $\langle \cdot \rangle$. Applied to the first order velocity statistics which are normalized with u_{ref} these become

$$\frac{\langle u \rangle}{u_{ref}}, \ \frac{\langle v \rangle}{u_{ref}}, \ \frac{\langle w \rangle}{u_{ref}}. \tag{3.4}$$

Based on the time-averaged or non-averaged velocity field the time-averaged or non-averaged vorticity is defined to be

$$\langle \omega \rangle = \nabla \times \langle \mathbf{u} \rangle \text{ or } \omega = \nabla \times \mathbf{u}. \tag{3.5}$$

Similarly the shear is defined to be

$$\langle \tau \rangle = \nu \nabla \langle \mathbf{u} \rangle \text{ or } \tau = \nu \nabla \mathbf{u}. \tag{3.6}$$

Fluctuations with respect to the time-averaged mean are indicated by $\cdot'$. The second-order velocity statistics in time, i.e. the velocity fluctuations, are normalized with u_{ref}^2.

$$\frac{\langle u'u' \rangle}{u_{ref}^2}, \ \frac{\langle v'v' \rangle}{u_{ref}^2}, \ \frac{\langle w'w' \rangle}{u_{ref}^2}. \tag{3.7}$$

They are used to determine the Turbulent Kinetic Energy (TKE)

$$tke = \frac{\langle u'u' \rangle + \langle v'v' \rangle + \langle w'w' \rangle}{2u_{ref}^2}. \tag{3.8}$$

The normalized crossflow correlations are defined to be

$$\frac{\langle u'v' \rangle}{u_{ref}^2}, \ \frac{\langle u'w' \rangle}{u_{ref}^2}, \ \frac{\langle v'w' \rangle}{u_{ref}^2}. \tag{3.9}$$

Unsteady flow phenomena are characterized by the Strouhal number

$$St = \frac{f l_{ref}}{u_{ref}}, \tag{3.10}$$

where f is a characteristic frequency of the considered test case. The frequency f is determined with a Fast Fourier Analysis of an instantaneous velocity time signal.

For evaluating the representation of the flow physics at the interface the time-averaged pressure coefficient is needed. The dimensionless time-averaged pressure coefficient is defined to be

$$\langle C_p \rangle = \frac{\langle p \rangle - p_\infty}{0.5 \rho u_\infty^2}, \tag{3.11}$$

where $\langle p \rangle$ is the time-averaged local pressure and p_∞, ρ_∞ and u_∞ are the pressure, density and velocity in the freestream at infinity. For the same purpose, the friction coefficient is employed

$$\langle C_f \rangle = \frac{\langle \tau_w \rangle}{0.5 \rho_\infty \langle u \rangle^2}, \tag{3.12}$$

where $\langle \tau_w \rangle$ is the time-averaged wall shear stress defined in Eq. (2.18)[4]. With $\langle C_f \rangle = 0$ the separation angle $\langle \theta_{sep} \rangle$ is defined.

Global integral quantities like the drag and lift coefficient are used for the investigation of flows around bodies of arbitrary shape. The time-averaged drag

[4]here defined with the time averaged velocity $\langle u \rangle$

coefficient per unit length is defined to be

$$\langle C_D \rangle = \frac{\langle F_D \rangle}{0.5 \rho u_\infty^2 l_{ref}}, \tag{3.13}$$

$\langle F_D \rangle$ is the force in streamwise direction and consists of the friction force $\langle F_{D,f} \rangle$ and the pressure force $\langle F_{D,p} \rangle$ acting in streamwise direction at the immersed interface. $\langle F_{D,f} \rangle$ is determined by integrating the streamwise component of the friction term $\mathbf{D}$, see Eq. (2.20), over all cut cells. For $\langle F_{D,p} \rangle$, the pressure force is integrated over all cut cells. Similarly, the maximum and the root-mean-square (rms) lift coefficient are defined

$$C_{L,max/rms} = \frac{F_{L,max/rms}}{0.5 \rho u_\infty^2 l_{ref}}, \tag{3.14}$$

where $F_{L,max/rms}$ is the force in transverse direction and consists of $F_{L,p,max/rms}$ and $F_{L,f,max/rms}$.

3.3 Inclined Channel Flow at $Re = 20$

The first test case is the laminar flow through a plane channel that is inclined at $\beta = 20°, 30°, 40°$ and $50°$ with respect to the grid. Based on the channel half height h and the mean velocity u_b, the Reynolds-number is $Re = 20$. This test case in particular validates the viscous term of CIIM. The computational domain is shown in Fig. 3.1.

The length of the channel is at least ten times the channel height. The spanwise extent is one channel height. A parabolic velocity profile is defined at the inlet boundary with the velocity aligned parallel to the axis of the channel. At the outlet a pressure boundary condition is imposed. In spanwise direction periodic boundary condition are used. At the walls of the channel, a no-slip condition is imposed by CIIM.

The order of accuracy is determined from error estimates of the velocity profiles on six successively refined equidistant grids, see Table 3.1. N_x and N_y are the number of cells in the respective direction of the computational domain.

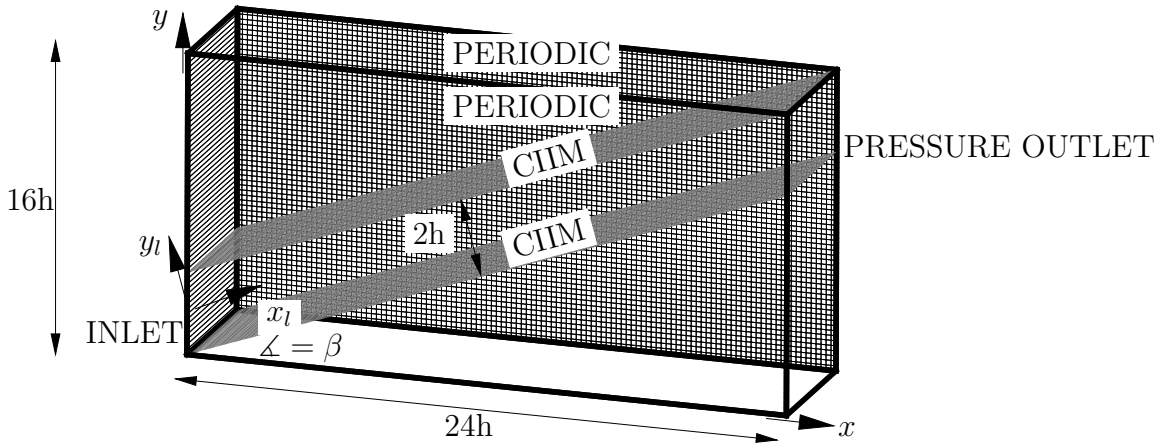

FIGURE 3.1: Computational setup for the inclined channel flow at $Re = 20$.

TABLE 3.1: Grids and number of computational cells over channel height $2h$ for the inclined channel flow at $Re = 20$.

N_x x N_y	n_{20°	n_{30°	n_{40°	n_{50°
40 x 60	11	13	13	14
60 x 90	16	17	17	18
120 x 180	25	27	27	28
180 x 270	35	37	37	39
360 x 540	64	69	69	72

To compute the error, the following equation is applied to compare the velocity profile of the computations to the analytical profile at half the channel length

$$\epsilon = \left(\frac{1}{n} \sum_{r=1}^{n} (u_r^{numerical} - u_r^{analytical})^2 \right)^{1/2}, \tag{3.15}$$

where n is the total number of cells across the channel. In Fig. 3.2 the error of the velocity profile with respect to the analytical profile for the different grid resolutions and inclination angles is shown. For all inclination angles the error decreases with about second-order. CIIM is compared to a simple blocking method [65] in Fig. 3.3(a). The blocking method shows a higher error than CIIM and only first-order convergence. In Fig. 3.3(b) the velocity profiles with CIIM for different grid resolutions are compared to the analytical profile for $\beta = 20^\circ$. The highest

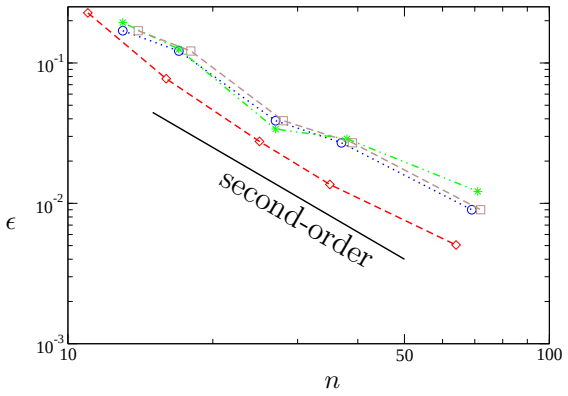

FIGURE 3.2: Error for different grid resolutions and different inclination angles for the inclined channel flow at $Re = 20$ (——◇: $\beta = 20°$, · · · · ·○: $\beta = 30°$, — · ·∗: $\beta = 40°$, ——□: $\beta = 50°$).

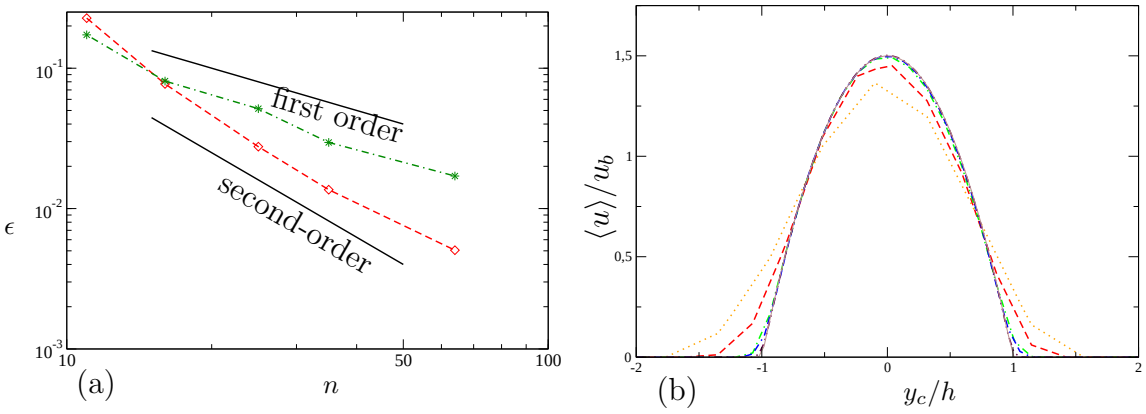

FIGURE 3.3: (a): Error for different grid resolutions with an inclination angle $\beta = 20°$ for CIIM and for the blocking method (——◇: with CIIM, · — ·∗: with blocking method). (b): streamwise velocity profiles for the inclined channel flow at $Re = 20$ $\beta = 20°$ with CIIM for different grid resolutions (· · · · ·: $n = 11$, ——: $n = 16$, · — ·: $n = 25$, · — —: $n = 35$, — · ·: $n = 64$, ———: analytical profile).

error occurs at the immersed interface and amounts to $1-2\%$ in the first full fluid cell on the fine grid ($n = 64$) in normal direction of the interface. Already for moderate resolutions the global agreement with the analytical solution is good.

3.4 Flow over a Square Cylinder at $Re = 100$

Two square cylinder cases are investigated: a) the non-inclined square cylinder (see Fig. 3.5(a)) b) a square cylinder inclined by $\alpha = 45°$ with respect to the incoming flow (see Fig. 3.5(b)). At a REYNOLDS-number $Re = 100$ based on the projected cylinder width d in the streamwise direction and the free stream velocity

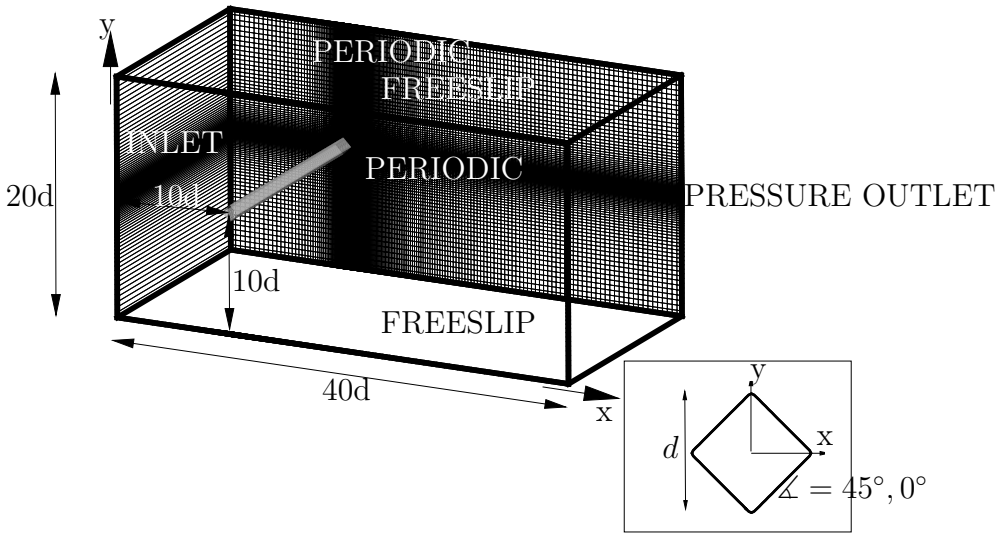

FIGURE 3.4: Computational setup for the 2-D flow over an inclined and a non-inclined square cylinder at $Re = 100$ (every ninth computational cell is shown, zoom on cylinder cross-section).

u_∞ the flow over a square cylinder is unsteady, two-dimensional and laminar. The computational setup used for all cylinder flow computations follows that of Fig. 3.4. Note that for both cases the cylinder boundaries do not coincide with the grid lines.

3.4.1 Non-inclined Square Cylinder

Vortex shedding occurs at a $St = 0.151$ based on the shedding frequency. The frequency in this and the following cylinder cases are determined through a FOURIER transform of a velocity time signal obtained in the wake of the cylinder. The computed STROUHAL-number agrees well with the experiments conducted by Okajima [117].

The STROUHAL number, the time-averaged drag coefficient per unit length $\langle C_D \rangle$ and the maximum lift coefficient per unit length $C_{L,max}$ are compared to results from literature in Table 3.2.

The lift coefficient agrees very well with the simulation by Franke et al. [45], whereas the drag coefficient of the present calculation is slightly lower. All in all,

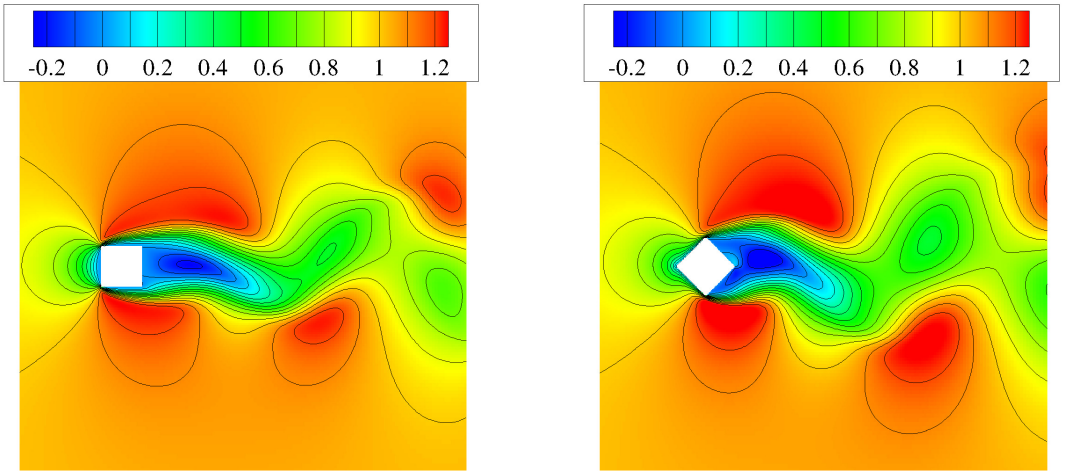

FIGURE 3.5: (a) Streamwise velocity and velocity contour lines for the flow over a non-inclined square cylinder and (b) 45°-inclined square cylinder at $Re = 100$.

TABLE 3.2: Inclination angle, time-averaged drag coefficient, maximum lift coefficient, root-mean-square lift coefficient and STROUHAL number for a non-inclined and 45°-inclined square cylinder flow at $Re = 100$.

Study	α	$\langle C_D \rangle$	$C_{L,max}$	$C_{L,rms}$	St
Okajima [117], experiment	0°	-	-	-	0.149
Davis and Moore [30], simulation	0°	1.63	-	-	0.152
Franke et al. [45], simulation	0°	1.61	0.27	-	0.154
Sohankar et al. [150], simulation	0°	1.48	-	0.18	0.150
Simulation with CIIM ($n = 76$)	0°	1.57	0.27	0.19	0.151
Sohankar et al. [150], simulation	45°	1.72	-	0.48	0.182
Simulation with CIIM ($n = 79$)	45°	1.76	-	0.49	0.184

the differences are well within the range of variation for numerical and experimental data reported in literature [175].

To determine the order of grid-convergence of CIIM also for this test case, the drag and the lift coefficient have been calculated on five grids not aligned to the cylinder, with different resolutions and the same domain size. All grids are refined according to a hyperbolic tangent function centered around the xz-, yz- symmetry planes of the cylinder. Grid parameters are summarized in Table 3.3.

The error is calculated with respect to the solution on the finest grid. Fig. 3.6 shows a double-logarithmic plot of the errors for $\langle C_D \rangle$ and $C_{L,max}$. n is the number of cells over the projected cylinder width. The error decreases with approximately second-order.

TABLE 3.3: Grids and number of computational cells n over the projected cylinder width for the non-inclined and 45°-inclined square cylinder flow at $Re = 100$.

N_x x N_y	$n_{0°}$	$n_{45°}$
128 x 64	15	17
192 x 96	23	25
256 x 128	34	36
384 x 192	51	53
512 x 256	76	79

3.4.2 45°-inclined Square Cylinder

This test case evaluates the influence of the geometry representation given by the level-set field on the accuracy. The level-set approach is known to smoothen sharp corners. The same grids are used as for the non-inclined case (see Table 3.3). The STROUHAL-number, the time-averaged drag coefficient per unit length $\langle C_D \rangle$ and the root-mean-square lift coefficient per unit length $C_{L,rms}$ of the current calculation are compared to the results of Sohankar et al. [150] in Table 3.2. The simulations of Sohankar et al. [150] have been carried out on body-fitted grids. The agreement with the present results is good, which gives direct evidence of the accuracy of the level-set description. The order of grid convergence is determined with the grids shown in Table 3.3. Fig. 3.6 shows a double-logarithmic plot of the errors for $\langle C_D \rangle$ and $C_{L,rms}$. n is the number of cells over the projected cylinder width. Note that about second-order convergence rate is also achieved for the inclined square cylinder.

3.5 Flow over a Circular Cylinder

In the following examples the flow over a circular cylinder for a wide range of REYNOLDS-numbers is investigated. The computational setup is shown in Fig. 3.7. The circular cylinder is a standard configuration for testing Immersed Boundary and Immersed Interface Methods and a huge amount of reference data are available from literature. The REYNOLDS-numbers of all cases is based on the cylinder diameter d and the free stream velocity u_∞.

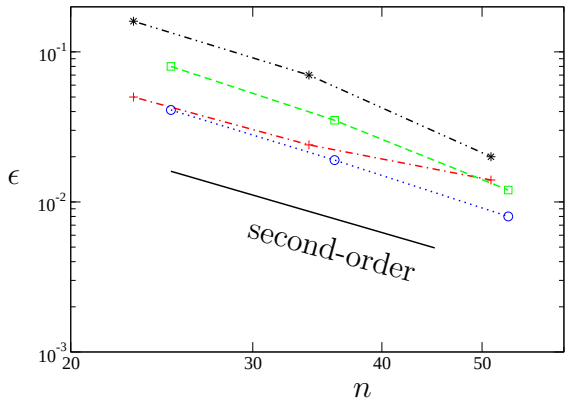

FIGURE 3.6: Error in $\langle C_D \rangle$ ($\cdots\circ$) and $C_{L,max}$ ($--\square$) for the flow over a non-inclined square cylinder and error in $\langle C_D \rangle$ ($-\cdot\diamond$) and $C_{L,rms}$ ($-\cdot\cdot\triangle$) for the flow over a 45°-inclined square cylinder at $Re = 100$ calculated on different grids.

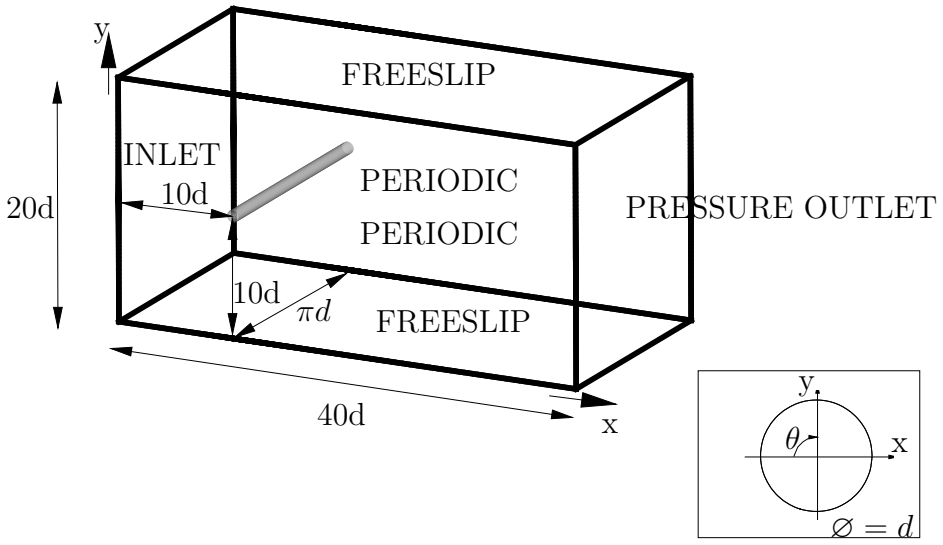

FIGURE 3.7: Computational setup for circular cylinder flow.

3.5.1 Flow over a Circular Cylinder at $Re = 40$

At $Re = 40$ laminar separation occurs and exhibits a two-dimensional symmetric wake. The calculation is carried out on a locally refined grid close to the immersed boundary with a total number of 175,000 computational cells and 72 computational cells over the cylinder diameter. The surface pressure coefficient $\langle C_p \rangle$ is compared with experimental and numerical results in Fig. 3.8. Note that the calculation with CIIM shows a smooth $\langle C_p \rangle$ profile unlike that often reported for discrete forcing approaches [20, 74, 111].

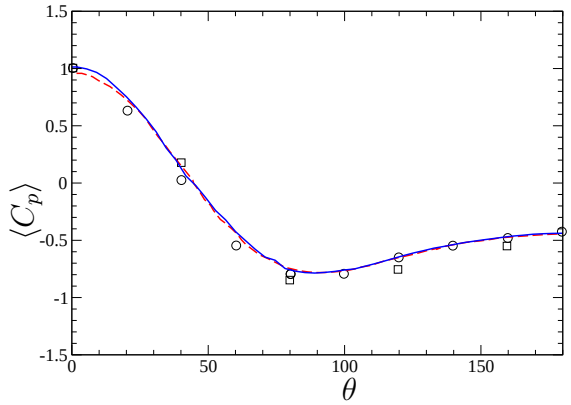

FIGURE 3.8: The pressure coefficient $\langle C_p \rangle$ along the surface of a circular cylinder at $Re = 40$ ($\theta = 0$ in the stagnation point; □: experimental data Grove [56], ∘: experimental data Thom [163] ——: Dröge [35], ———: present method).

TABLE 3.4: Drag coefficient, pressure drag coefficient, friction drag coefficient, separation angle and recirculation bubble length for the circular cylinder flow at $Re = 40$.

Study	$\langle C_D \rangle$	$\langle C_{D,p} \rangle$	$\langle C_{D,f} \rangle$	$\langle \theta_{sep} \rangle$	$\langle L_{rec}/d \rangle$
Tritton [167], experiment	1.58	-	-	-	-
Grove et al. [56], experiment	-	0.92	-	137.2°	-
Coutanceau et al. [29], experiment	-	-	-	126.5°	2.13
Dennis and Chang [32], simulation	1.52	0.99	0.524	126.2°	2.35
Ye et al. [182], simulation	1.52	-	-	-	2.27
Dröge [35], simulation	1.58	1.02	0.56	126.67°	2.22
Simulation with CIIM ($n = 72$)	1.56	1.04	0.52	126.4°	2.28

The drag, the separation angle and the length of the recirculation bubble compare well with reference data both from experiments and other simulations, see Table 3.4. The agreement for the individual contributions of pressure and friction to the drag coefficient is also good.

3.5.2 Flow over a Circular Cylinder at $Re = 100$

At $Re = 100$ the flow is unsteady, two-dimensional and laminar, see Fig. 3.9(a). For CIIM flow separation occurs at a an angle of 119° measured from the stagnation point. Vortex shedding occurs at $St = 0.165$. A comparison of $\langle C_D \rangle$, $C_{L,max}$ and St for the present results with experimental and numerical results is given in Table 3.5. All results are well within the range reported in the literature.

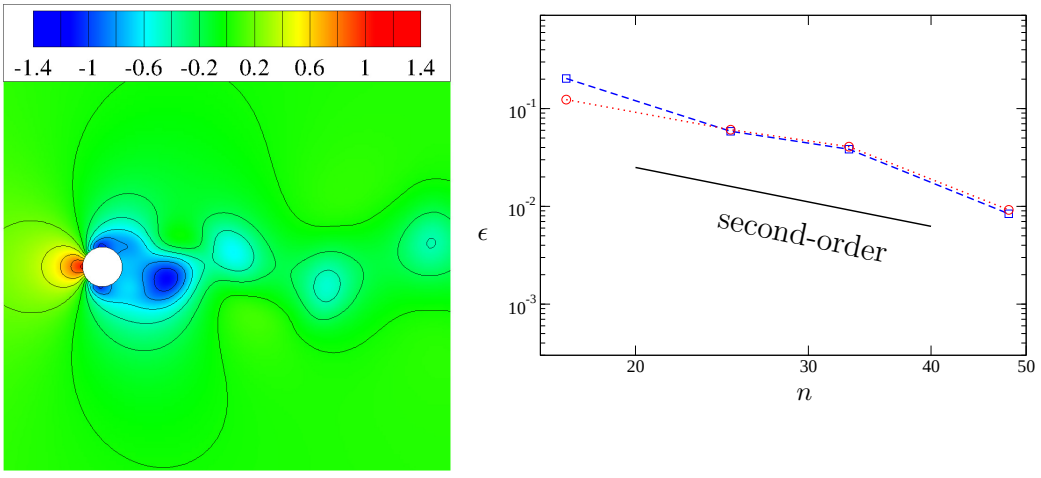

(a) (b)

FIGURE 3.9: (a): Contour map of the pressure coefficient C_p for the flow over a circular cylinder at $Re = 100$. (b): Error in $\langle C_D \rangle$(−−□) and C_L(——○) for the flow over a circular cylinder at $Re = 100$ calculated on different grids.

TABLE 3.5: Drag coefficient, maximum lift coefficient, separation angle and STROUHAL number for the circular cylinder flow at $Re = 100$.

Study	$\langle C_D \rangle$	$C_{L,max}$	$\langle \theta_{sep} \rangle$	St
Tritton [167], experiment	1.26	-	-	-
Henderson [61], experiment	1.3	-	122°	-
Fey et. al [41], experiment	-	-	-	0.165
Kim et. al [77], simulation	1.33	0.32	-	0.165
Dröge [35], simulation	1.24	0.30	117°	0.165
Present, simulation ($n = 76$)	1.26	0.34	119°	0.165

In this investigation the influence of the amount of mixing, i.e. the effect of the mixing threshold ζ_{crit}, on the accuracy of the solution is analyzed. A variation of the small-cell mixing criterion down to $\zeta_{crit} = 0.2$ leads to a decrease of 0.9% for the drag coefficient and a variation up to $\zeta_{crit} = 0.7$ to an increase of 1.6% with respect to the CIIM-standard solution. The amount of mixing was chosen as best compromise between accuracy and overall efficiency and does not significantly affect the computed flow field.

For a convergence study calculations have been performed on five grids with different resolution. All grids have been refined according to a tangent hyperbolic function centered at the xz-, yz- symmetry planes of the cylinder. The different grid resolutions are summarized in Table 3.6, where the finest grid is taken as reference for the error estimation. For $\langle C_D \rangle$ and $C_{L,max}$ second-order accuracy are found, see Fig. 3.9(b).

TABLE 3.6: Grids and number of computational cells n along the diameter for the circular cylinder flow at $Re = 100$.

N_x x N_y	n
128 x 64	15
192 x 96	23
256 x 128	34
384 x 192	51
512 x 256	76

3.5.3 Flow over a Circular Cylinder at $Re = 3900$

At $Re = 3900$ the separated, unsteady laminar shear layers undergo transition in the near wake of the cylinder. An accurate representation of the flow at the immersed interface is crucial for a correct prediction of the global flow physics, making this test case especially suitable for the assessment of CIIM.

This case is widespread in literature and can be considered as an established reference, despite the discrepancies of published results and sometimes not very clearly specified configurations. Many DNS (Dröge [35]; Ma et al. [91]) and LES (Breuer [9]; Fröhlich et al. [49]; Kravchenko and Moin [82]; Franke and Frank [44]; Mahesh et al [92]; Park et al. [123]; Parnaudeau et al. [124]) have been conducted for this flow.

In order to address the particular concern of accurate boundary treatment, this investigation includes a quantitative comparison of statistical results of two implicit LES with ALDM, one on a curvilinear body-fitted grid with a usual formulation of the wall-boundary condition, and one on a Cartesian grid with CIIM.

Reference Data and Previous Studies The pressure measurements of Norberg (data extracted from Kravchenko and Moin [82]) provide the only experimental surface pressure data known to the author. Turbulent statistics in the very near wake of the cylinder have been measured by Lourenco and Shih [89]) using PIV. These data are commonly used in numerical studies for validation (e.g. Franke and Frank [44]; Dröge [35]) and investigation (e.g. Kravchenko and Moin [82], Ma et al. [91], Parnaudeau et al. [124]), yet their validity in the recirculation zone is often subject to discussion. Beaudan and Moin [7] attribute discrepancies in the velocity profiles to asymmetric experimental conditions. This disagreement is confirmed by

Mittal and Moin [104] as well as by Kravchenko and Moin [82]. Kravchenko and Moin [82] further argue that observed differences can be attributed to transitional effects in the separating shear layers of the experiment. Norberg [116] showed that aspect ratios of 60-70 are required to obtain results unaffected by cylinder length under experimental conditions. Szepessy and Bearman [157] report differences in the vortex formation length for different aspect ratios. In consideration of these findings the aspect ratio of 21 in the experiments of Lourenco and Shih [89] appears to be rather small.

However, Parnaudeau et al. [124], whose PIV data are also used for comparison here, have the same aspect ratio in their experiment as Lourenco and Shih [89] but obtain different results. Furthermore, the PIV data of the experiments of Parnaudeau et al. [124] for mean velocity on the wake centerline are consistent with the hot-wire measurements of Ong and Wallace [118] but inconsistent with their own hot-wire data. Due to these discrepancies, both the PIV data of Lourenco and Shih [89] and Parnaudeau et al. [124] for the very near wake and the hot-wire measurements of Ong and Wallace [118] for the near wake comparisons are considered.

Computational Details Calculations were done on a locally refined grid with a total of 7 million cells, see Fig 3.10 and a curvilinear body-fitted grid with a total of 6 million cells and an O-H topology, see Fig. 3.11. The cell size of all cells at the fluid-solid interface is $\triangle x = \triangle y = 0.0025/d$, so that the resolution is similar to the LES of Franke and Frank [44] and Fröhlich et al. [49]. The first computational cell in the wall normal direction is within the viscous sublayer of the cylinder. At the boundary of the obstacle a viscous-wall boundary condition is prescribed for the calculation on the curvilinear grid, and for the calculation on the Cartesian grid the immersed interface condition is imposed by CIIM. In the region 1.5d away from the fluid-solid interface, the resolution is 3 timer coarser than at the interface. The region of the turbulent wake is resolved with a 9 times coarser grid than at the interface. The Cartesian grid was automatically generated with a local mesh refinement algorithm based on ghost cells in the grid transition regions. Data are assigned to ghost cells by a third-order conservative interpolation scheme. This scheme ensures mass and momentum conservation. The computational stencil does not change at grid transition. All cut cells are on the finest grid level.

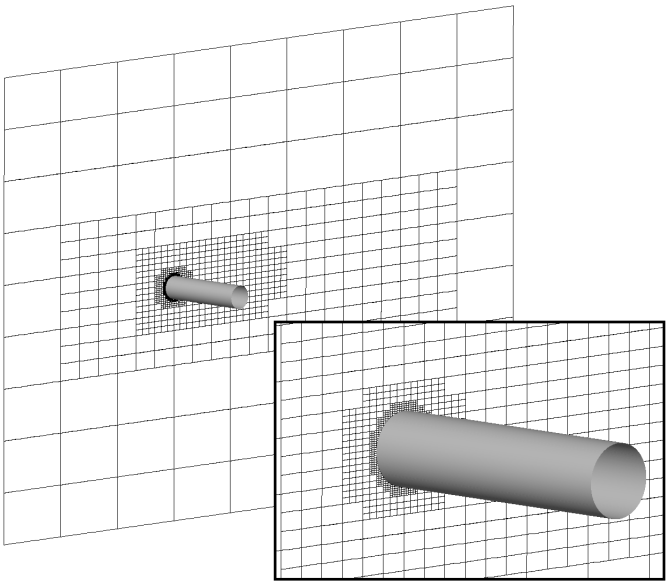

FIGURE 3.10: Locally refined grid for the circular cylinder flow at $Re = 3900$ (every ninth computational cell is shown).

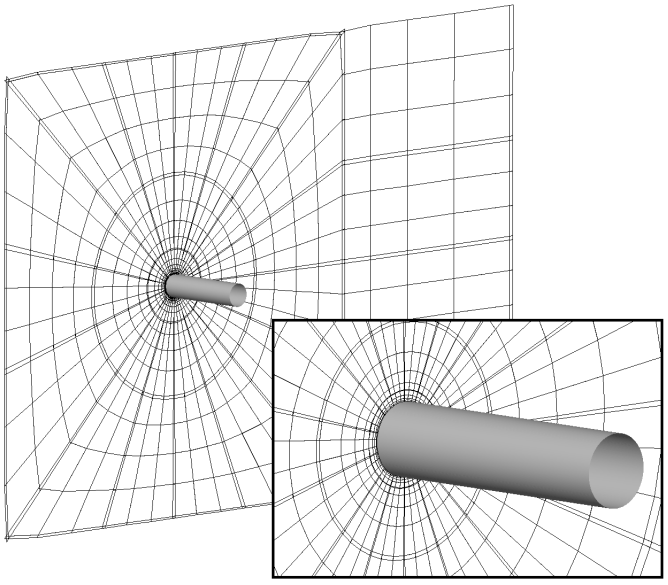

FIGURE 3.11: Curvilinear grid for the circular cylinder flow at $Re = 3900$ (every ninth computational cell is shown).

For both simulations the SGS modeling is realized with ALDM. ALDM has been developed primarily for Cartesian grids due to the superior computational efficiency and because Cartesian grids allow for an easy control of the truncation error (see also Section 2).

ALDM has also been translated to general curvilinear coordinates and implemented in a finite-volume solver for the incompressible NAVIER-STOKES equations

on three-dimensional block-structured, body-fitted grids [67]. Boundary conditions are imposed in a natural way on body-fitted grids, which facilitate accurate numerical predictions of the wall-layer. The simulation code Large-Eddy Simulation On Curvilinear Coordinates (LESOCC2) [68] employs non-orthogonal, boundary-fitted, block-structured grids. Boundary-fitted block-structured grids can offer considerable computational advantages for predicting wall-bounded turbulence: Imposing no-slip wall boundary conditions is straightforward for grid-aligned domain boundaries. The algorithm uses a cell-centered variable arrangement and Cartesian velocity components. The convective fluxes are discretized by ALDM in an algorithmically simplified version (SALD) [64]. SALD preserves the modeling capability of ALDM while significantly reducing computational costs. Another advantage of SALD is that it allows for a straightforward application to curvilinear grids as the reconstruction of the unfiltered solution at cell faces by HARTEN-type deconvolution polynomials can be done dimension by dimension [67]. Viscous fluxes are discretized by centered differences. Numerical stability for the collocated grid arrangement is maintained by employing a momentum–interpolation technique.

Instantaneous Flow Field Fig. 3.12 gives an impression of the instantaneous turbulent wake behind the cylinder. On both, the upper and the lower side of the cylinder, a long shear layer with a longitudinal extent of one cylinder diameter separates, see also Fig. 3.13. Instabilities of the shear layers lead to the development of vortices which mix in the primary VON KÁRMÁN vortices before propagating downstream as VON KÁRMÁN vortex street. A good qualitative agreement with the investigations of Ref. [24, 49] is observed. However, laminar-turbulent transition of the separated shear-layer on the body-fitted grid occurs closer to the cylinder than on the Cartesian grid.

Instantaneous streamwise, cross-flow and spanwise velocity fields in the plane $y = 0$ of the first nine diameters of the cylinder are shown in Figs. 3.14 – 3.16. An unsteady recirculation region in Fig. 3.14 and alternating regions of positive and negative cross-flow vortices in Fig. 3.15 corresponding to the VON KÁRMÁN vortices can be observed. The wake appears to be highly turbulent and three-dimensional. Both large and small-scale structures are present in the wake. Flow structures tend to increase in size downstream, see also Fig. 3.16 showing the instantaneous spanwise velocity. However, small scale fluctuations are present even 9 diameters

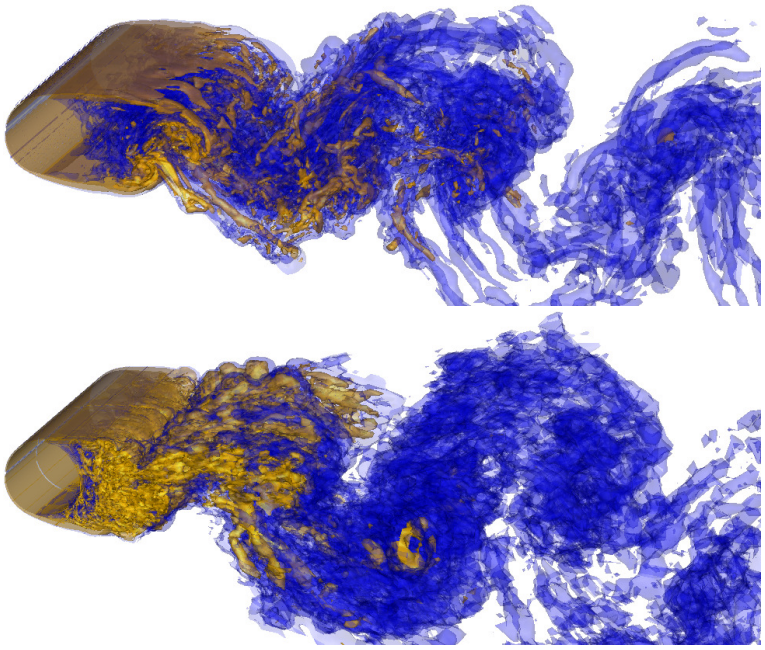

FIGURE 3.12: Isometric view on isosurfaces of instantaneous vorticity magnitude $\omega d/u_\infty = 3$ and $\omega d/u_\infty = 10$ for the circular cylinder flow at $Re = 3900$ on a Cartesian grid (top) and body-fitted grid (bottom).

downstream of the cylinder. Similar observations have been made by Kravchenko and Moin [82]. This separation of scales downstream seems more prevalent and regions of dense contour lines implying laminar-turbulent transition appear further away from the cylinder for the simulation on the Cartesian grid. This supports the previous findings.

Isosurfaces of the streamwise vorticity in the planes $y = 0$ and $z = 0$ are shown in Fig. 3.17(a) and (b). For both simulations the quasiperiodic streamwise vortical structures agree both in size and shape with the experimental findings of [94, 179]. The spanwise length scales are of the order of one-fourth to one-half with respect to the cylinder diameter (see Fig. 3.13) and correspond to the scale estimation of Mansy et al. [94, 179]

$$\frac{\lambda_z}{d} \sim 25Re^{-0.5} \Rightarrow \frac{\lambda_z}{d}|_{Re=3900} = 0.4. \tag{3.16}$$

Averaged Flow Field For a quantitative validation, turbulence statistics are sampled over 50 shedding cycles after steady vortex shedding was established and are averaged in spanwise direction.

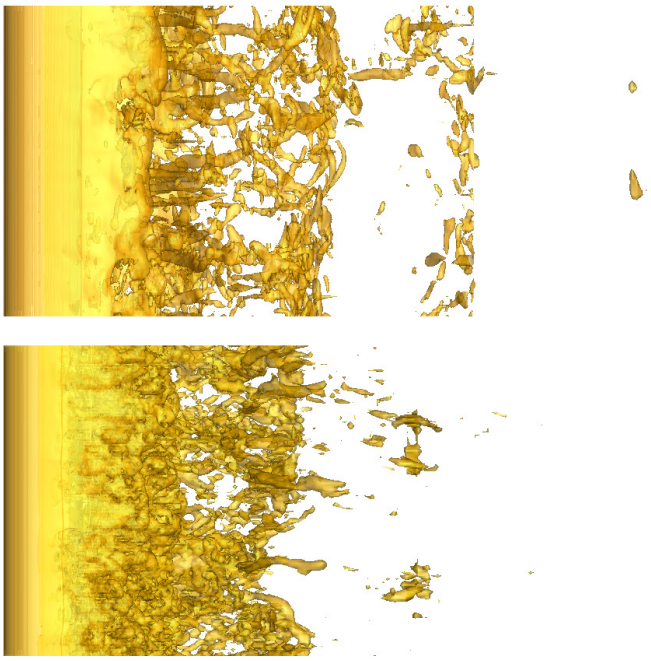

FIGURE 3.13: Topview on isosurfaces of the instantaneous vorticity magnitude $\omega d/u_\infty = 10$ for the circular cylinder flow at $Re = 3900$ on a Cartesian grid (top) and a body-fitted grid (bottom).

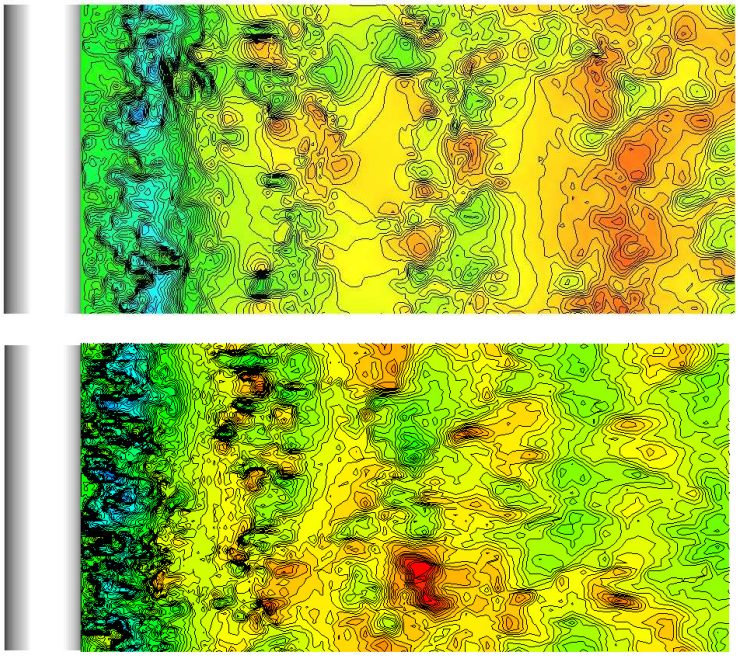

FIGURE 3.14: 52 contours from -1.5 to 1.5 of the instantaneous streamwise velocity in the plane $y = 0$ of the circular cylinder flow at $Re = 3900$ on a Cartesian grid (top) and a body-fitted grid (bottom).

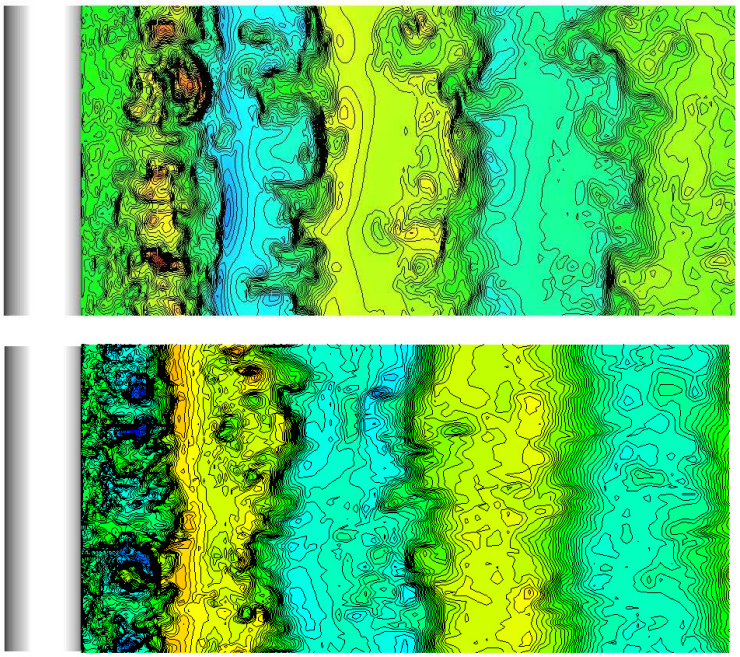

FIGURE 3.15: 52 contours from -1.5 to 1.5 of the instantaneous crossflow velocity in the plane $y = 0$ for the circular cylinder flow at $Re = 3900$ on a Cartesian grid (top) and on a body-fitted grid (bottom).

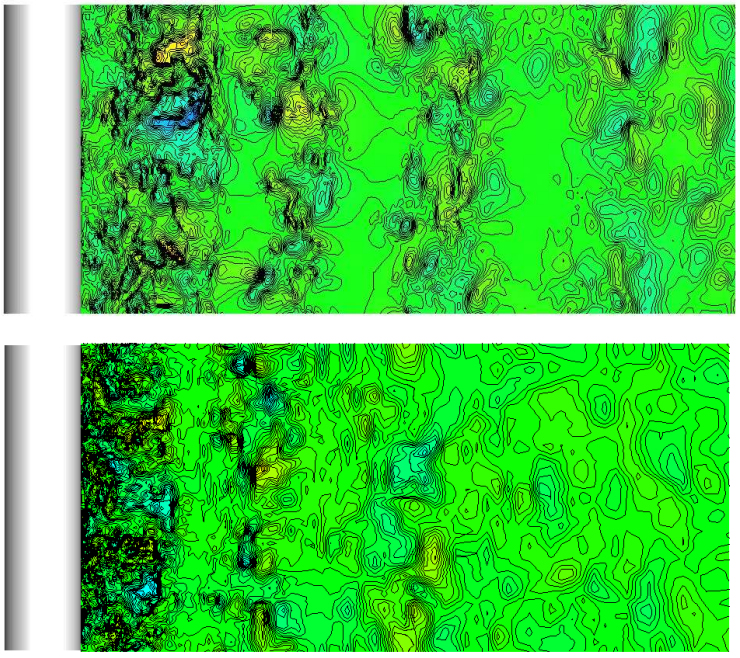

FIGURE 3.16: 52 contours from -1.5 to 1.5 of the instantaneous spanwise velocity in the plane $y = 0$ of the circular cylinder flow at $Re = 3900$ on a Cartesian grid (top) and on a body-fitted grid (bottom).

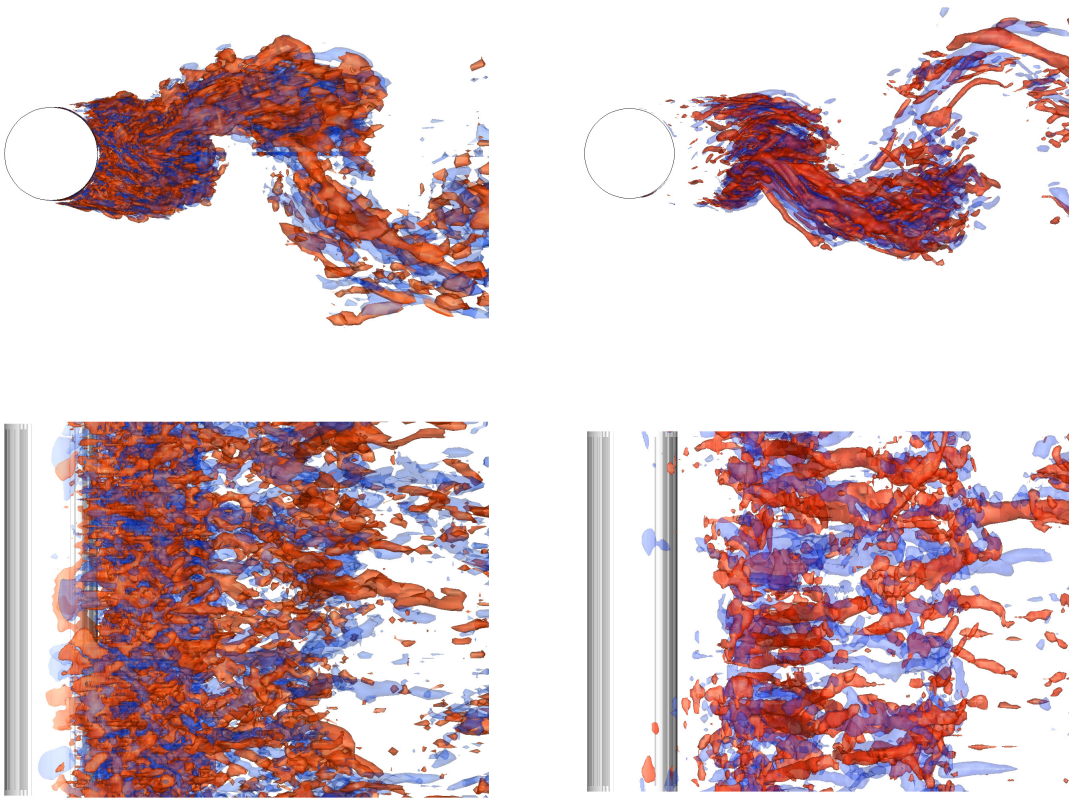

(a) (b)

FIGURE 3.17: Streamwise vorticity-isosurfaces $\pm 5.5\ s^{-1}$ of the circular cylinder flow at $Re = 3900$ on a Cartesian grid (a) and on a body-fitted grid (b).

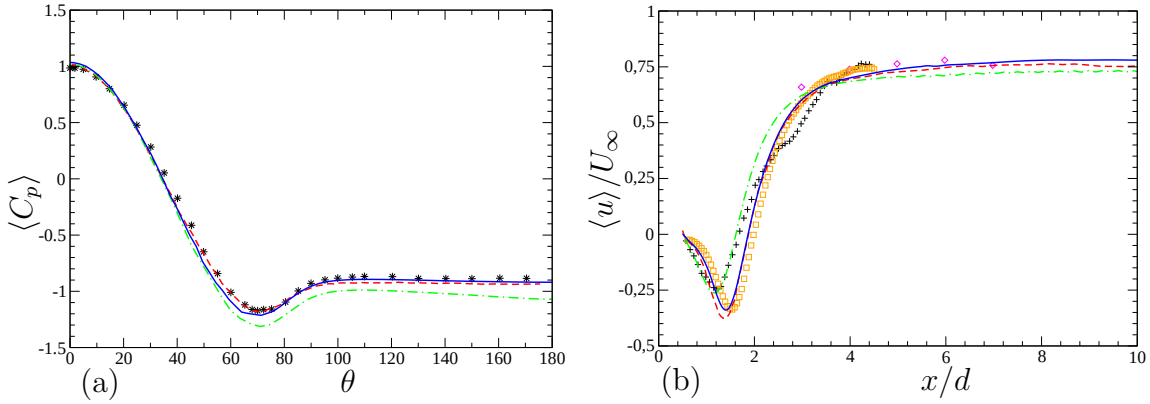

FIGURE 3.18: (a): $\langle C_p \rangle$ along the cylinder surface for the circular cylinder flow at $Re = 3900$ ($\theta = 0$ in the stagnation point) and (b) $\langle u \rangle / U_\infty$ on the centerline of the cylinder for the circular cylinder flow at $Re = 3900$ ($*$: experimental data Norberg extracted from Kravchenko and Moin [82], $+$: experimental data of Lourenco and Shih [89] ,$\square$: experimental data of Parnaudeau [124] ,$--$: Kravchenko and Moin [82], $\cdot - \cdot$: ILES on a body-fitted grid, ——: ILES on a Cartesian grid + CIIM).

The pressure coefficient $\langle C_p \rangle$ shows good agreement with the experimental results of Norberg [extracted from Ref. [82]] and numerical results of Kravchenko and Moin [82], see Fig. 3.18(a). The results of the ILES on the curvilinear grid do not fully recover the recirculation zone. Note that the calculation with CIIM shows a smooth $\langle C_p \rangle$ profile unlike that often reported for discrete forcing approaches (Cheny and Botella [20]; Kang et al. [74]; Muldoon and Acharya [111]).

The mean streamwise velocity along the centerline is shown in Fig. 3.18(b). The recirculation zone in the experiments of Lourenco and Shih [89] is shorter than in the experiments of Parnaudeau et al. [124]. The calculation on the curvilinear grid shows good agreement with the results of Lourenco and Shih [89] while the calculation on the Cartesian grid shows good agreement with the experimental results of Parnaudeau et al. [124] and the LES of Kravchenko and Moin [82]. The dip at $x/d = 3$ seen in the experiments of Lourenco and Shih [89] is neither reproduced by the experiments of Parnaudeau et al. [124] nor by any simulation reported in the literature.

Figs. 3.19 compare the statistics in the very near wake of the cylinder with the experiments of Lourenco and Shih (1993) and Parnaudeau et al. [124]. Fig. 3.19(a) shows velocity profiles at four different downstream locations ($x/d = 0.58, 1.06,$ $1.54, 2.02$) of the mean streamwise velocity $\langle u \rangle / U_\infty$. A strong velocity deficit occurs in the region of the recirculation bubble. The mean velocity-profile shows a U-shape close to the cylinder which evolves towards a V-shape further downstream. At $x/d = 0.58$ the implicit LES on the curvilinear grid and the data of Lourenco and Shih [89] are in good agreement. Please note the different shape of the profiles at $x/d = 1.06$ for the two experiments. The results of Lourenco and Shih [89] show a V-shape whereas Parnaudeau et al. [124] show a U-shape profile. Both shapes have also been observed in various numerical studies. A V-shape profile at $x/d = 1.06$ along with a longer recirculation length has been observed by e.g. Kravchenko and Moin [82], Parnaudeau et al. [124] and also in the present implicit LES on the Cartesian grid. On the other hand, the present calculation on the curvilinear grid agrees with the results of Lourenco and Shih [89] and the LES of Fröhlich et al. [49] and Fröhlich et al. [47]. Ma et al. [91] were able to reproduce both shapes by DNS, where doubling the spanwise extent of the domain changes the mean profile form U-shape to V-shape. Results for the mean normalized transversal velocity $\langle v \rangle / U_\infty$ are shown in Fig. 3.19(b). It should be mentioned that the profiles of Lourenco and Shih are shifted such that $\langle v \rangle = 0$ is

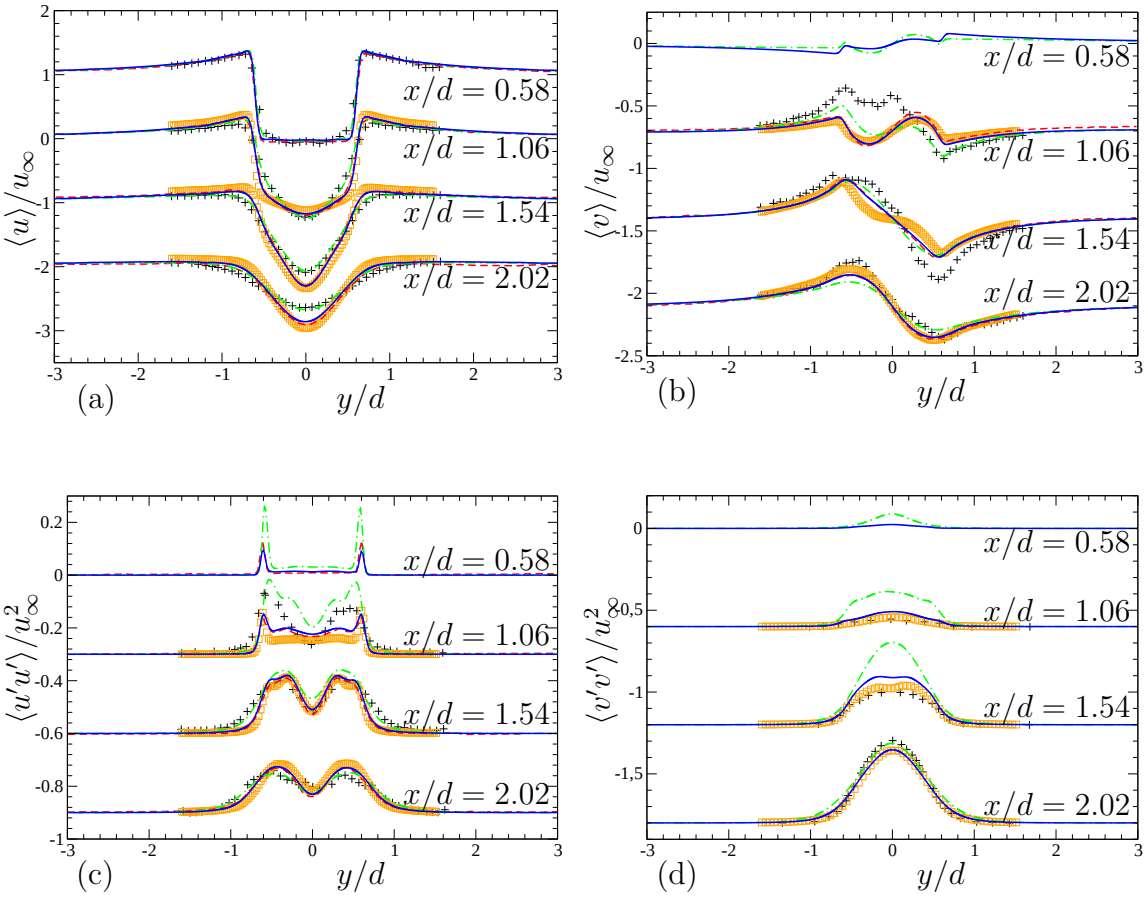

FIGURE 3.19: (a) Mean streamwise velocity, (b) mean crossflow velocity, (c) streamwise velocity fluctuations and (d) crossflow velocity fluctuations at different locations in the near wake of a circular cylinder at $Re = 3900$ (+: experimental data of Lourenco and Shih [89] ,□: experimental data of Parnaudeau [124] ,− −: Kravchenko and Moin [82], · − ·: ILES on a body-fitted grid, ——: ILES on a Cartesian grid + CIIM).

recovered for large y/d, as done also by Franke and Frank [44]. This anomalous behavior in the data of Lourenco and Shih [89] can be attributed to experimental disturbances (Parnaudeau et al. [124]). Despite the shifting, calculations in general agree better with the data of Parnaudeau et al. [124]. Possible explanations are discussed below.

In Fig. 3.19(c) the REYNOLDS normal stresses $\langle u'u' \rangle / U_\infty^2$ are shown. At $x/d = 0.58$ the calculation on the curvilinear grid shows higher peaks in the REYNOLDS normal stresses than the calculation on the Cartesian grid. The two sharp peaks at $x/d = 1.06$ can be attributed to the transitional state of the shear layers, which show a flapping behavior due to primary vortex formation. The two peaks can be matched in magnitude and position by the implicit LES on the Cartesian grid. The results on the curvilinear grid again show an overshoot with the respect to

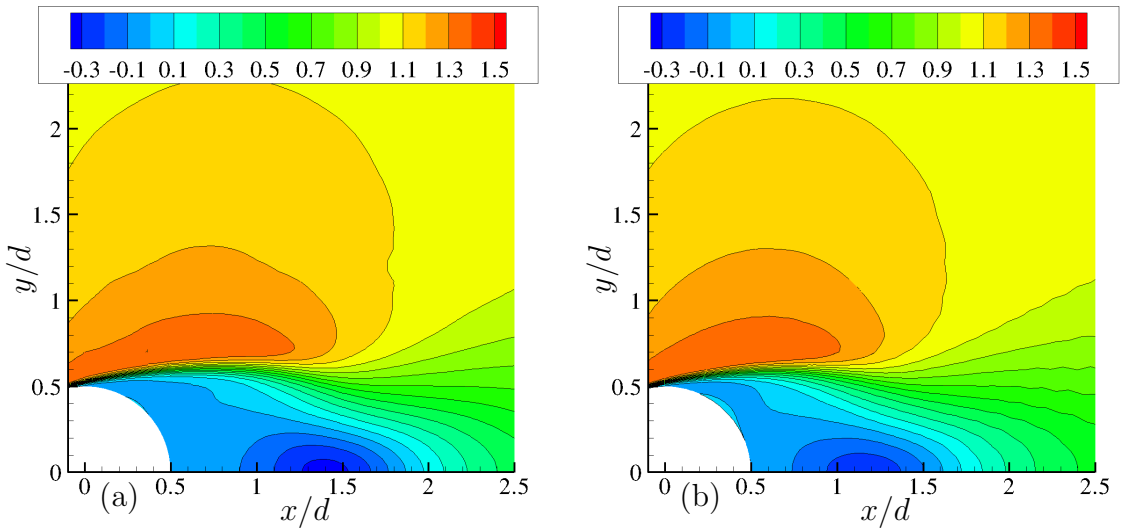

FIGURE 3.20: Contour maps of $\langle u \rangle / U_\infty$ for the circular cylinder flow at $Re = 3900$ on a Cartesian grid (left) and on a body-fitted grid (right).

other data. For all data better agreement is reached further downstream. For the crossflow normal REYNOLDS stresses $\langle v'v' \rangle / U_\infty^2$ the calculation on the Cartesian grid shows reasonable agreement with both experiments, see Fig. 3.19(d), while the calculation on the curvilinear grid shows an overshoot at $x/d = 0.58, 1.06, 1.54$. This overshoot implies that with respect to the Cartesian-grid calculation laminar-turbulent transition of the separated shear layers occurs closer to the cylinder, which leads to a shorter length of the recirculation bubble. This is also confirmed by the contour maps shown in Fig. 3.20-3.21. The mean velocity fields in Fig. 3.20 and Fig. 3.21 are similar apart from the size of the recirculation bubble, whereas the velocity fluctuations in Fig. 3.22-3.24 clearly show the earlier transition in the detached shear layers of the calculation on the body-fitted grid.

Figs. 3.26 compare the statistics in the near wake ($x/d = 4, 6, 7, 10$) with the experiments of Ong and Wallace [118]. Fig. 3.26(a) shows the mean streamwise velocity at four different locations. The slightly lower velocity at $x/d = 4$ and $x/d = 6$ on the wake centerline indicates that the recirculation length in the experiment is longer than the computed ones. Accordingly, the calculated streamwise REYNOLDS stress is slightly larger than the experimental REYNOLDS stress (see Fig. 3.26(b)). However, this finding confirms the numerical studies of Ma et al. [91], Franke and Frank [44] and Kravchenko and Moin [82]. Further downstream the agreement of the mean streamwise velocities and the streamwise REYNOLDS stresses is good for the Cartesian-grid calculation and satisfactory for the curvilinear-grid calculation. For the cross-flow normal stress and the

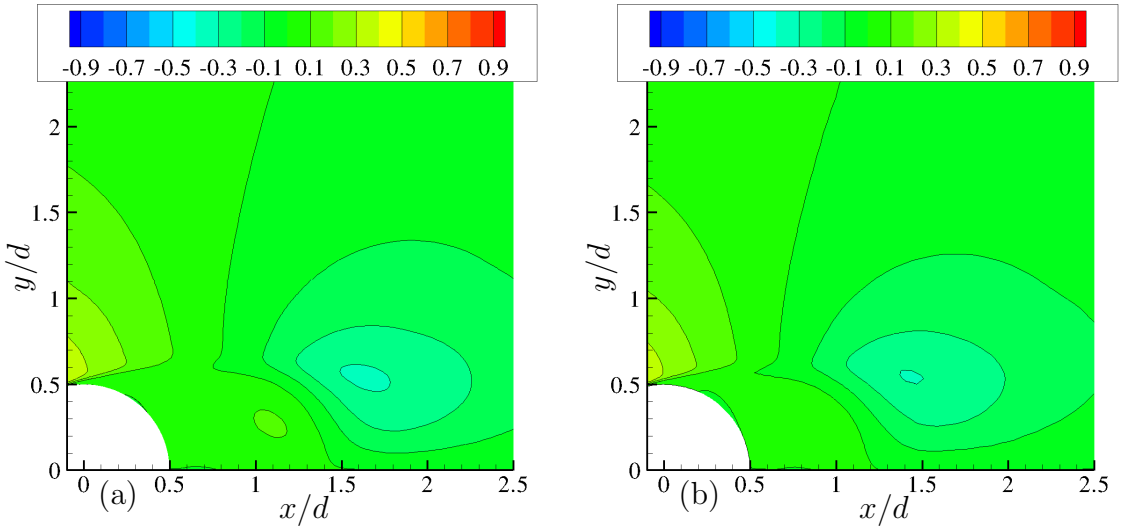

FIGURE 3.21: Contour maps of the $\langle v \rangle / U_\infty$ for the circular cylinder flow at $Re = 3900$ on a Cartesian grid (left) and on a body-fitted grid (right).

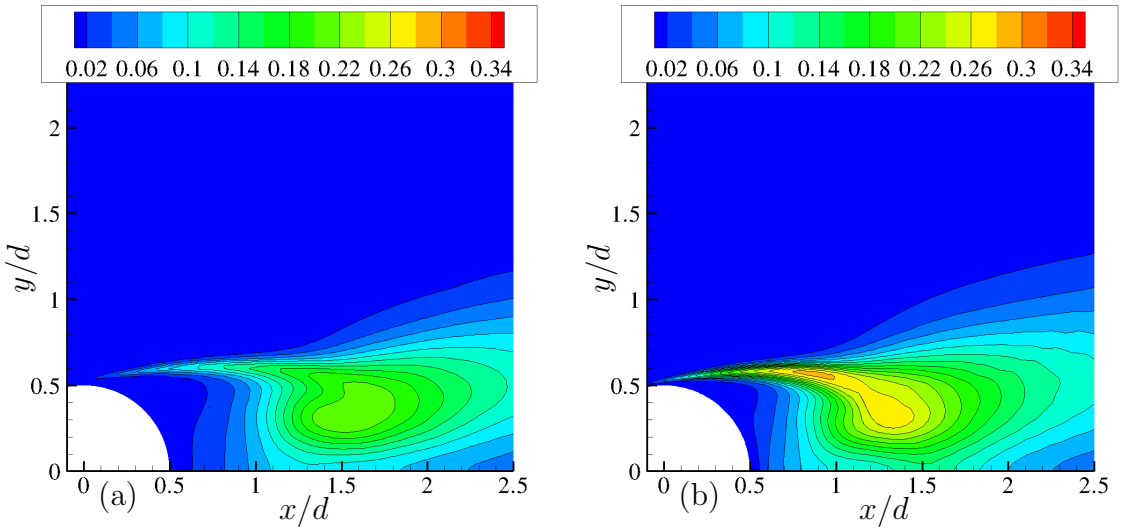

FIGURE 3.22: Contour maps of $\langle u'u' \rangle / U_\infty$for the circular cylinder flow at $Re = 3900$ on a Cartesian grid (left) and on a body-fitted grid (right).

REYNOLDS shear stress, plotted in Fig. 3.26(c) and Fig. 3.26(d), there is also a slight overprediction at $x/d = 4$. Further downstream the cross-flow stresses show that the calculated wake is wider than the measured one.

One Dimensional Energy Spectra In Fig. 3.27 the one dimensional energy spectrum of the u-velocity component on the centerline of the wake at $x/d = 3$ is plotted. The LOMB-periodogram technique with an oversampling of 4 and a HANN window were used to perform the spectral analysis of unevenly sampled u-velocity data for the two LES simulations. About 330,000 samples of the u-velocity were

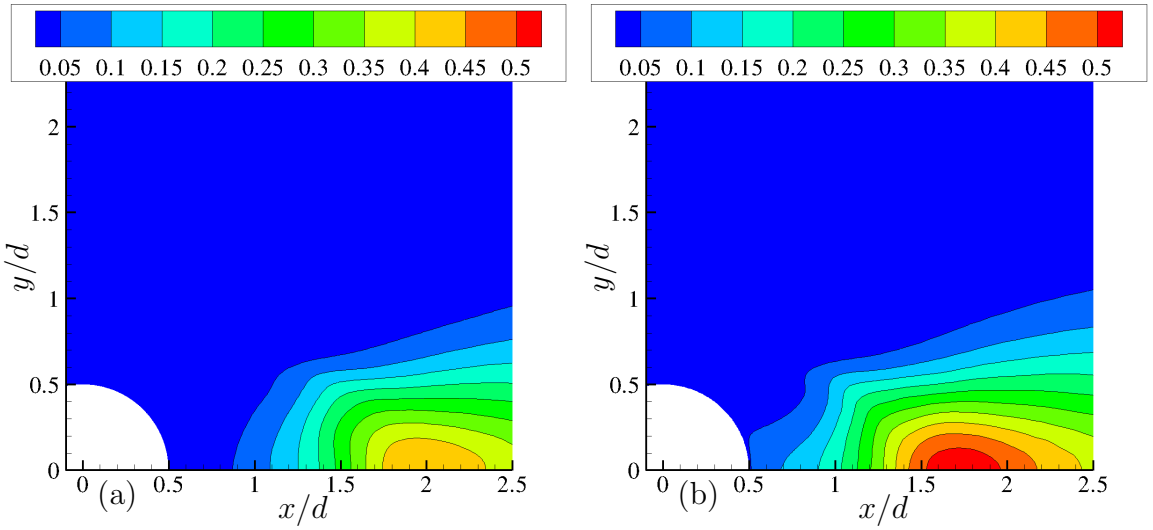

FIGURE 3.23: Contour maps of $\langle v'v' \rangle / U_\infty$ for the circular cylinder flow at $Re = 3900$ on a Cartesian grid (left) and on a body-fitted grid (right).

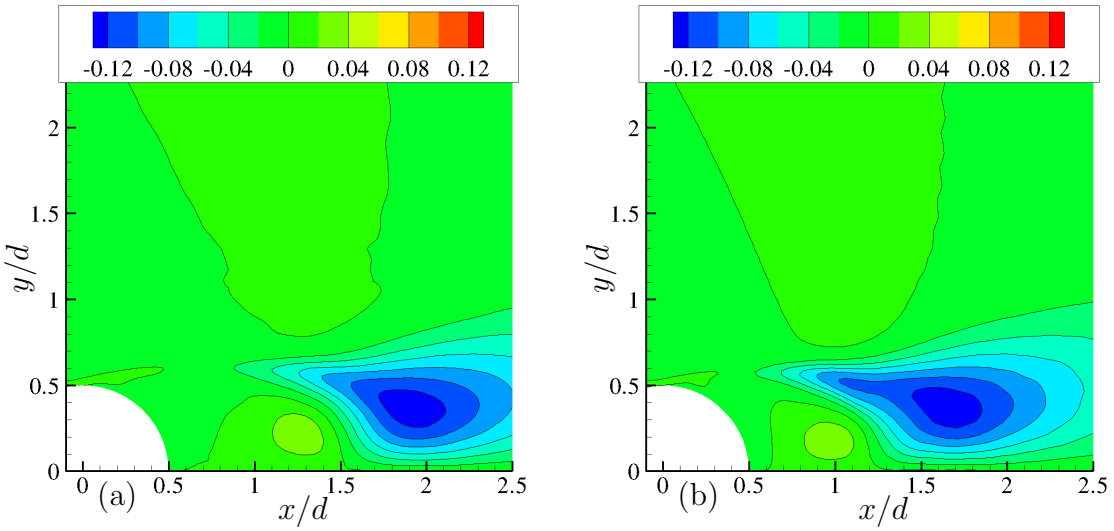

FIGURE 3.24: Contour maps of $\langle u'v' \rangle / U_\infty$ for the circular cylinder flow at $Re = 3900$ on a Cartesian grid (left) and on a body-fitted grid (right).

collected over a time interval of $TU_\infty/d = 300$. The frequencies are normalized with the STROUHAL shedding frequency ω_{St}. In Fig. 3.27 the one dimensional energy spectrum of the u-velocity component on the centerline of the wake at $x/d = 3$ is plotted. The LOMB-periodogram technique with an oversampling of 4 and a HANN window were used to perform the spectral analysis of unevenly sampled u-velocity data for the two LES simulations. About 330,000 samples of the u-velocity were collected over a time interval of $TU_\infty/d = 300$. The frequencies are normalized with the STROUHAL shedding frequency ω_{St}.

Also displayed in Fig. 3.27 are the experimental results of Parnaudeau et al. [124]

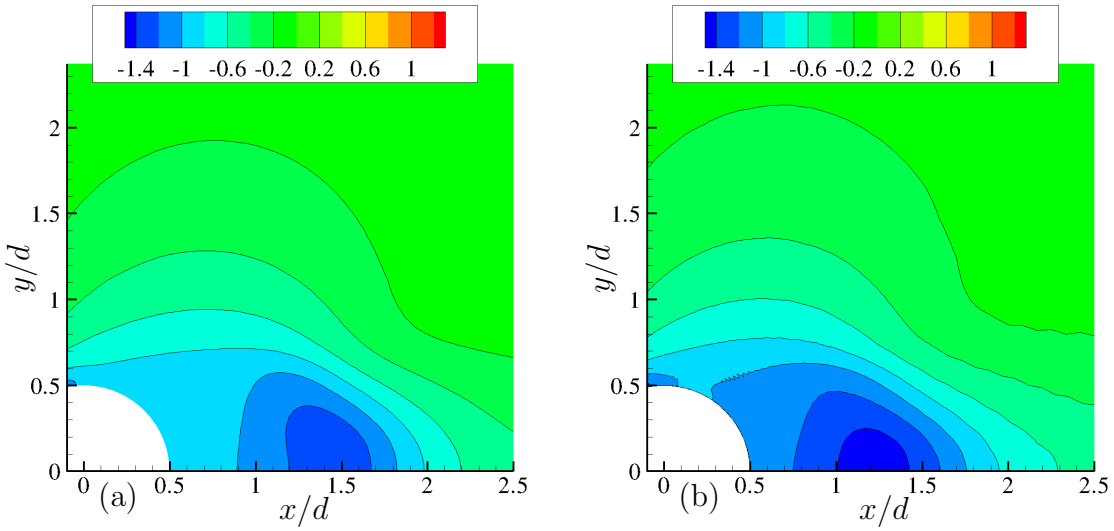

FIGURE 3.25: Contour maps of $\langle C_p \rangle / U_\infty$ for the circular cylinder flow at $Re = 3900$ on a Cartesian grid (left) and on a body-fitted grid (right).

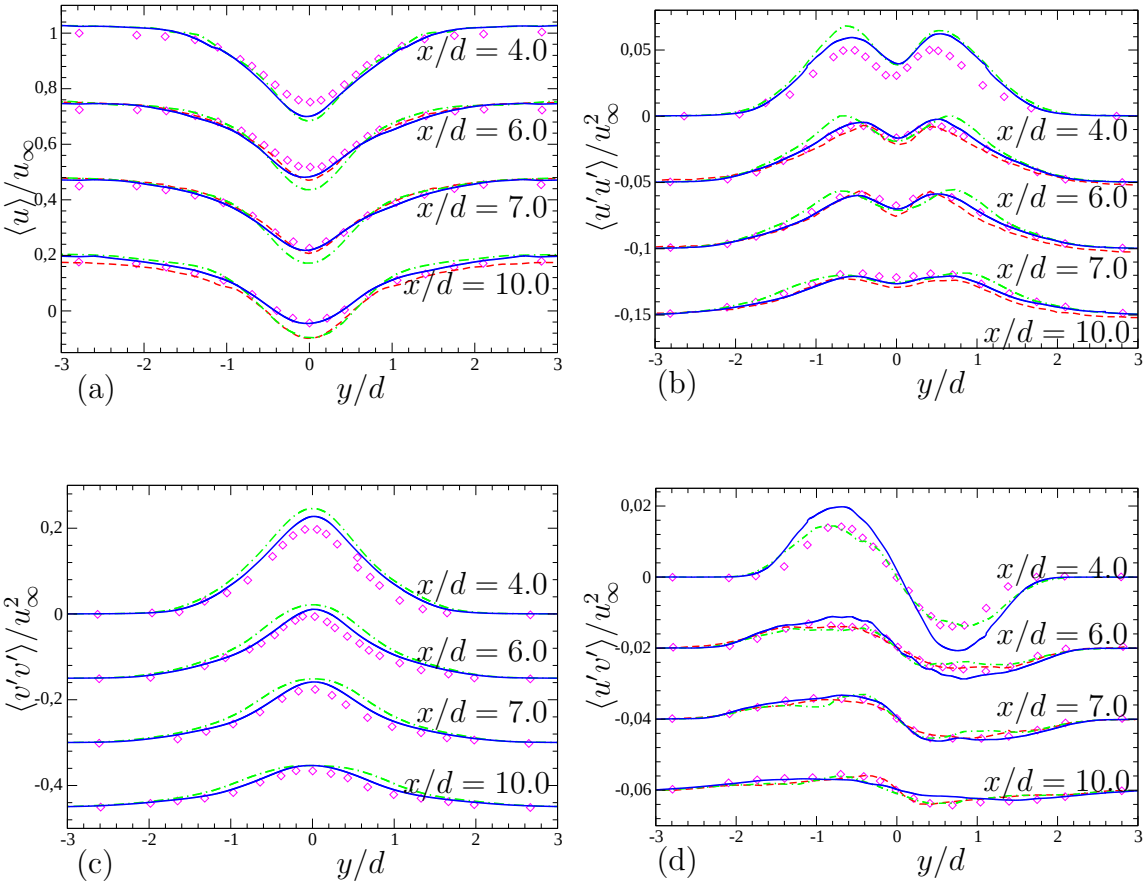

FIGURE 3.26: (a) Mean streamwise velocity, (b) mean crossflow velocity, (c) streamwise velocity fluctuations and (d) crossflow velocity fluctuations at different locations in the far wake of a circular cylinder at $Re = 3900$ ($\diamond$: experimental data of Ong and Wallace [118] ,– –: Kravchenko and Moin [82], $\cdot - \cdot$: ILES on a body-fitted grid, ——: ILES on a Cartesian grid + CIIM).

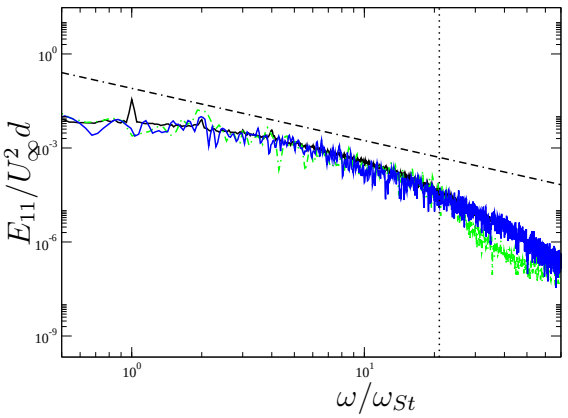

FIGURE 3.27: One dimensional velocity spectra at $x/d = 3$ in the wake of a circular cylinder at $Re = 3900$ ($\cdot - \cdot$ line: -5/3 slope, $\cdots\cdots$ line: cut-off frequency, ——— with $\omega/\omega_{St} < 35$: experimental data of Parnaudeau [124] ,– –: Kravchenko and Moin [82], $\cdot - \cdot$: ILES on a body-fitted grid, ———: ILES on a Cartesian grid + CIIM).

and a $-5/3$-slope. The spectra of the two LES and the experiment clearly show the inertial range. The good agreement for high wavenumbers of the ILES on the Cartesian grid with the experiment implies a correct representation of the flow down to the smallest scales. The three peaks of the u-spectrum at $x/d = 3$ of the experiment are the shedding frequency and the first and second harmonic [124]. The peak at $\omega/\omega_{St} = 1$ is an experimental artefact that should not be present at the centerline [124]. The first harmonic can be reproduced by the simulation on the body-fitted grid and by the on the on the Cartesian grid, whereas the one on the body-fitted grid also reproduces the second harmonic correctly.

Global Quantities Table 3.7 compares the mean drag coefficient, base suction coefficient ($\langle C_{p,ba}\rangle = \langle C_p\rangle|_{\theta=180^\circ}$), mean separation angle, mean recirculation length and STROUHAL number for the vortex shedding of the two simulations with the data from literature.

All presented data for the drag coefficient are in good agreement. Ma et al. [91] reported the lowest drag coefficient with 0.96 and Fröhlich et al. [49] obtained the highest with 1.08. In the present simulation on the curvilinear grid a similar value is obtained as in the LES of Fröhlich et al. [49] who also used LESOCC2 but in combination with a dynamic SMAGORINSKY model. The drag coefficient obtained on the Cartesian grid is close to the value obtained in the LES of Kravchenko and Moin [82].

The base suction coefficient is strongly dependent on the drag coefficient, since drag is mainly due to pressure drag and the pressure varies the strongest at $\theta = 180°$ in all simulations and experiments. The results on the curvilinear grid are again close to the results obtained by Fröhlich et al. [49]. The results obtained on the Cartesian grid are close to the experimental data of Norberg (extracted from Ref. [82]), see also Fig. 3.18(a).

The separation angle in the experiment by Lourenco and Shih [89] is considerably smaller than the angles in the simulations. However the angles found in the simulations including the simulations presented here are all in good agreement. The difference in length of the recirculation bubble L_{rec}/d between the experiments and the simulations are significant. Fröhlich et al. [49] and Ma et al. [91] as well as the current calculation on the curvilinear grid have the shortest recirculation bubble, which is also in rather good agreement with the experimental results of Lourenco and Shih [89]. The largest recirculation length has been reported by Franke and Frank [44]. The results obtained on the Cartesian grid are close to the experimental results of Cardell [16], the results obtained in the DNS of Dong et al. [34] and the results obtained in the LES of Kravchenko and Moin [82].

The results for the STROUHAL number in the simulations are all within the range of the experimental data, only Ma et al. [91] and Dong et al. [34] reported results that are lower. The results of both current simulations match the experimental results of Cardell [16] and Lourenco and Shih [89].

Discussion of Differences Differences between the two calculations in the present study certainly can be attributed to the effect of CIIM in the Cartesian grid calculation, differences in local grid resolution, and differences in the pressure treatment (staggered grid vs. collocated grid and stabilization). Fröhlich et al. [44] also used LESOCC2 in their LES on a curvilinear grid with a dynamic SMAGORINSKY model and obtained for the very near wake mean velocity profiles, the REYNOLDS stresses and the respective length of the recirculation bubble (see also Table 3.7) very similar results to our LESOCC2 calculation with ALDM. It is emphasized that, despite these differences, results of both implicit LES are well within the range of available experimental and numerical reference data. Overall, the results of the Cartesian-grid calculation with CIIM can be considered at least as reliable as that on the curvilinear grid.

TABLE 3.7: Drag coefficient, base suction coefficient, separation angle, recirculation bubble length and STROUHAL number for the circular cylinder flow at $Re = 3900$.

Study	$\langle C_D \rangle$	$\langle C_{p,ba} \rangle$	$\langle \theta_{sep} \rangle$	$\langle L_{rec}/d \rangle$	St
Cardell [16], experiment	-	-	-	1.33	0.215
Norberg taken from [82], experiment	0.98	-0.9	-	-	0.21
Lourenco and Shih [89], experiment	0.99	-	86°	1.19	0.215
Ong and Wallace [118], experiment	-	-	-	-	0.21
Parnaudeau et al. [124], experiment	-	-	-	1.51	0.208
Dong et al. [34], simulation	-	-	-	1.47	0.203
Dröge [35], simulation	1.01	-0.88	87.7°	1.26	0.210
Franke and Frank [44], simulation	0.98	-0.85	88.2°	1.64	0.209
Fröhlich et al. [49], simulation	1.08	-1.03	88.1°	1.09	0.216
Kravchenko and Moin [82], simulation	1.04	-0.94	88°	1.35	0.210
ILES on body-fitted grid	1.07	-1.05	88.9°	1.18	0.215
ILES on Cartesian grid + CIIM	1.05	-0.92	88°	1.38	0.210

Computational Performance In this test case, the computational cost for CIIM and the flux calculation with ALDM, each amounts to 2% of the overall computational time, while the POISSON solver needs about 80%. Compared to the ILES on the curvilinear grid the simulation on the Cartesian grid with CIIM is four times faster with respect to the wall-clock time per timestep and per mesh-node. Please note that both simulations have been conducted on the same system architecture, a SGI-ALTIX with ItaniumII processors. Further information on performance is given in [102].

Further information on this test case with more physical interpretation can be found in Meyer et al [101].

3.6 Turbulent Periodic Hill Flow at $Re = 10,595$

The incompressible turbulent flow in a channel with a periodic arrangement of smooth constrictions is calculated at $Re = 10,595$ based on the constriction height h and bulk velocity u_b above the constriction. The major challenges of this test case is to predict the turbulent flow separation from a curved geometry and the reattachment on a flat plate, see Fig. 3.28.

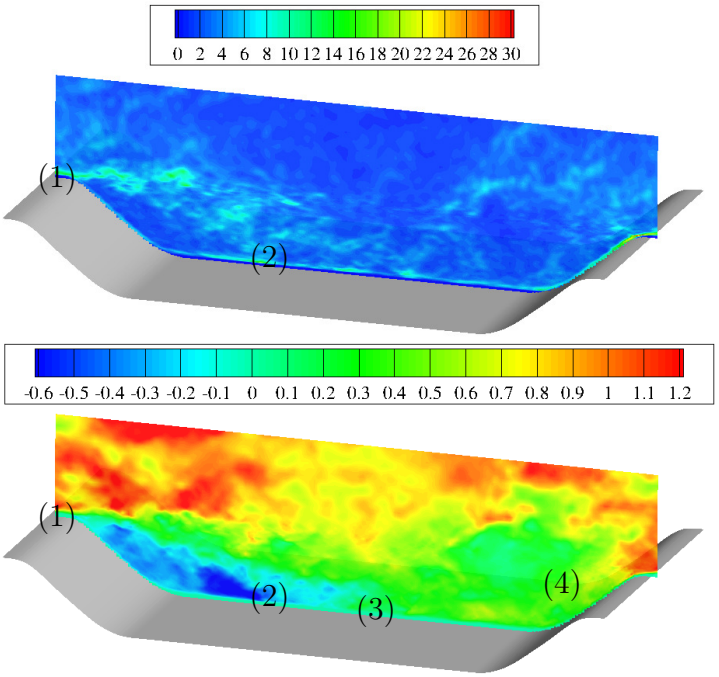

FIGURE 3.28: Slice in midplane in spanwise direction of instantaneous shear (top) and instantaneous streamwise velocity (bottom) for the flow over periodic hills at $Re = 10,595$ ((1): separation from smooth curved surface, (2): unsteady reattachment on flat plate, (3): acceleration in post-reattachment region, (4): acceleration on windward hill).

Previous Studies Motivated by these challenges many numerical and experimental studies have been conducted on different periodic hill set-ups. The present study uses the specific setup proposed by Mellen et al. [98] which is a modification to the experiment of Ahmeida et al. [2]. With respect to Ahmeida et al. [2] Mellen et al. [98] double the streamwise distance between the hills allowing for natural reattachment, halve the channel height for reduction of the computational effort, assume periodicity in spanwise direction instead of sidewalls in the experiment and reduce the REYNOLDS number.

In this configuration the periodic hills have been widely used in workshops like ERCOFTAC/IAHR/COST Workshops on Refined Turbulence Modeling [70] and [93] to study and compare the ability of different numerical methods. Thanks also to additional investigations many results of RANS [70, 93], LES [70, 93, 98, 160, 161] and hybrid LES-RANS approaches including Detached-Eddy Simulations DES [10, 11, 70, 141] are available.

The REYNOLDS number influence has been studied by Refs. [11, 13]. It was shown that gross-flow parameters, such as the separation bubble length, are sensitive to

grid quality [160] and modeling approximations (e.g. SGS modeling [98, 161] or wall modeling [160]).

To capture the flow physics computational grids require sufficient resolution in streamwise direction near the separation bubble [161] and in spanwise direction in the post-reattachment region [48]. As stated by Fröhlich et al. [48] most of the statistical RANS turbulence models fail even with second-moment closures to capture the "splatting of large-scale eddies originating form the shear layer and convected downstream towards the windward slope" [48] because they do not account for the high level of spanwise velocity fluctuations in the post-reattachment region. DES approaches perform better provided that the LES-RANS interface lies inside of the boundary layer on the crest of the hill [141]. In LES recovering near-wall physics has proven to be more influential then SGS-modeling making this configuration particularly suitable for testing CIIM.

For a qualitative comparison the well-resolved LES of Breuer [9] and the experiment of [13] are used.

Computational Details ALDM is employed as subgrid-scale model. The dimensions of the computational domain and the boundary conditions are shown in Fig. 3.29. The size of the computational domain corresponds to the one used in Ref [48]. A fixed Reynolds-number and a constant mass flux is ensured by a volume force term in the Navier-Stokes equations. A total number of 1.6 million cells is used: $192 \times 128 \times 64$ (streamwise $\times$ wall-normal $\times$ spanwise). The grid is stretched in streamwise and wall-normal direction to resolve the crest with $\Delta x_{crest}/h = 0.0375$ and $\Delta y_{crest}/h = 0.0051$ comparable to Ref. [13]. Top and bottom wall are resolved with $\Delta y/h = 0.008$ in wall normal direction. In spanwise direction the grid is equidistant with $\Delta z/h = 0.0703$.

Instantaneous Flow Field At the considered Reynolds-number the flow evolution is dominated by the detached shear layer above the unsteady recirculation zone. Fig. 3.28 gives an impression of the flow field of the present simulation. The flow separates downstream of the hill crest and reattaches in the middle of the hills. A good qualitative agreement is observed with Ref. [13, 48].

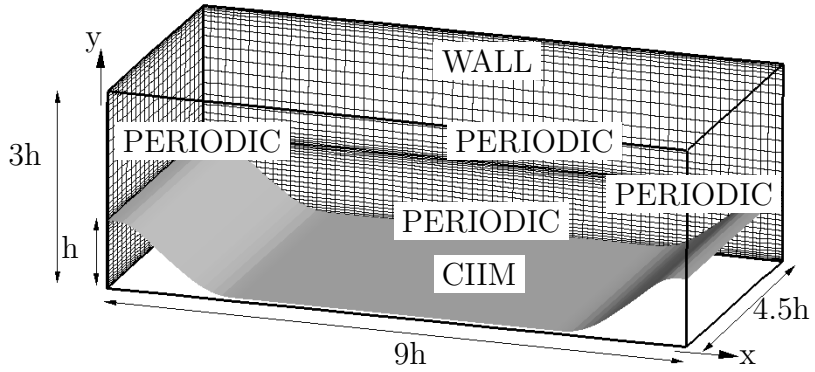

FIGURE 3.29: Computational setup for the flow over periodic hills at $Re = 10,595$ (every ninth computational cell is shown).

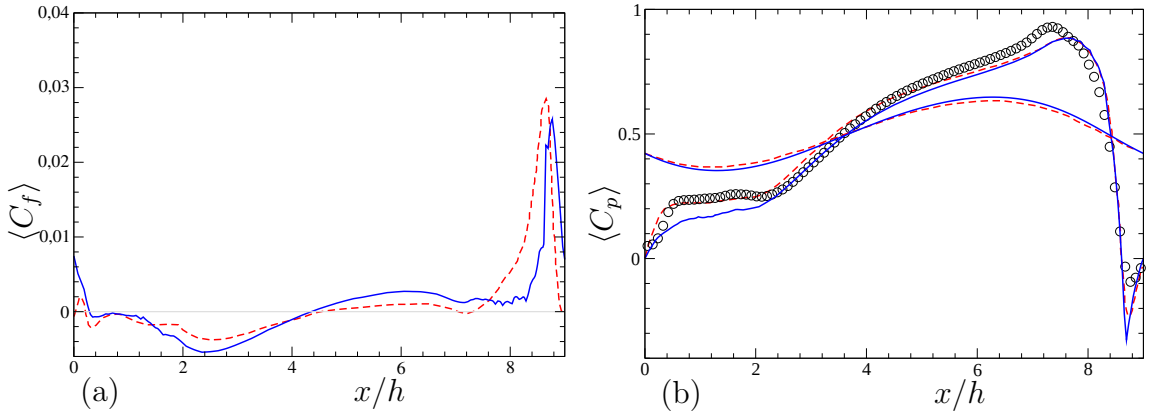

FIGURE 3.30: $\langle C_f \rangle$ and $\langle C_p \rangle$ distribution on the surface for the flow over periodic hills at $Re = 10,595$ (∘: experiment [134], −−: well-resolved LES on a grid with 13×10^6 cells [13], ——: present method).

Averaged Flow Field For a quantitative validation, turbulence statistics are sampled over 25 flow-through times and averaged in the homogeneous spanwise direction. The results are compared with the experimental data of Rapp [134] and the well-resolved LES of Breuer et al. [13]. Breuer et al. [13] used a dynamic SMAGORINSKY SGS model and a grid with 13 million cells.

Fig. 3.30 shows (a) the skin-friction coefficient $\langle C_f \rangle$ and (b) the pressure coefficient $\langle C_p \rangle$. The skin friction distribution along the bottom wall shows an irregular, geometry-induced variation of the near-wall velocity, as reported by [48]. At the leeward side of the hill the reverse flow in the recirculation region decelerates and almost reverses its direction. Over the upstream half of the recirculation zone on the lower wall $\langle C_p \rangle$ is nearly constant before rising dramatically downstream of the left crest. According to Ref [48] the pressure plateau in this area is typical for separated regions bordered by an outer flow with minor streamwise velocity variations. The minimum skin friction occurs at $x/h = 2.5 - 2.6$, where the

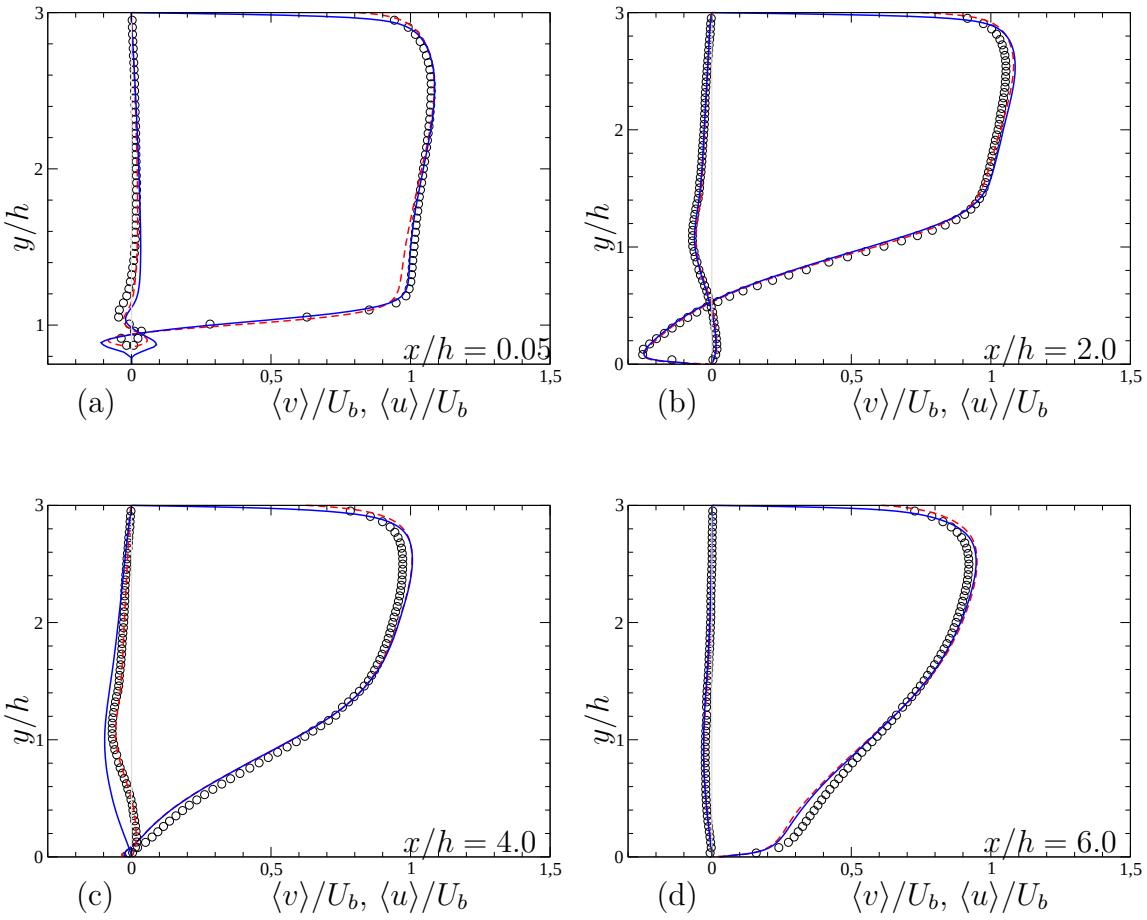

FIGURE 3.31: Mean streamwise and cross flow velocity for the flow over periodic hills at $Re = 10,595$ (○: experiment [134], −−: well-resolved LES on a grid with 13×10^6 cells [13], ——: present method).

reverse flow reaches a maximum. Approaching the reattachment point, the near wall velocity and the skin friction tend to zero. The positive pressure gradient is related to the deceleration of the outer flow and a laterally shrinking recirculation zone [48]. The incipient separation at $x/h = 7.2$ is not recovered by the present simulation. On the windward side of the hill the flow accelerates toward the hill crest leading to a sharp increase in skin friction.

The results for four stations are shown: a short distance beyond the hill crest at $x/h = 0.05$, in the middle of the recirculation region at $x/h = 2.0$, close to the reattachment at $x/h = 4.0$ and in the post-reattachment region, halfway between reattachment and the foot of the next hill at $x/h = 6.0$.

In Fig. 3.31 the mean streamwise and crossflow velocity are shown. Overall, a good agreement with the reference data [13, 134] is observed. Deviations are visible at $x/h = 4.0$ in the cross flow velocity. This might be linked to a shorter recirculation

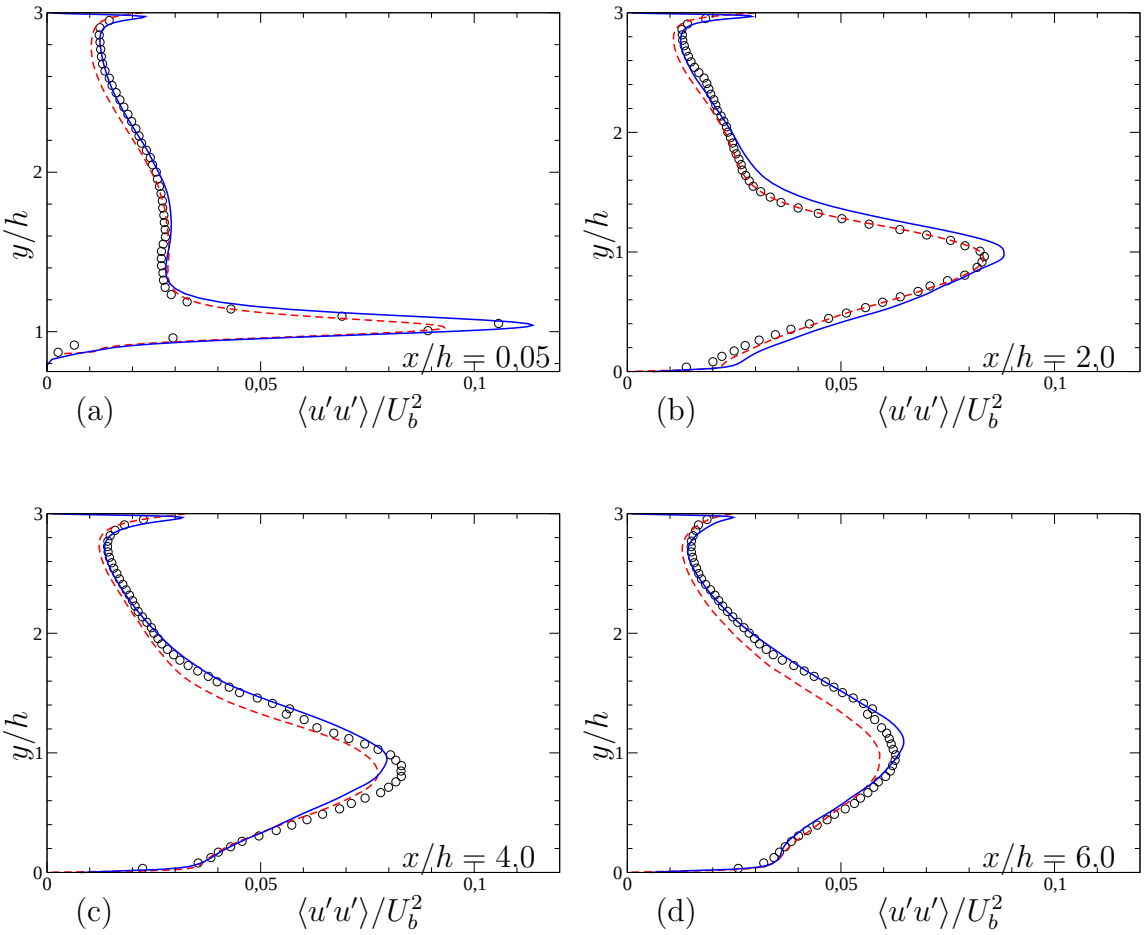

FIGURE 3.32: Streamwise velocity fluctuations for the flow over periodic hills at $Re = 10,595$ (○: experiment [134], −−: well-resolved LES on a grid with 13×10^6 cells [13], ——: present method).

bubble in the present simulation compared to the references. However, it should be noted that the crossflow velocity is about one order of magnitude smaller than the streamwise component and thus more sensitive [9].

Looking at the streamwise velocity fluctuations (Fig. 3.32) the simulated and the measured data are found to be in close agreement. The present simulation even reproduces the strong measured peak at $x/h = 0.05$.

The crossflow velocity fluctuations are depicted in Fig. 3.33. Considering the sensitiveness of the mean cross flow velocities the fluctuations show satisfactory agreement with the references.

In case of the REYNOLDS shear stresses (Fig. 3.33) the order of magnitude of the deviations is similar to the streamwise velocity fluctuations.

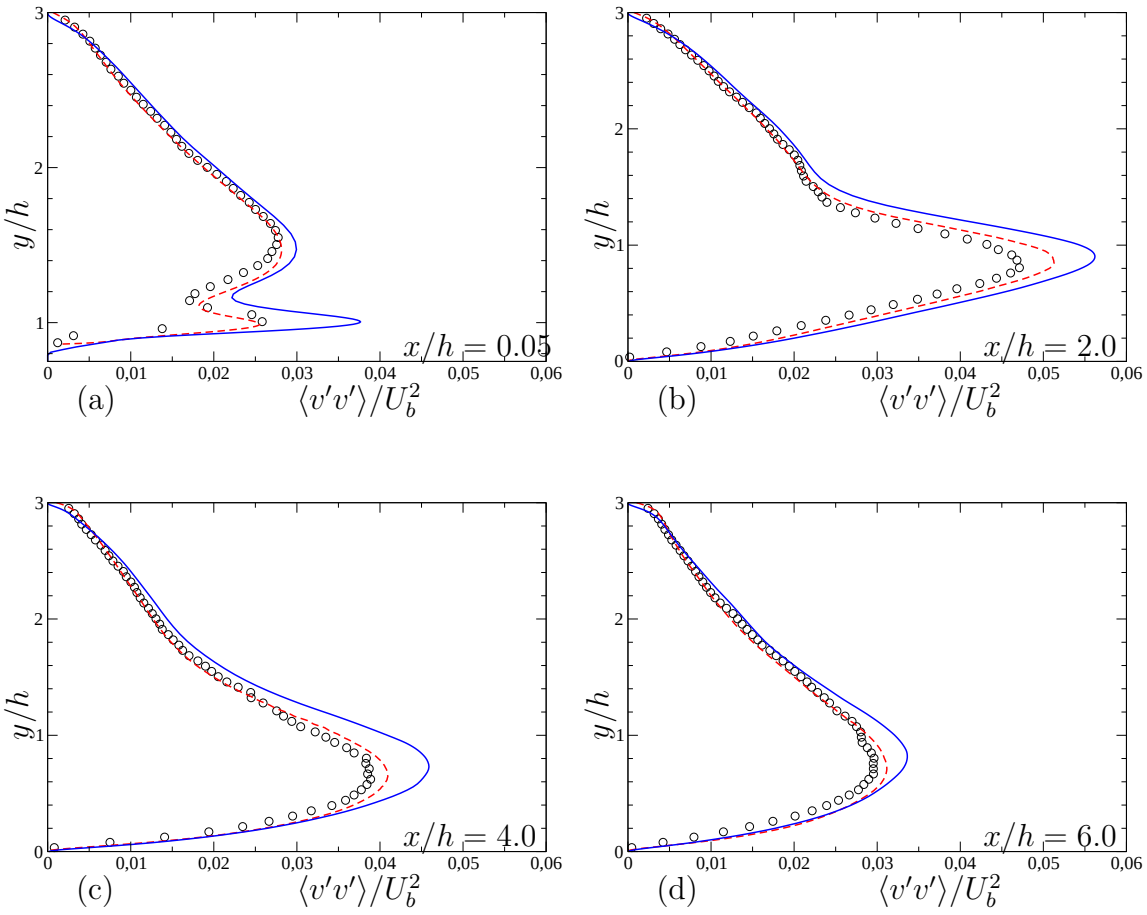

FIGURE 3.33: Cross flow velocity fluctuations for the flow over periodic hills at $Re = 10,595$ (○: experiment [134], ——: well-resolved LES on a grid with 13×10^6 cells [13], ———: present method).

TABLE 3.8: Separation and reattachment points for the flow over periodic hills at $Re = 10,595$.

Study	$(x/h)_{sep}$	$(x/h)_{reatt}$
Breuer [9], simulation	0.19	4.69
Hickel et al. [65], simulation	0.34	4.30
Fröhlich et al. [48], simulation	0.2	4.56
Simulation on Cartesian grid + CIIM	0.19	4.45

Global Quantities The flow separates at $(x/h)_{sep} = 0.19$ downstream of the hill crest and reattaches at $(x/h)_{reatt} = 4.5 - 4.65$, see also Fig. 3.35. The respective recirculation zone occupies about 50% of the streamwise domain. Good agreement with reference literature is found, see also Tab. 3.8.

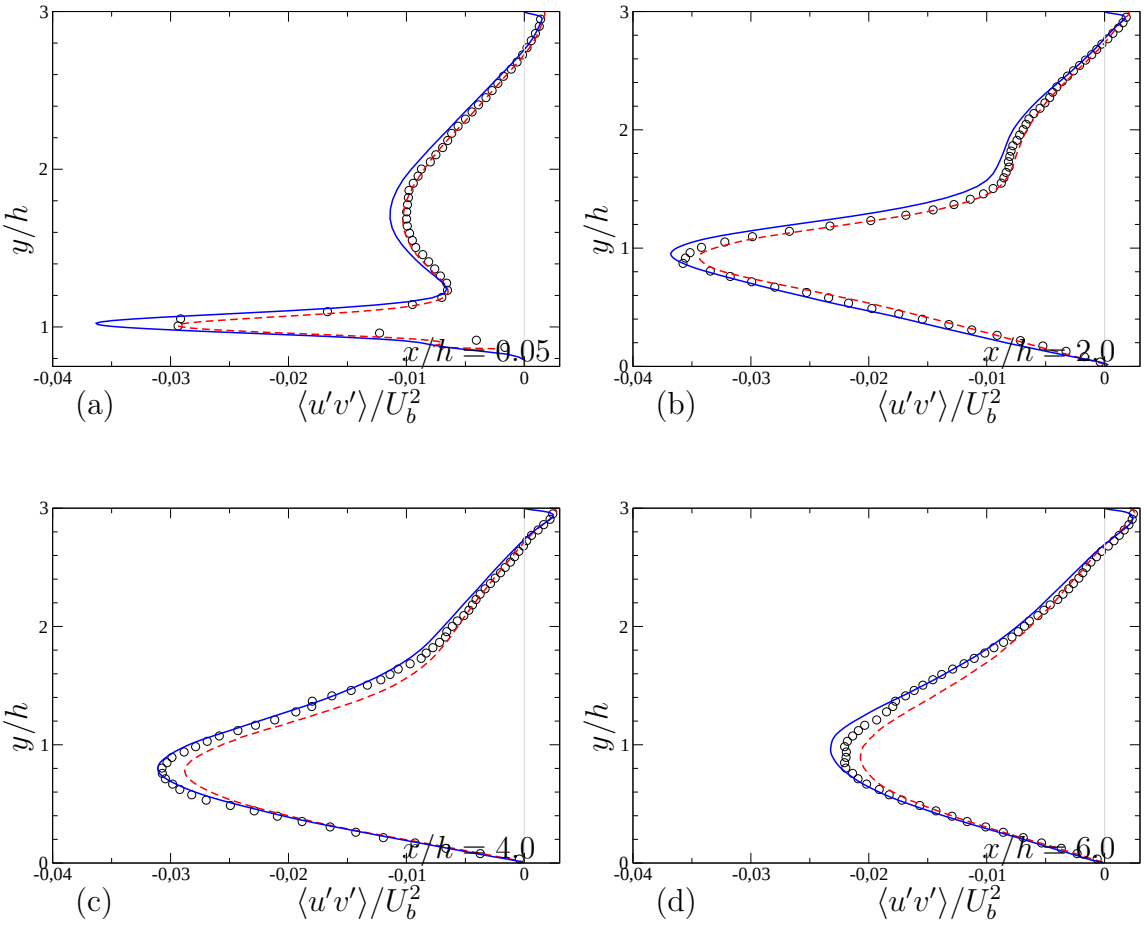

FIGURE 3.34: REYNOLDS shear-stresses for the flow over periodic hills at $Re = 10,595$ (○: experiment [134], −−: well-resolved LES on a grid with 13×10^6 cells [13], ——: present method).

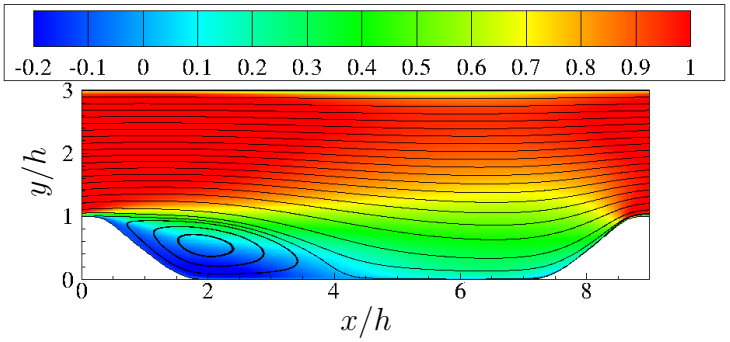

FIGURE 3.35: Contour map of the mean streamwise velocity for the flow over periodic hills at $Re = 10,595$.

Computational Performance For this test case again a SGI-ALTIX with ItaniumII processors have been used. CIIM consumes 3% of the overall computational time, the flux calculation with ALDM accounts for 8% and the POISSON solver uses 81%.

3.7 Summary

This chapter has validated and tested the performance of the Conservative Immersed Interface Method (CIIM) with respect to the previously defined requirements, see also Chapter 1.3. The test matrix is shown in Table 3.9.

TABLE 3.9: Summary of validation test cases and defined requirements.

Requirements/ Test case	convergence	conservation	interface physics	efficiency
Incl. channel flow Re=20	✓	✓	✓	-
Square Cylinder flow Re=100	✓	✓	-	-
Circ. Cylinder flow Re=40	-	✓	✓	-
Circ. Cylinder flow Re=100	✓	✓	-	-
Circ. Cylinder flow Re=3900	-	✓	✓	✓
Turbulent hill flow Re=10,595	-	✓	✓	✓

Second-order grid convergence has been proven for the decrease of the velocity profile error of the inclined channel flow at $Re = 20$ simulated on a equidistant grid and for the decrease of the lift and drag coefficient error of the circular and square cylinder flow at $Re = 100$ simulated on a stretched grid. For all simulations mass and momentum conservation are both locally and globally ensured. Mass conservation is proven to be ensured discretely according to the accuracy threshold chosen in the POISSON solver, up to machine precision if desired. The local flow physics at the interface are proven to be modeled correctly for the developed laminar channel flow at $Re = 20$, the separated laminar circular cylinder flow at $Re = 40$, the separated circular cylinder flow with laminar-turbulent transition at $Re = 3900$ and the separated and reattached turbulent periodic hill flow at $Re = 10,595$. Even for complex flow cases, i.e. circular cylinder at $Re = 3900$ and the turbulent periodic hill flow at $Re = 10,595$, CIIM consumes only an insignificant amount of computational time and allows for a four times faster simulation compared to a respective simulation on a curvilinear grid with standard

wall boundary conditions. All in all, CIIM fulfills all stated requirements and shows a good performance.

Chapter 4

Application to the Flow over a 3-element Highlift Airfoil

One major objective of this thesis is to show that CIIM is also suitable for the simulation of turbulent flows bounded by geometries of arbitrary shape and industrial relevance.

An industrially relevant test case is the turbulent flow over a 3-element highlift airfoil [173]. In aeronautics 3-element highlift airfoils or other highlift systems are employed to control the aerodynamic characteristics of aircraft [42, 136]: for steep climb-out and landing approaches or, more unconventionally, for improving the cruise flight performance [135]. The cruise flight performance can be improved by, e.g., novel seamless leading edge moveables to increase the portion of laminar flow on the wing during cruise, novel trailing edge devices for slatless leading edge wings or variable camber wings for better lift or even shock control.

An improvement of highlift systems can help to reduce fuel consumption and emissions, noise impact and to better exploit airport capacities [162, 181]. The necessary comprehensive understanding of the complex flow physics in the design and optimization process of such system, especially in the case of the unconventional or novel ones, can be achieved by high-fidelity numerical simulations. With increasing computational, capabilities numerical simulations can partially replace or complement time-consuming and expensive experimental investigations and therefore play an important role in the reduction of development cost and development time of new aircraft.

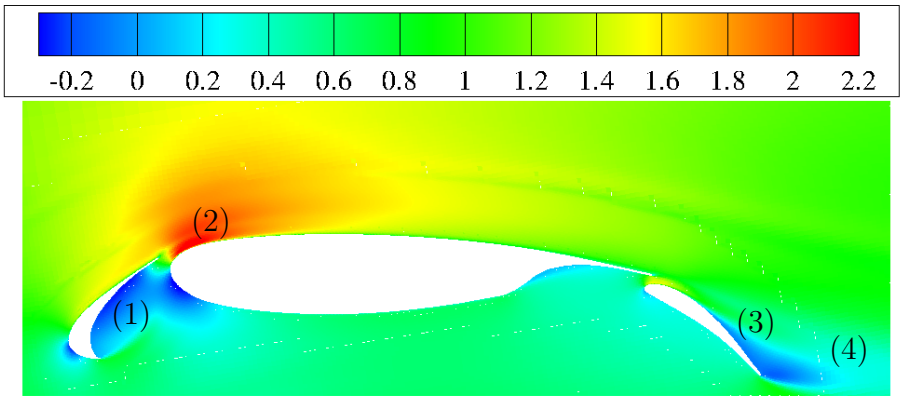

FIGURE 4.1: Contour map of the mean streamwise velocity for the flow over the RA16SC1 three-element airfoil at $Re = 1.7 \times 10^6$ ((1): unsteady flow dynamics, (2): laminar-turbulent transition region, (3): flow separation, (4): confluence of boundary layer and wake).

The flow over highlift configurations, such as shown in Fig. 4.1, exhibits a wide range of physical phenomena including highly unsteady flow dynamics in the cove of the slat (1), laminar-turbulent transition (2), strong pressure gradients possibly leading to flow separation on the flap (3), and the confluence of boundary layers and wakes (4).

Previous studies [31, 139] have shown that classical RANS simulations cannot fully reproduce the flow around a three-element airfoil due to the unsteady nature of the flow. Fully turbulent Unsteady RANS (URANS) simulations with turned-off turbulence modeling in the cove region of the slat made a better overall agreement possible [75, 76, 86]. However, in order to account for strong three-dimensional effects and a possible recirculation zone on the upper flap surface, researchers, e.g. Deck [31], considered LES but deemed it to be beyond feasibility. Instead Refs. [31, 138] use hybrid RANS/LES approaches or DES, and apply LES only in the slat cove and the flap region. However, according to Ref. [31] and to the knowledge of the author DES has not yet been able to accurately reproduce the flow physics on the flap. Since the flap contributes to the lift and respectively to the maximum possible lift coefficient[5], knowing and understanding the flow physics on the flap is crucial for the multi-element airfoil design [149] and an accurate prediction with numerical simulation is strongly desirable.

[5]In the design of conventional transport aircraft generally the maximum lift coefficient is the sizing parameter at landing, while at take-off rather the lift-to-drag ratio and the related required thrust and fuel burn for reaching a defined climb rate are important, see also Ref. [173]

As opposed to former studies this investigation accounts for the strong downstream influence of the slat [33, 107] on the turbulent-boundary layer development on the main wing [140] and on the flap by performing a LES of an entire highlift configuration. This is made feasible by several efficiency-increasing means such as modeling near-wall turbulence and the usage of adaptively refined computational grids. The study will answer the question to what extent an efficient LES approach can accurately reproduce the flow physics that was observed in a highlift configuration experiment.

4.1 Description of RA16SC-1 Experiments

The highlift airfoil of the current study has been designed and manufactured by ONERA Lille (France) for the EUROPIV 2 project G4RD-CT-2000-00190 and has used as a test case in the European DESider Project AST-CT-2003-502842. The airfoil model is based on the two-dimensional RA16SC-1 profile and consists of a slat, a wing and a flap in landing configuration, i.e., with the slat 30° and the flap 40° deflected. In this extended configuration the wing has a chord length $c_e = 0.691\ m$. The wing span is 2.1 m and maximum profile thickness measures 0.08 m.

The current investigation uses the experimental data of the EUROPIV 2 project, in which the DLR and Airbus Bremen (Germany) jointly performed static pressure and Particle Image Velocimetry (PIV) measurements in the Low Speed Wind Tunnel (LSWT) of Airbus Bremen [4, 113]. LSWT is an Eiffel-type wind tunnel with a closed test section with a cross section of $2.1 \times 2.1\ m^2$ and a test section length of 4.45 m.

The vertically installed model has been passed through the tunnel floor and has been attached a short distance underneath to a motorized turntable. The gap between wind tunnel floor and model has been filled by two wooden plates cut specially to fit around the model profile.

Optical access for the PIV system has been provided by several glass windows in the bottom, top and side walls of the test section. At the side walls outside the test section two pairs of Quantel Brilliant-B pulsed lasers plus associated optics have been mounted to form the light sheets. The light sheets have been set up to enter the test section horizontally at the height of the mid-span of the model. Seeding

has been produced by two DLR generators [81] filled with DEHS (Di-2-Ethylhexyl-Sebacat) oil and has been carried out in the complete hall surrounding of the wind tunnel. Data acquisition has been performed simultaneously by four cameras PCO SENSICAM digital cameras with Zeiss and Tamron lenses of maximum aperture fl 2.8 and various focal lengths.

PIV measurements have been performed in four camera setups (see Fig. 4.2) concentrating on the slat wake, the slat-wing gap, the flow mixing over the main wing, the wing-flap gap and the wing wake. Three angles of attack α have been investigated: 12°, 17.5° and 19°. Based on the retracted chord length of the wing $c_{retr} = c = 0.5\ m$, the wind tunnel freestream speed of $u_\infty = u_{ref} = 54\ m/s$ and atmospheric conditions the REYNOLDS number has been equal to 1.7×10^6.

During PIV measurements the tunnel hall has been blacked out. Before starting data acquisition fine adjustments to the focii of the cameras have been carried out on the seeding particles themselves. For each incidence a sequence of 34 images pairs has been acquired from each camera with an inter-pair interval of $1/3\ s$. This procedure has been then repeated twice to give 102 image pairs for each window allowing for averaging over approximately 100 image pairs per window. All data have also been averaged in spanwise direction.

In the post-processing process, perspective distortions have been removed by dewarping all images in the first step [37].

4.2 Computational Setup

4.2.1 Numerical Method

The flow is described by the incompressible NAVIER-STOKES equations discretized on a staggered Cartesian grid. The convective terms are discretized with ALDM [64]. As opposed to other studies, e.g. Refs. [21, 31, 76], the turbulence model is not modified or even switched off in the cove of the slat or other regions. The explicit third-order RUNGE-KUTTA scheme of Shu [142] is used for time advancement. The time-step is dynamically adapted to satisfy the COURANT-FRIEDRICHS-LEWY condition CFL = 1.0. Diffusive terms and the pressure-POISSON equation are discretized by second-order centered differences. The POISSON solver employs fast

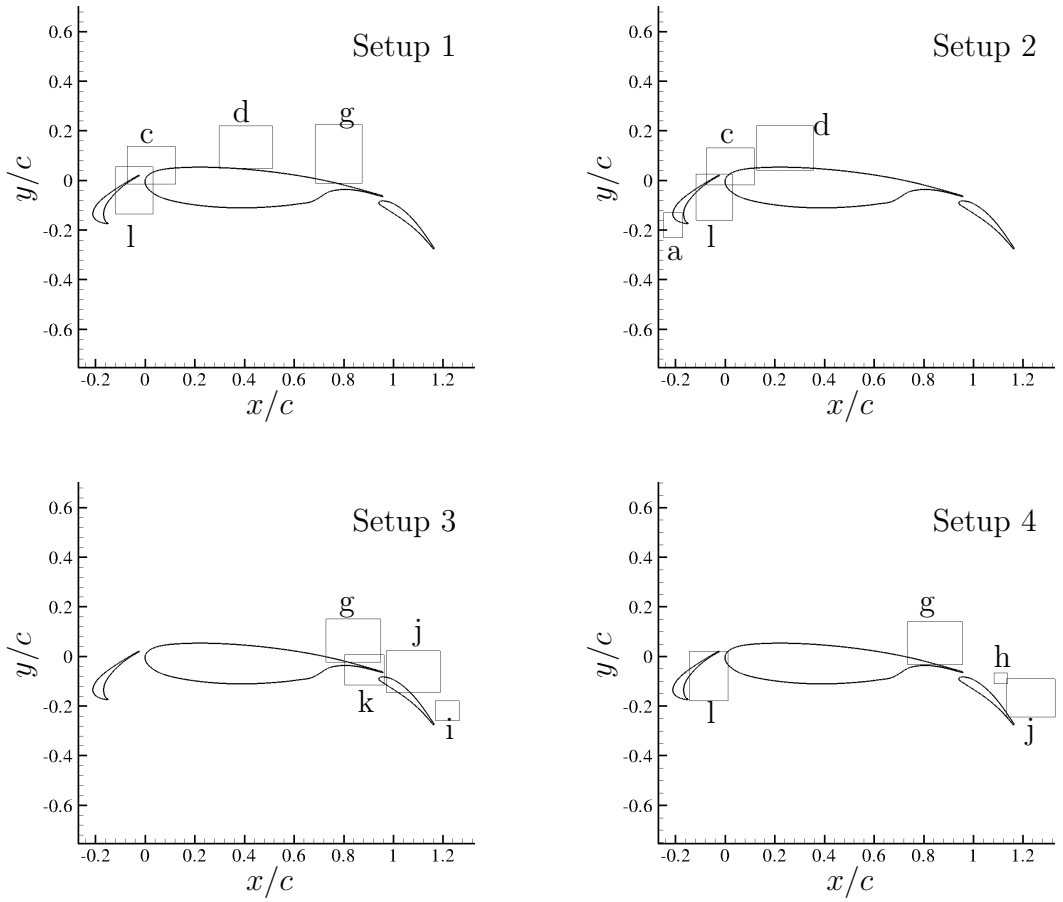

FIGURE 4.2: Four camera arrangements for PIV measurements for the flow over the RA16SC-1 three-element airfoil.

FOURIER transforms in the spanwise direction and the stabilized bi-conjugate gradient (BiCGstab) method [146, 174] in the streamwise and wall-normal directions. The POISSON equation is solved at every RUNGE-KUTTA substep.

4.2.2 Computational Domain and Boundary Conditions

The computational domain is shown in Fig. 4.3. The farfield is chosen to be at at least 30 c away from the profile. At the inlet a uniform velocity profile and at the outlet a pressure condition is defined. At the upper and lower side free-slip boundary conditions are imposed. In spanwise direction the domain extent is 0.2 c and periodicity is assumed. In all directions the domain extent is larger or at least as large as in comparable studies [21, 31, 75].

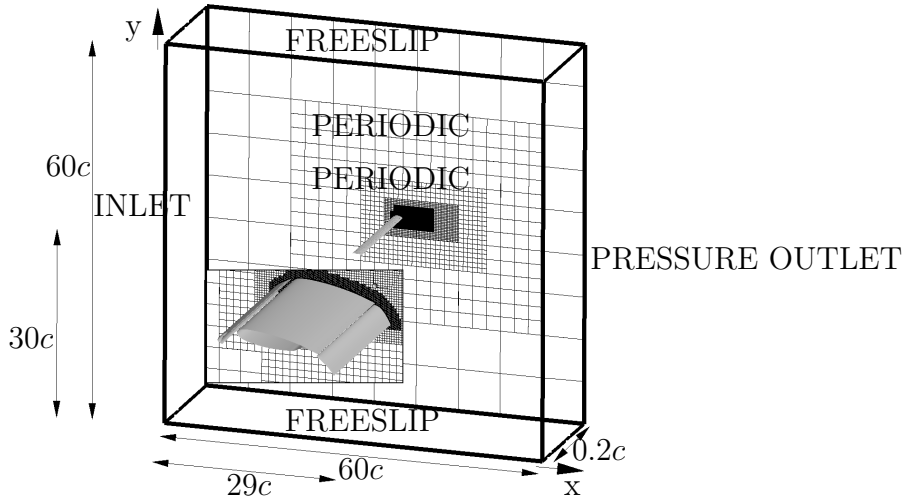

FIGURE 4.3: Computational setup for the flow over the RA16SC-1 three-element airfoil at $Re = 1.7 \times 10^6$ (every third computational cell is shown, spanwise extent is 100 times magnified for better visualization).

Wall boundary conditions are imposed with CIIM in connection with a Thin-Boundary-Layer-Equation (TBLE) based wall-model [19]. The coupling position between wall-model and LES is located in the logarithmic region of the boundary layer.

Please note that laminar-turbulent transition in this simulation is fully natural. Neither fully turbulent flow is assumed as in Deck [21, 31] nor turbulence is triggered by, e.g., suction/blowing approaches as in Refs. [22, 86].

4.2.3 Computational Grid

The computational domain is subdivided into 2000 blocks with 7 different grid refinement levels. In the vicinity of the immersed interface cell sizes correspond to a non dimensional value of $\Delta y^+ = 60$, based on the experiences made for turbulent boundary layers with a TBLE wall-model [19]. Refined regions are located in the slat cove, the wake of the flap and up to distance of 0.15 c away from the profile on the suction side of the slat, wing and flap (see Fig.4.4). The planar xy-grid consists of approximately $300,000$ square-shaped computational cells. The basic planar xy-grid is simply duplicated to obtain the spanwise grid that consists of 128 equidistantly distributed cells. Please note that as opposed to Deck [31] this is a fully three-dimensional simulation without any two-dimensional regions. In

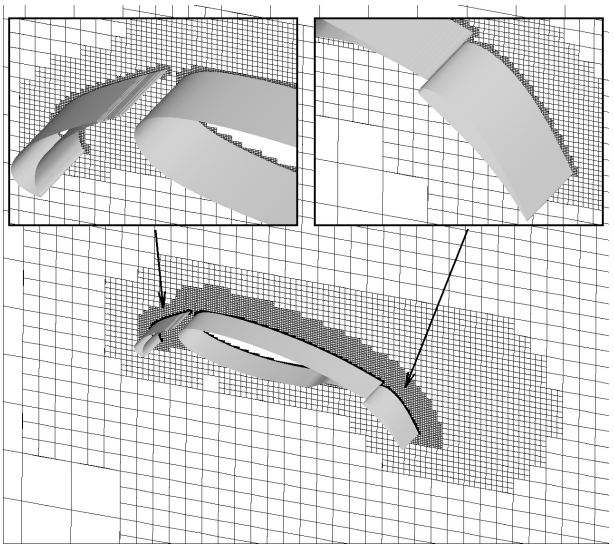

FIGURE 4.4: Computational grid for the flow over the RA16SC-1 three-element airfoil at $Re = 1.7 \times 10^6$ (every third computational cell is shown).

all directions the grid resolution is higher than in the previous study by Deck [31]. The total number of cells of this study is 38×10^6.

4.2.4 Statistical Analysis

For statistical analysis the simulation was run for $\Delta t_{ave} = 0.3\ s$ of physical time after reaching a statistically steady state. A clearer picture of the sample size for the flow over a wing is obtained with the Convective Time Unit (CTU), i.e., the time the flow needs to pass the wing, which is defined to be

$$CTU = \frac{c}{u_{ref}}. \tag{4.1}$$

The number of Convective Time Units n_{CTU} is calculated with

$$n_{CTU} = \frac{\Delta t_{ave}}{CTU}. \tag{4.2}$$

Respectively, the flow of this study has been averaged over 30 Convective Time Units (CTU's) after the transient was washed out and the flow has reached a statistically steady-state. Statistics have been also averaged in the homogeneous spanwise direction.

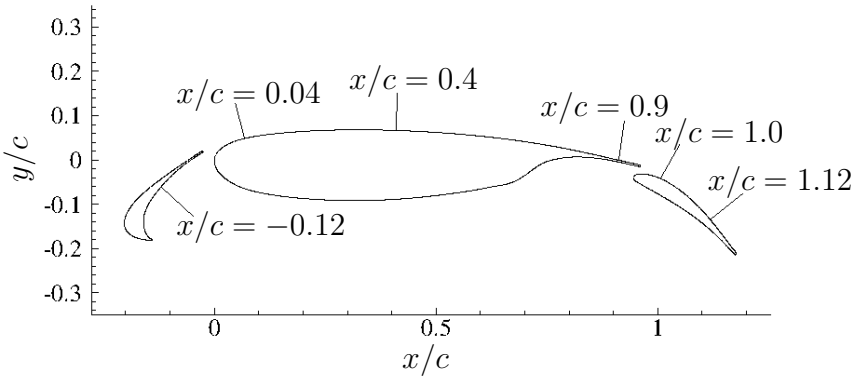

FIGURE 4.5: RA16SC-1 model and rake locations.

4.3 Results and Discussion

This investigation uses the conventions and variable definitions of Chapter 3.2. Further variables are defined in the respective section before their usage.

This investigation pertains to the experiment with the angle of attack $\alpha = 12°$. According to Refs. [31, 165] the presence of separation on the tunnel walls caused by the lack of suction devices affected the recirculation and respectively the loading on the slat. An adaptation of the angle of attack in the calculation is a commonly used methodology for highlift device computations, see also Ref. [75]. In a study related to this test case, Tran [165] showed, that, based on a comparison of the experimental and calculated slat lift coefficient, the correction for $\alpha = 12°$ is equal to $-4°$. However, Deck [31] showed, that, based on a comparison of the pressure coefficient distribution between the experiment and precursor RANS calculations, a correction of $-3°$ is sufficient for his DES. For the current simulation a correction of $-3°$, i.e., $\alpha = 9°$, is chosen.

The investigation is divided into: a) Global Surface Pressure Distribution, b) Flow over the Slat, c) Flow over the Main Wing and d) Flow over the Flap. Both, the instantaneous flow field and the averaged flow field are studied. For comparing the turbulent statistics of the current simulation with experimental data six rake positions are defined, see Fig. 4.5. The experimental profiles at the rake positions are extracted from the PIV maps shown in Fig. 4.2. The profiles are plotted against the local wall-normal distance normalized by the reference chord length, i.e. δ/c.

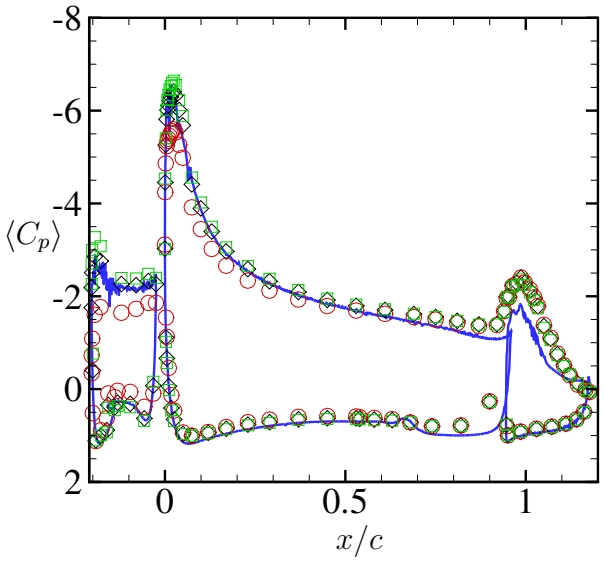

FIGURE 4.6: Pressure distribution $\langle C_p \rangle$ on the surface of the slat, main wing and flap for the RA16SC-1 three-element airfoil at $Re = 1.7 \times 10^6$ ($\circ$: experiment 8° angle of attack, $\diamond$: experiment 12° angle of attack, $\square$: experiment 13° angle of attack, ——: present simulation at 9° angle of attack).

4.3.1 Global Surface Pressure Distribution

Fig. 4.6 compares the distribution of the mean surface pressure coefficient $\langle C_p \rangle$ of the present simulation with the experimental results of the EUROPIV 2 project at $\alpha = 8°$, 12° and 13°. The good agreement with the experimental $\langle C_p \rangle$ distribution at $\alpha = 12°$ gives evidence that the correction to $\alpha = 9°$ for the simulation is adequate. From here on only the experiment at $\alpha = 12°$ and the simulation at $\alpha = 9°$ are considered.

On the slat surface the experimental pressure coefficient $\langle C_p \rangle$ distribution is well reproduced by the simulation. Please note the good agreement for the highest positive $\langle C_p \rangle$ at the stagnation point, the slightly lower $\langle C_p \rangle$ at the slat cusp and the $\langle C_p \rangle$ distribution of the pressure recovery region starting at the suction peak $\langle C_p \rangle_{min,slat}$ and ending at the slat trailing edge.

On the main wing surface the experimental $\langle C_p \rangle$ distribution is also predicted well by the simulation. Near the leading edge the good agreement between measured and computed $\langle C_p \rangle$ distribution gives proof that flow physics in the slat cove are represented correctly [21, 22]. A good agreement is also found on the lower main wing surface including the flap cove. The discrepancy near the trailing edge is also visible in all other related simulations [31, 165] and is likely to be due to

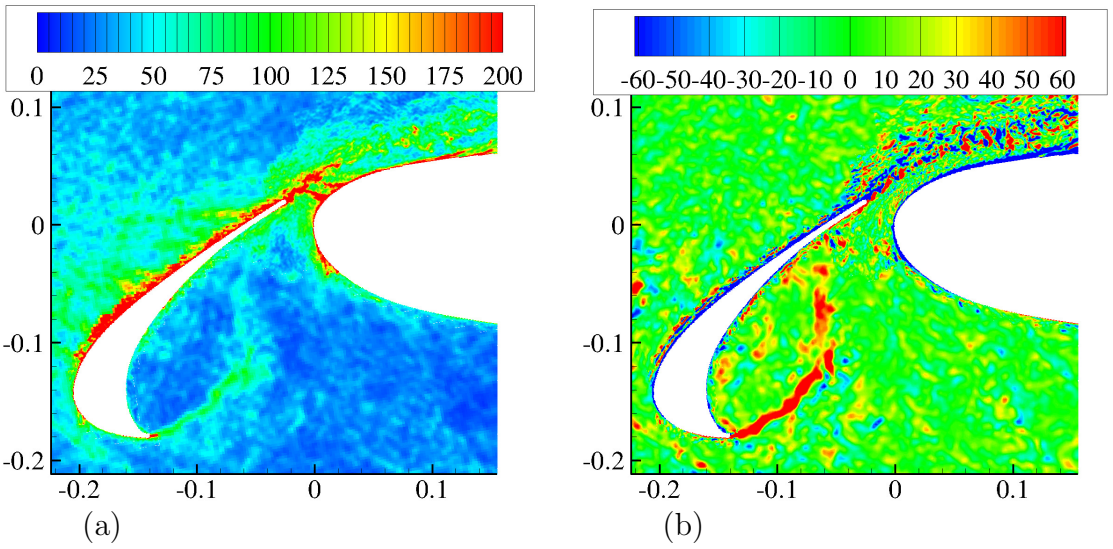

FIGURE 4.7: Contour maps of the shear and the spanwise vorticity $\omega_z c/u_\infty$ in the slat area of the RA16SC-1 three-element airfoil at $Re = 1.7 \times 10^6$.

experimental issues. On the first 70% of the upper wing surface, i.e. the suction side, the simulation and the experiment agree well; especially the experimental pressure peak $(\langle C_p \rangle)_{min,main}$ is predicted perfectly both in position and in magnitude. However, near the wing trailing edge the agreement on the upper wing is less satisfactory.

On the flap surface the $\langle C_p \rangle$ distribution of the experiment and the simulation agrees less than on the slat and on the main wing. This confirms previous observations of Deck [31].

Please note that the $\langle C_p \rangle$ distribution on the flap is almost independent of the angle of attack, see also Fig. 4.6 and similar findings in Ref. [21, 165]. Thus, it is concluded that the angle of attack and its correction are most likely not the cause of the discrepancy between experiment and simulation. This discrepancy will be investigated later on.

4.3.2 Flow over the Slat

As the flow physics at the slat have a strong downstream influence and respectively influence on the angle of attack limits, wing loading etc., they are studied first.

Instantaneous Flow Field Fig. 4.7(a) shows the shear layers emanating from the slat trailing edge and the slat cusp. Almost immediately downstream of the

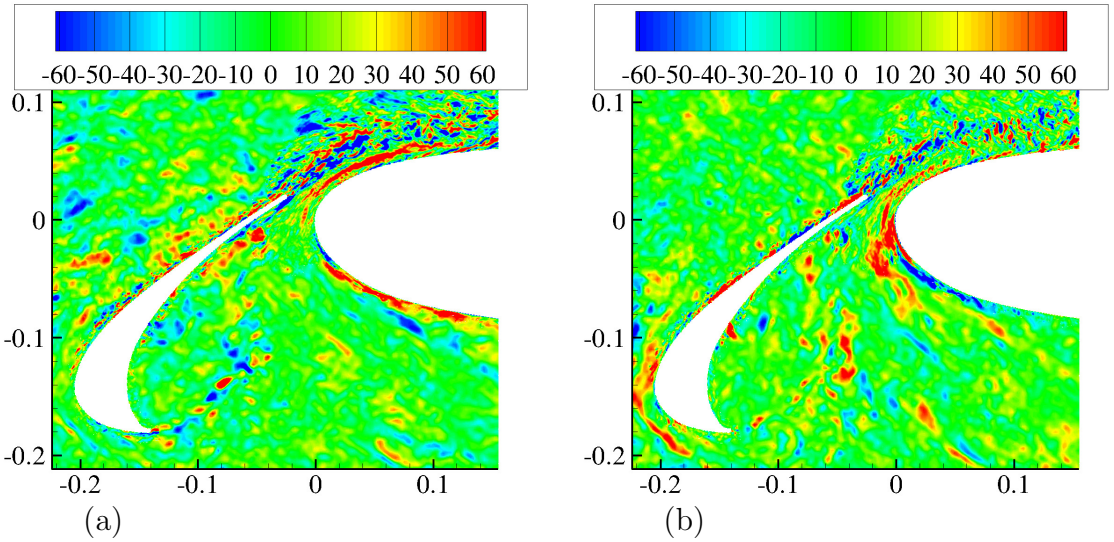

FIGURE 4.8: Contour maps of the streamwise $\omega_x d/u_\infty$ and the crossflow vorticity $\omega_y c/u_\infty$ in the slat area of the RA16SC-1 three-element airfoil at $Re = 1.7 \times 10^6$.

cusp the shear layer rolls up and evolves into a stream of discrete quasi-2D, elongated vortices co-rotating in spanwise direction with a positive sign, see Fig. 4.7(b). Convected towards the lower surface of the slat within the shear layer the vortices progressively become three-dimensional and distorted, see vorticity in streamwise and crossflow direction in Fig. 4.8(a) and (b) as well as the vorticity magnitude in Fig. 4.9. The shear layer reattaches and forms a recirculation region to which some vortices temporarily entrain while other vortices are drawn towards the slat trailing edge.

The entrained vortices are diverted downwards to the cusp and induce unsteady eruptions of secondary vortices from the recirculating boundary layer flow along the slat surface, see Fig. 4.7(b). When swept upwards again by the recirculating boundary layer flow the vortices partially merge with those convected by the shear layer separated from the slat cusp in a mixing layer.

The vortices directed towards the slat trailing edge get distorted by the local mean flow strain, see also Fig. 4.8 (a) and (b). Specifically, the stretching of streamwise vorticity, as a result of the mean flow acceleration behind the reattachment, leads to streamwise elongated vorticity structures convecting underneath the slat trailing edge, see also Fig. 4.10. The convected slat cove structures interact with the small-scale vortices shed behind the relatively thin slat trailing edge.

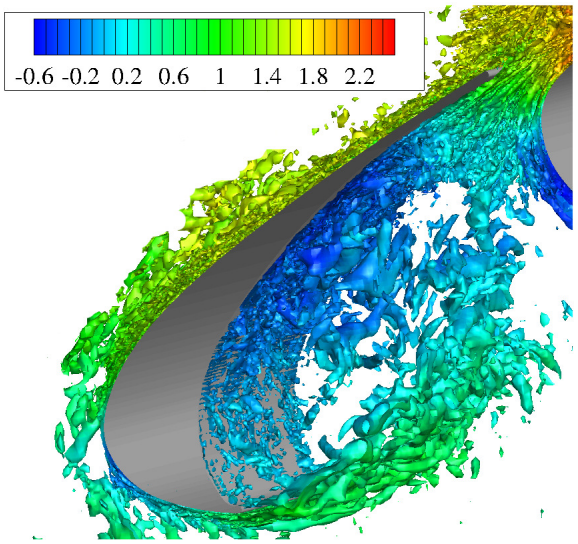

FIGURE 4.9: Instantaneous vorticity magnitude isosurface colored by streamwise-velocity in the slat area of the main wing of the RA16SC-1 three-element airfoil at $Re = 1.7 \times 10^6$.

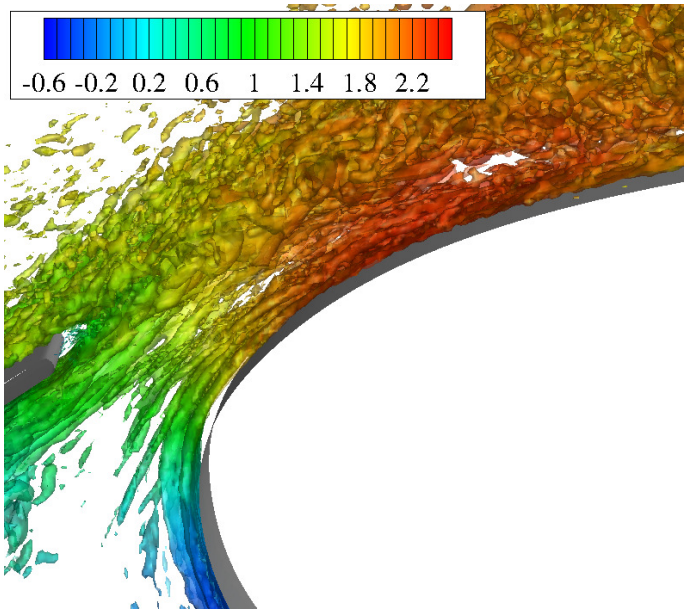

FIGURE 4.10: Instantaneous vorticity magnitude isosurface colored by streamwise-velocity in the gap between trailing edge of the slat and the main wing of the RA16SC-1 three-element airfoil at $Re = 1.7 \times 10^6$.

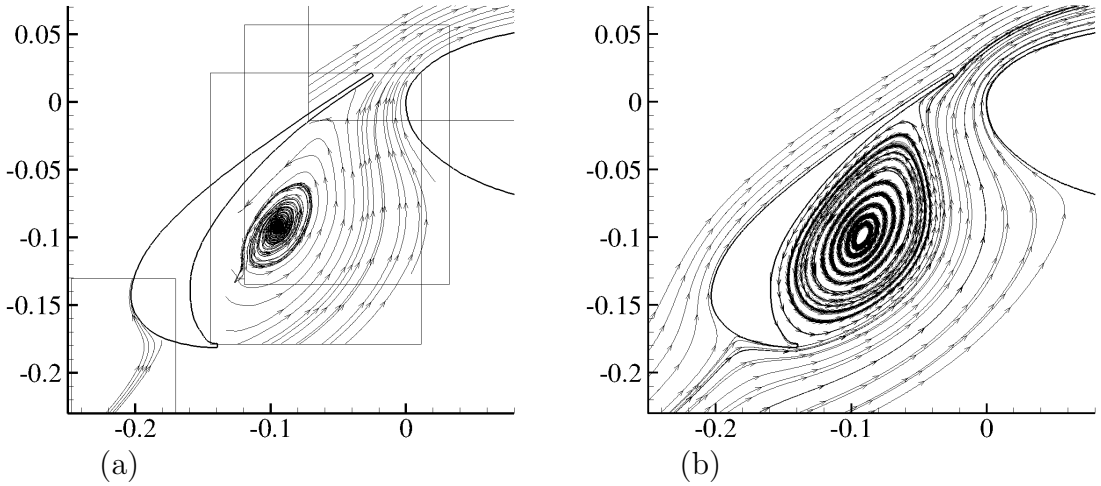

FIGURE 4.11: Streamlines in the slat region for the experiment and the simulation with CIIM of the RA16SC-1 three-element airfoil at $Re = 1.7 \times 10^6$.

The vortical structures shed at the trailing edge of the slat show negative and positive signs for spanwise vorticity indicating classic vortex shedding, see also Fig. 4.7(b). These vortices evidently do not pass through the gap between the slat and the main wing.

The vortical structures leaving the slat downstream perturb the main wing boundary layer beneath them, see Fig. 4.10. According to Paschal et al. [125] the vortical structures emerging from the slat cove hereby play a more important role than the ones shed at the trailing edge. Overall, qualitatively good agreement is observed with the related PIV experiments of Takeda [158] and Paschal et al. [125] as well as the DES of Deck [31].

Averaged Flow Field Fig. 4.11 compares the time-averaged streamlines in the slat region of the current simulation with the experimental PIV data of the EUROPIV 2 project. The experiment and simulation clearly show the same position for the stagnation point at $(x/c)_{slat,stag} = -0.19$ which gives further evidence that the chosen angle of attack in the simulation is correct. Experimental and numerical results exhibit a large recirculation region with separation at the slat cusp and reattachment in the slat cove near the trailing edge. The distance between the slat trailing edge and the reattachment point is $(l/c)_{slat,reatt} = 0.034$ in the experiment and $(l/c)_{slat,reatt} = 0.033$ in the current simulation, see also Table 4.1. The reattachment produces large velocity fluctuations as reflected in the turbulent kinetic energy contours in Fig. 4.12(a) and as reported by Moriatry et al. [109].

TABLE 4.1: Characteristic quantities for the RA16SC1 three-element airfoil at $Re = 1.7 \times 10^6$.

Study	$(x/c)_{slat,stag}$	$(l/c)_{slat,reatt}$	$(L_r/c)_{flap,sep}$
EUROPIV 2, experiment	-0.19	0.034	0.12
Deck [31], simulation (DES)	-0.19	0.035	0.0
Simulation on Cartesian grid + CIIM	-0.19	0.033	0.08

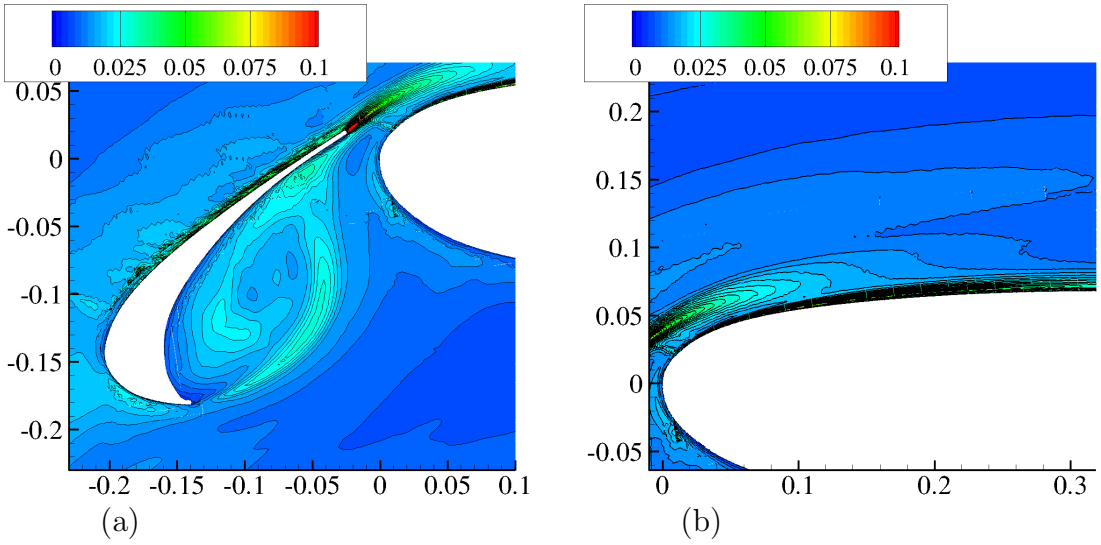

FIGURE 4.12: Contour maps of the turbulent kinetic engery (tke) in the slat area and on the suction side of the main wing of the RA16SC-1 three-element airfoil at $Re = 1.7 \times 10^6$.

Hereby the aforementioned secondary vortices are initiated [71], which are then distributed over the slat lower surface by the recirculation movement.

Fig. 4.11 also shows that the flow on the upper surface of the slat is attached. The high density of streamlines in the gap between slat and main wing, adjacent to the recirculation zone and near to the stagnation point imply strong flow acceleration in the slat region.

Zones of flow acceleration are clearly visible in the contour maps of the measured and the computed velocity magnitude shown in Fig. 4.13. The flow is accelerated on both sides of the stagnation point. On the suction side the flow is further accelerated up to the velocity peak and associated pressure peak (see also Fig. 4.6) at $x/c = -0.19$, then slightly decelerated down to the trailing edge of the slat. On the pressure side the flow is further accelerated until the slat cusp before it separates as a free shear layer, i.e. a mixing layer. This shear layer bounds the

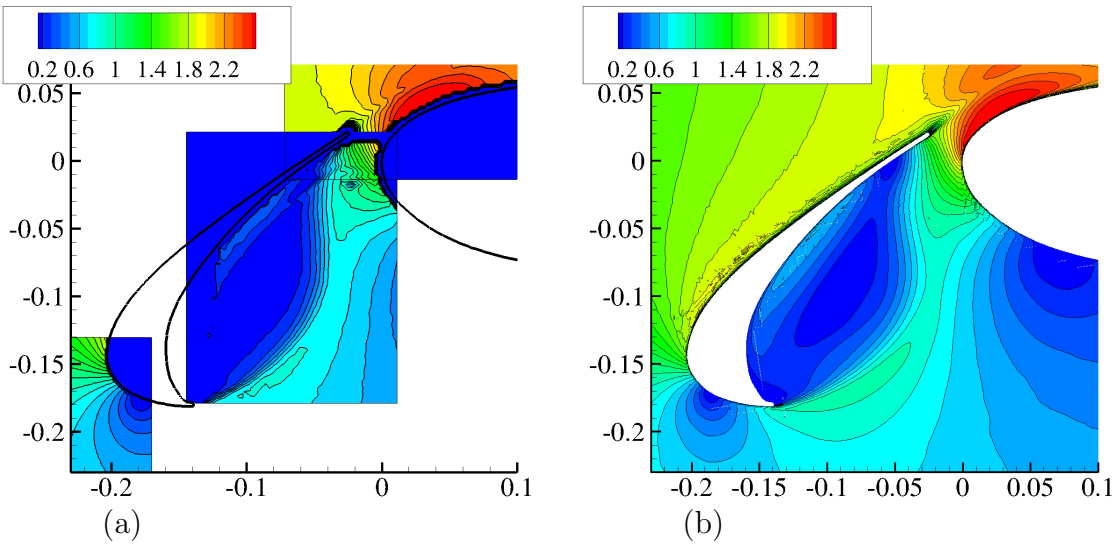

FIGURE 4.13: Contour maps of the velocity magnitude in the slat area for the experiment and the simulation with CIIM.

recirculation zone associated with low velocities. Across the shear layer a strong velocity differential is apparent. When the shear layer passes through the gap between slat and main wing, the flow is considerably accelerated leading to the aforementioned stretching of vortical structures in streamwise direction. Please also note the unsteadiness of the slat wake implied by the high level turbulent kinetic energy, see Fig. 4.12(b).

For a more detailed study of the recirculation region and the bounding shear layer, turbulent statistics of the current simulation are compared to the experiments of the EUROPIV 2 project of Rake0. Fig. 4.14(a) shows the computed and measured mean velocity magnitude. The velocity gradient between the cove and the outer flow is significant. The simulation reproduces the measured center of the recirculation bubble defined by $(\langle u \rangle / u_\infty) = 0$ at $\delta/c = 0.04$ and the measured shear layer boundary defined by $(\langle u \rangle / u_\infty)_{max}$ at $\delta/c = 0.1$.

Fig. 4.15(a)-(d) show the streamwise velocity fluctuations, the crossflow velocity fluctuations, the spanwise velocity fluctuations and the turbulent kinetic energy for Rake0. Peaks for all components are visible in the region of the shear layer at $\delta/c = 0.1$ indicating that the shear layer is unsteady. For the streamwise and crossflow velocity fluctuations another peak is located in the recirculation bubble at $\delta/c = 0.02$. The flow seems to be highly three-dimensional in the region where the flow reverses as reflected by the spanwise velocity fluctuations in Fig. 4.15(c).

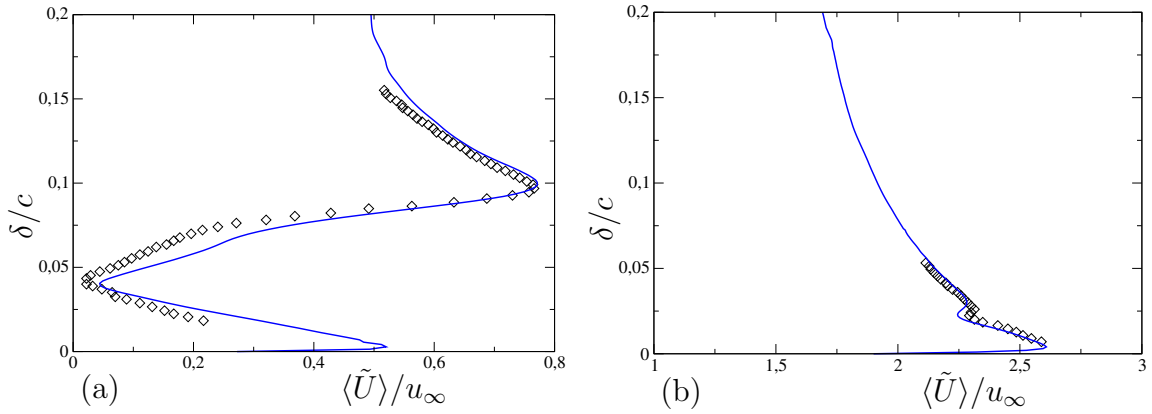

FIGURE 4.14: Velocity magnitude at Rake0 and Rake1 for the RA16SC-1 three-element airfoil at $Re = 1.7 \times 10^6$ ($\diamond$: experimental data EUROPIV 2, ——: present method)

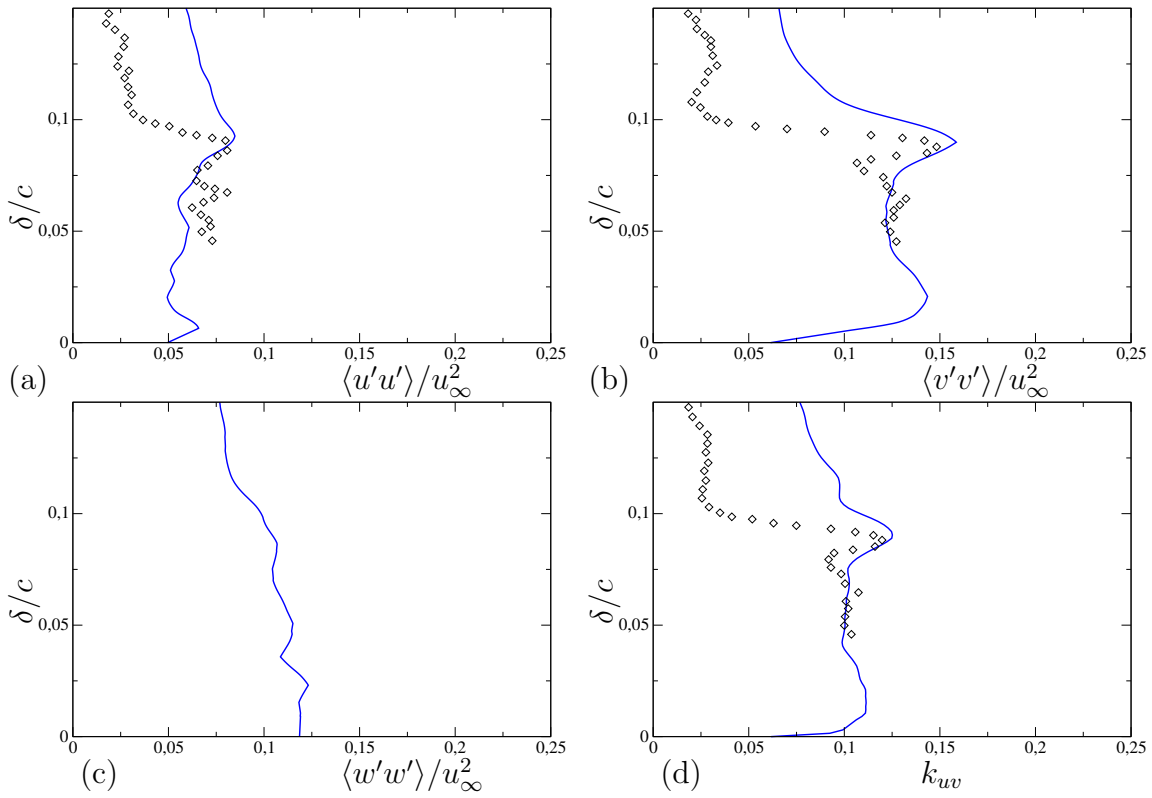

FIGURE 4.15: Streamwise velocity fluctuations, crossflow velocity fluctuations, spanwise velocity fluctuations and turbulent kinetic energy at Rake0 for the flow over the RA16SC-1 three-element airfoil at $Re = 1.7 \times 10^6$ ($\diamond$: experimental data EUROPIV 2, ——: present method).

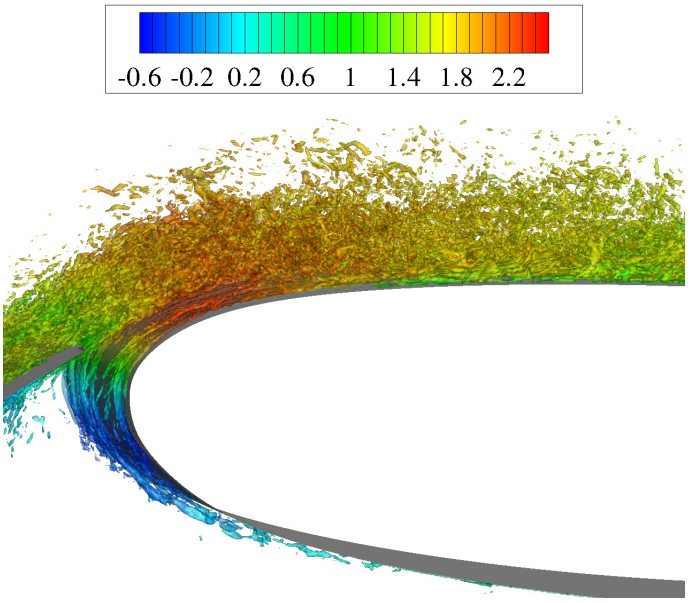

FIGURE 4.16: Instantaneous vorticity magnitude isosurface colored by streamwise-velocity on the suction side of the main wing of the RA16SC-1 three-element airfoil at $Re = 1.7 \times 10^6$.

4.3.3 Flow over the Main Wing

The main wing takes the major part of the aerodynamic wing loading. An accurate prediction is therefore necessary for determining correct global aerodynamic coefficients and the overall aerodynamic characteristics of the wing configuration in the preliminary design process.

Instantaneous Flow Field The vortices leaving the slat impinge into the main wing boundary layer and trigger its development and laminar-turbulent transition, see Fig. 4.16. When the longitudinal vortices from the slat cove hit the boundary layer they are partially merged with the vortices of the boundary layer, partially convected downstream. Moving towards the trailing edge of the main wing the turbulent boundary layer flow is slowed down by the adverse pressure gradient.

In the flap cove of the main wing the turbulent structures are similar to those found in the slat cove. Again a recirculation zone dominates the flow physics. It is bounded by a shear layer that separates from the flap cove lip on the lower surface of the main wing, rolls up into vortices rotating in spanwise direction with a positive sign (see Fig. 4.17(a)) that become three-dimensional and unsteady when approaching the reattachment zone in the flap cove, see Fig. 4.18. Some of these vortices interact with the recirculation bubble and induce eruptions of secondary

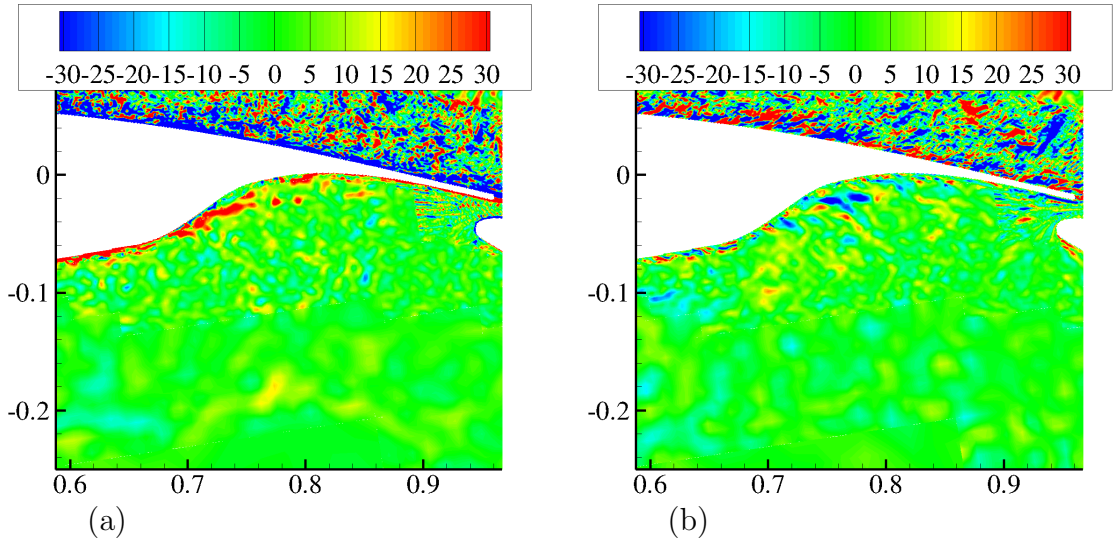

FIGURE 4.17: Contour maps of the spanwise $\omega_z c/u_\infty$ and the streamwise vorticity $\omega_x c/u_\infty$ in flap cove area of the RA16SC-1 three-element airfoil at $Re = 1.7 \times 10^6$.

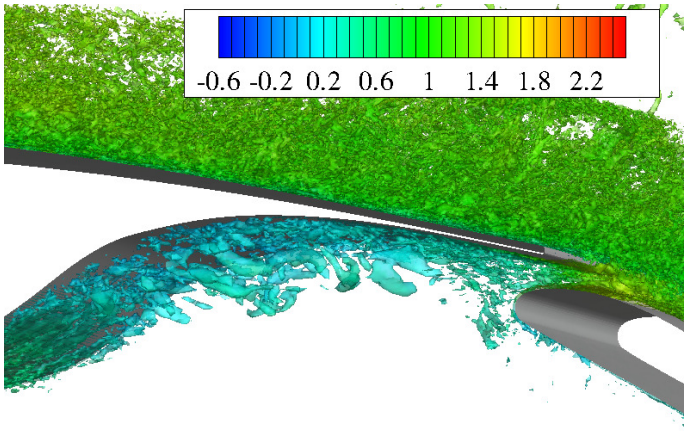

FIGURE 4.18: Instantaneous vorticity magnitude isosurface colored by streamwise-velocity in the flap cove of the main wing of the RA16SC-1 three-element airfoil at $Re = 1.7 \times 10^6$.

vortices in the near wall region of the flap cove. When diverted back towards the reattachment region, the entrained vortices partially merge with the vortices of the separated shear layer, see Fig. 4.17(a). Vortices that are not entrained in the recirculation region are directed towards the trailing edge of the main wing. The vortical structures are deformed and stretched in streamwise direction when the flow is accelerated in the gap between main wing and flap, see Fig. 4.17(b).

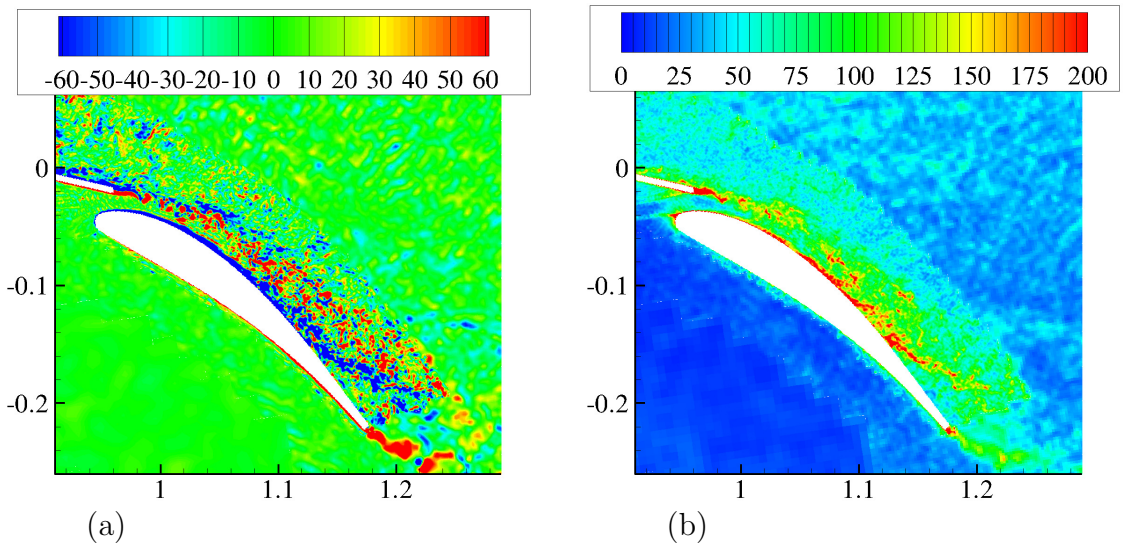

FIGURE 4.19: Contour maps of the spanwise vorticity and the shear in the flap area of the RA16SC-1 three-element airfoil at $Re = 1.7 \times 10^6$.

At the trailing edge of the main wing vortex shedding occurs, see Fig. 4.19(a) and (b). These vortices partially interact with those generated in the flap region and those of the turbulent boundary layer of the main wing before impinging into the boundary layer of the flap.

Averaged Flow Field Fig. 4.20(a) and (b) show the contour maps of the measured and the calculated time-averaged velocity magnitude near the leading edge of the main wing. Both in the experiment and the simulation the flow accelerates up to the position $x/c = 0.025$ where $(\langle C_p \rangle)_{min,main}$ is reached and is then decelerated down to the trailing edge due to the adverse pressure gradient. The merging process of the slat wake with the main wing boundary layer is clearly visible. With increasing running length the growing wing boundary layer pushes the slat wake away from the surface. However, in the simulation this phenomenon is more pronounced than in the experiment. This difference between experiment and simulation will be studied more thoroughly by comparing the measured and computed turbulent statistics at Rake1, Rake2 and Rake3.

Fig. 4.14(b) displays the measured and computed mean velocity magnitude at Rake1. The mass deficit due to the slat wake is slightly more pronounced in the simulation than in the experiment. This can be attributed to a higher turbulence level in the experiment leading to a more intense merging process. The agreement between simulation and experiment is good.

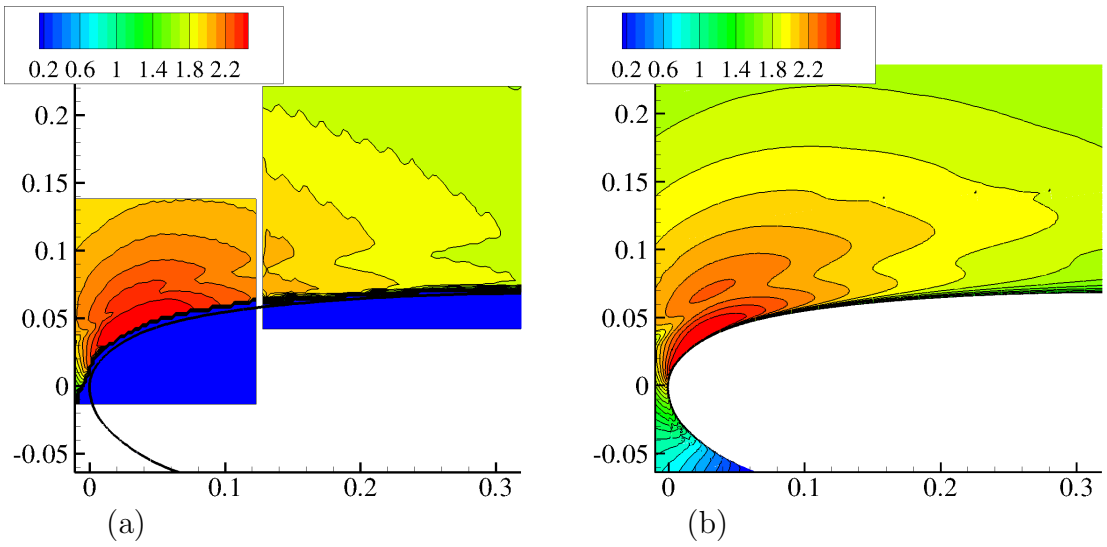

FIGURE 4.20: Contour maps of the velocity magnitude in the main wing area for the experiment and the simulation with CIIM.

The velocity fluctuations at Rake1 shown in Fig. 4.21(a)-(c) indicate the unsteadiness of the impinging slat wake. For the streamwise velocity fluctuations the same peak as for the mean velocity magnitude is visible. The considerable values of the spanwise velocity fluctuations underline the three-dimensionality of the flow. The high values for the turbulent kinetic energy (see Fig. 4.21(d)) at the wall can be attributed to the turbulent flow structures emanating from the slat cove, see also Fig. 4.12(b).

Further downstream at Rake2 the agreement of computed mean streamwise velocity (see Fig. 4.22(a)) is good. The mass deficit, i.e. the slat wake, is located at $\delta/c = 0.03$ in the experiment and at $\delta/c = 0.032$ in the simulation. Please note that this merging process is most important for the correct prediction of the maximum lift coefficient [149]. According to the profiles' characteristics, e.g. the velocity gradient at the wall, the turbulence level of the boundary layer is slightly higher in the experiment. This can be at least partially attributed to the high turbulence level of the experimental setup already discussed in Deck [31]. Another influence can be expected from the wall-modeling approach that does not account for the strong pressure gradient and/or a lack of grid resolution[6]. This discrepancy is also responsible for the difference in measured and calculated $\langle C_p \rangle$ discussed before.

[6]This test case has been simulated three times; with increasing resolution related results improved slightly. However, a further increase of resolution would make the simulation impossible with available computational resources.

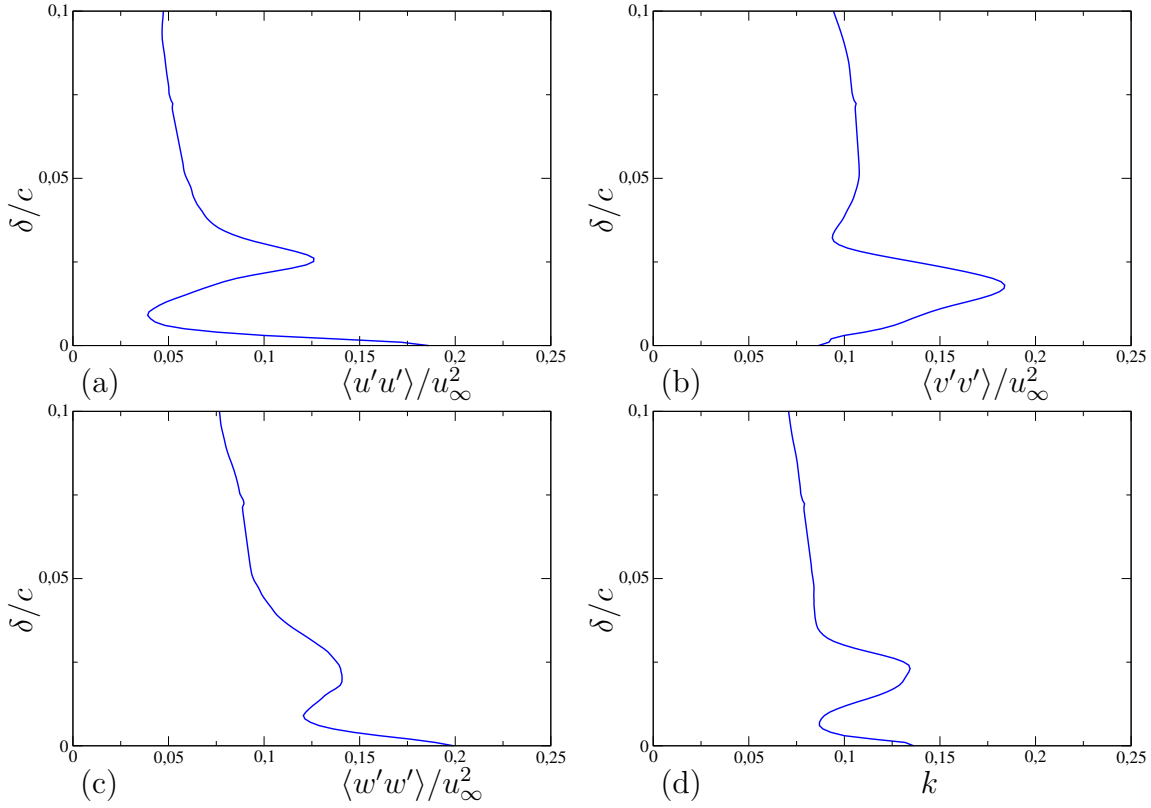

FIGURE 4.21: (a) Streamwise velocity fluctuations, (b) crossflow velocity fluctuations, (c) spanwise velocity fluctuations and (d) turbulent kinetic energy at Rake1 for the RA16SC-1 three-element airfoil at $Re = 1.7 \times 10^6$ (——: present method).

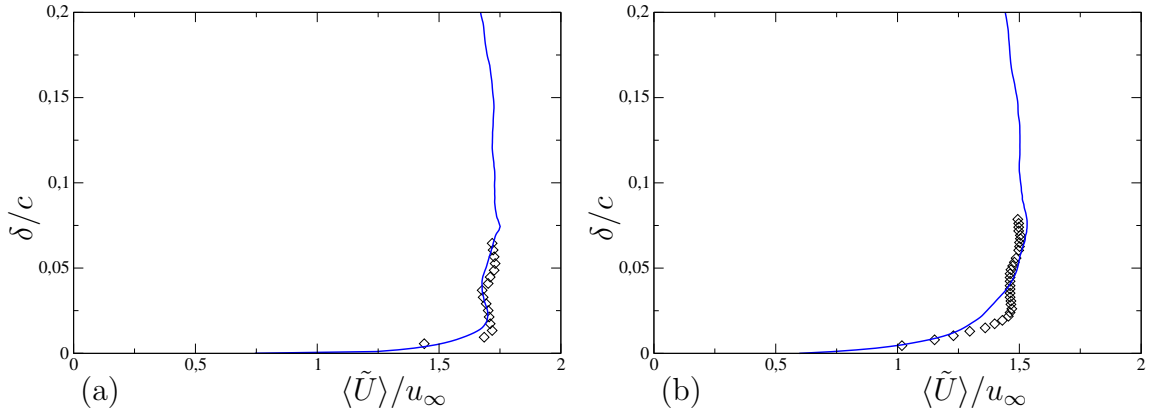

FIGURE 4.22: Velocity magnitude at (a) Rake2 (b) Rake3 for the RA16SC-1 three-element airfoil at $Re = 1.7 \times 10^6$ (◇: experimental data EUROPIV 2, ——: present method).

The findings at Rake2 also apply to the mean velocity magnitude at Rake3, shown in Fig. 4.22(b).

4.3.4 Flow over the Flap

The flow over the flap is strongly affected by the flow physics upstream (see Fig. 4.23) and their correct representation by the simulation. Previous simulations [31] of this test case have not been able to reproduce the separation of the experiment. However, the correct prediction of the flow over the flap is essential for the sustainable usage of CFD in the industrial environment.

Instantaneous Flow Field Most of the vortices passing the trailing edge of the main wing penetrate into the developing boundary layer on the flap and trigger laminar-turbulent transition, i.e., vorticity is distributed in all three space dimensions, see Fig. 4.19(b) as well as Fig. 4.24(a) and (b).

The vortical structures turning with a positive sign in spanwise direction seem to induce a "flapping" separation of the flap shear layer, see Fig. 4.19(a). Hereby the flap-cove flow with vortical structures elongated in streamwise direction show a cushioning or shielding behavior. Excited by the discrete vortices of the Kevin Helmholtz instability of the trailing edge of the main wing the separated shear layer becomes almost immediately unstable and rolls up into discrete vortices, see Fig. 4.19(b).

Close to the separation of the unsteady shear layer the flapping of this separated shear-layer induces secondary vortices, see Fig. 4.19(a). The separated shear layer bounds a recirculation zone entraining some of the vortices. Again these vortices generate further vorticity when the shear layer convects them along the upper surface of the flap. Vortex merging is also visible.

Averaged Flow Field The averaged streamlines of the experiment, Fig. 4.25(a), show a smaller recirculation bubble than the current simulation, Fig. 4.25(b), see also Table 4.1. This will be investigated in the following paragraphs.

In Fig. 4.26(a) and (b) the measured and the calculated velocity magnitude contour are compared. Both show the acceleration of the flow in the gap between the main

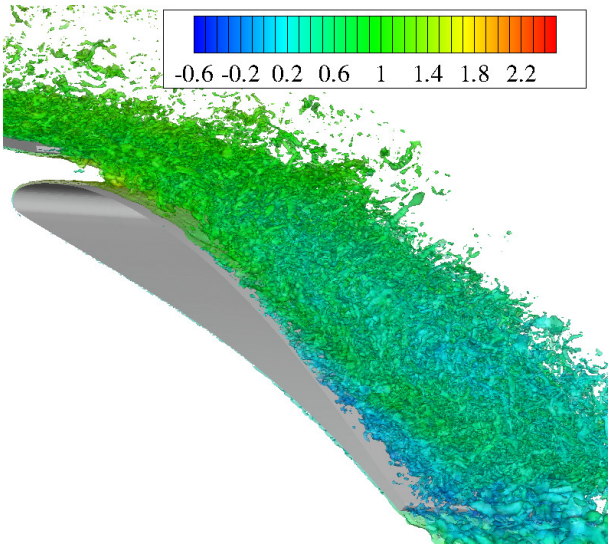

FIGURE 4.23: Instantaneous vorticity magnitude isosurface colored by streamwise-velocity in the flap region of the RA16SC-1 three-element airfoil at $Re = 1.7 \times 10^6$.

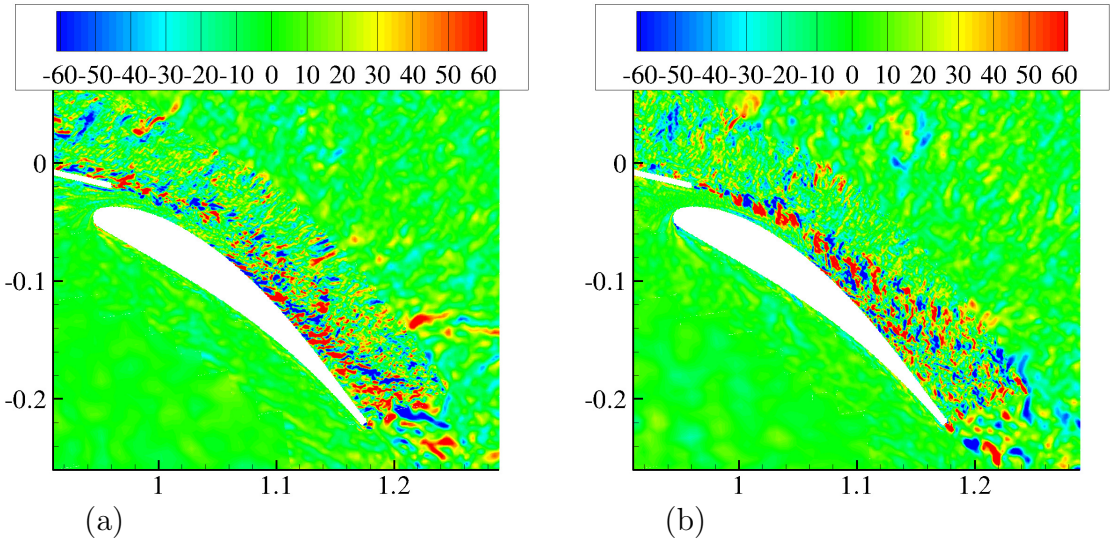

FIGURE 4.24: Contour maps of the streamwise $\omega_x c/u_\infty$ and the crossflow vorticity $\omega_y c/u_\infty$ in the flap area of the RA16SC-1 three-element airfoil at $Re = 1.7 \times 10^6$.

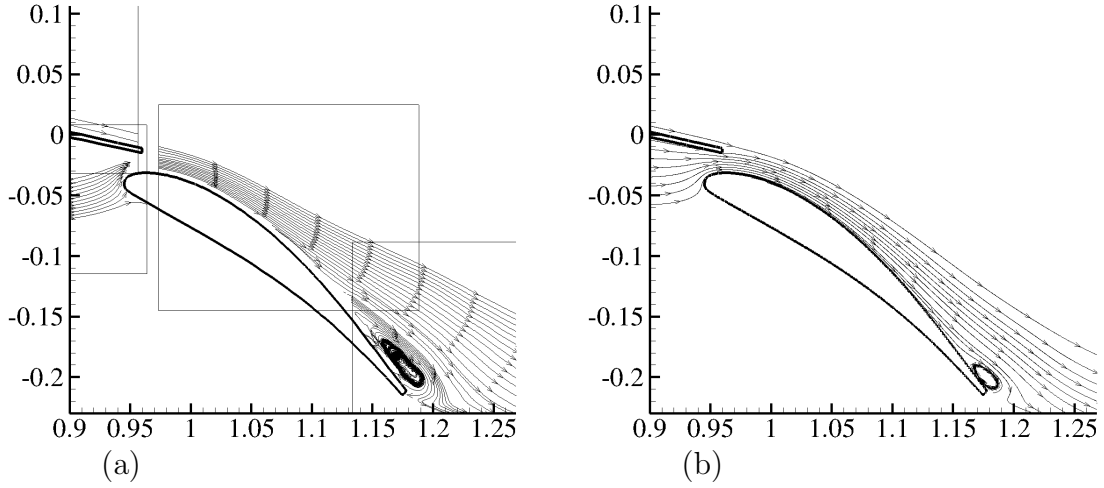

FIGURE 4.25: Streamlines in the flap region for the experiment (a) and for the simulation with CIIM (b) of the RA16SC-1 three-element airfoil at $Re = 1.7 \times 10^6$.

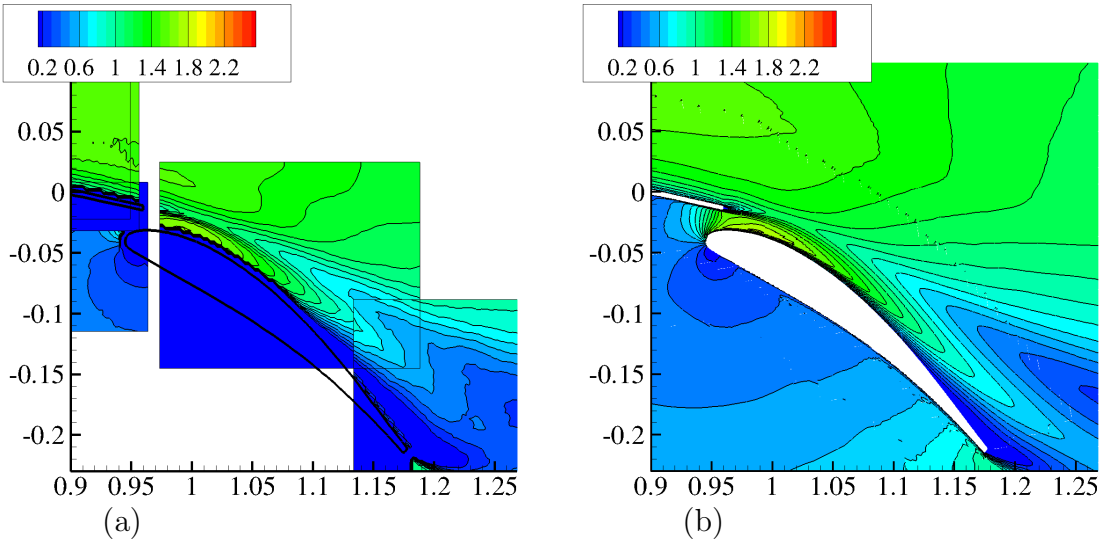

FIGURE 4.26: Contour maps of the velocity magnitude in the flap area for the experiment (a) and for the simulation with CIIM (b) of the RA16SC-1 three-element airfoil at $Re = 1.7 \times 10^6$.

wing and the flap. However, the contour lines of the shear layer leaving the upper surface of the main wing differ: in the experiment the dip for the mass deficit due to the slat wake is closer to the surface than in the simulation.

For a more detailed investigation the measured and calculated turbulent statistics at Rake4 are compared. In Fig. 4.27(a) the mean velocity magnitude shows good agreement for the accelerated gap flow. It is therefore concluded that the simulation correctly predicts the flow physics of the flap cove. The agreement for the

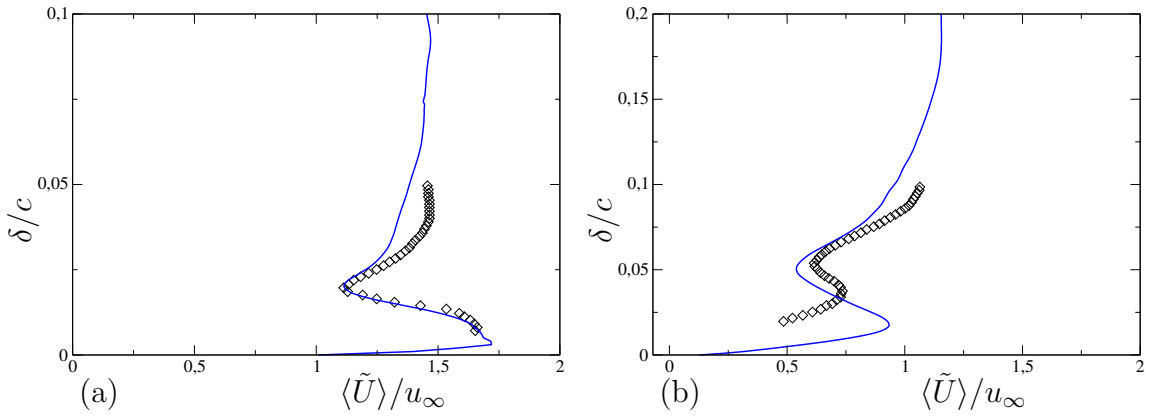

FIGURE 4.27: Velocity magnitude at Rake4 and Rake5 for the RA16SC-1 three-element airfoil at $Re = 1.7 \times 10^6$ ($\diamond$: experimental data EUROPIV 2, ——: present method).

mass deficit for the main wing wake is also good. However, the agreement for the main wing boundary layer now separated from the main wing, i.e. $\delta/c > 0.03$, is in line with the findings for the previously discussed rakes and is considered less satisfactory.

The velocity fluctuations in Fig. 4.28(a)-(d) show two considerable peaks: at $\delta/c = 0.01$ for representing the small-scale vortex shedding at the blunt trailing edge of the main element and at $\delta/c = 0.03$ associated with the turbulent boundary layer over the main wing and the slat wake. Fig. 4.28(a) and (c) clearly depicts the unsteadiness in all three spatial directions. The higher turbulent kinetic energy Fig. 4.28(d) implies a higher turbulence level of the numerical simulation compared to the experiment. This higher turbulence level is assumed to delay the separation of the flap boundary layer making the recirculation bubble smaller compared to the experiment.

Fig. 4.27(b) shows the measured and the calculated mean velocity profiles at Rake5 located in the region of the recirculation bubble. In comparison with the experiment the simulation shows an established recirculation region and it places the mass deficit at a low position. On the simulation side discrepancies can be attributed to differences in the characteristics of the impinging main wing boundary layer and to the lack of consideration of strong pressure gradient effects in the wall-model, i.e., incorrect prediction of the boundary layer growth and respective deflection of the wake. Furthermore, discrepancies are expected due to the non-constant pressure gradient in the experiment [31].

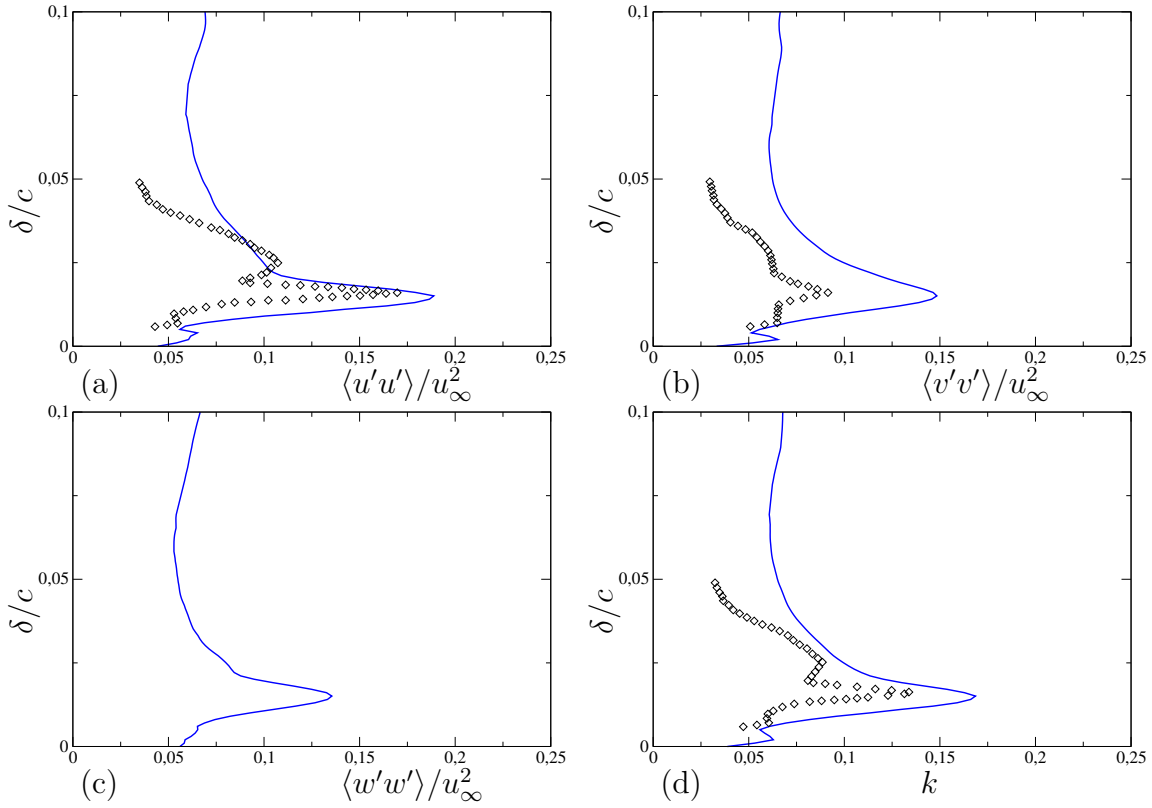

FIGURE 4.28: Streamwise velocity fluctuations, crossflow velocity fluctuations, spanwise velocity fluctuations and turbulent kinetic energy at Rake4 for the RA16SC-1 three-element airfoil at $Re = 1.7 \times 10^6$ ($\diamond$: experimental data EUROPIV 2, ——: present method).

4.4 Summary

In this chapter CIIM in combination with a wall-model based on the Thin-Boundary Layer Equations (TBLE) [19] has been applied in the investigation of the flow over the 3-element RA16SC-1 airfoil.

The use of this configuration was the best compromise between a geometry model that was not too complex in shape to gain optical access for PIV, but from a flow physics point of view still complex enough to be representative for industrial highlift systems. The correct prediction of the global flow physics requires an accurate representation of wall-bounded turbulence and poses a major challenge for LES on a Cartesian adaptive grid on which the wall-boundary condition is imposed by CIIM.

The simulation has predicted the unsteady three-dimensional flow in the slat region correctly. The development, evolution and interaction of primary and secondary vortices in the simulation qualitatively has corresponded to the experimental data.

Further quantitative comparisons with experimental results have confirmed this agreement.

The flow of the slat influences the boundary layer development on the main wing. On the first part of the main wing the quantitative and qualitative agreement between experiment and simulation is good. Further downstream the simulation shows a more prominent growth of the turbulent boundary layer deflecting the slat wake upwards. Possible reasons have been identified: a lack of grid resolution, lack of consideration of pressure-gradients in the TBLE formulation, a higher turbulence level in the experiment as well as a non-constant pressure gradient in the experiment.

Despite this discrepancies, the experimental flow physics on the flap are represented qualitatively well in the simulation. In particular this LES, as opposed to former simulations, is capable to reproduce the separation on the flap observed in the experiment. However, due to an over-predicted boundary layer growth with respect to the experiment the upward deflection of the main wing wake is overpredicted and the quantitative agreement is less satisfactory. Here, in particular it is assumed that the TBLE formulation has problems with large flow separation.

Considering that no parameter adjustments in turbulence model or wall model have been made, the agreement between experiment and simulation is promising. The good agreement with the experiment in regions not-requiring any wall model, underlines the modeling ability of CIIM. Its usage of less than 2% of computational resources[7] throughout the computations further underlines its suitability for industrially relevant configurations.

[7]Simulations have been performed on a NEC architecture using Intel Westmere X5650 processors with a Nehalem microarchitecture.

Chapter 5

First Results for the Application to the Flow over a Delta Wing

The industrial application of slender delta wings is manifold and reaches from the classical aerospace engineering, e.g. highly agile aircraft, aerodynamic devices or control surfaces, to unique environmental technologies, such as devices for snow clearance. In all cases the development of leading edge vortices is exploited. However, steadiness and stability of these leading edge vortices are essential for controllability, particularly for highly agile aircraft. These vortices can undergo a sudden expansion often related to vortex breakdown [90].

As a generic aerodynamic configuration the international Vortex Flow Experiment 2 (VFE-2) Delta-Wing, which has been used within the RTO/AVT 113 project for extensive experimental as well as theoretical investigations, has been chosen. The VFE-2 has 65° leading edge sweep and is equipped with different Leading Edges (LE): Sharp (S), Rounded with a Small radius (RS), with a Medium radius (RM) and a Large radius (RL). Here the RM-case is considered for which shear layer separation is not purely geometrically-defined as for the S-case. Instead the shear-layer laminar-turbulent transition constitutes a sensitive interaction process with separation and roll-up. For a Reynolds number of 1.0×10^6 based on the root chord length c_r and with increasing angle of attack α, the flow around the RM-case wing undergoes three major regimes: (1) at $\alpha = 13°$: partially attached, partially separated flow, (2) at $\alpha = 18°$: separated flow without vortex breakdown and (3) at $\alpha = 23°$: separated flow with vortex breakdown.

A profound understanding of vortex formation and breakdown requires a comprehensive insight into the complete unsteady flowfield. This insight can only be obtained from time-accurate simulations accompanied by experiments. Previous RANS simulations with statistical turbulence models have failed to accurately predict the separation of a comparable test case, i.e. the separated flow around a flat plate at high incidence [12]. In the case of the VFE-2 Delta-Wing RANS results so far do not compare well with existing experimental data [111]. Slightly better results have been achieved with DES with appropriate modifications [111]. A first LES employing wall functions with acceptable results was carried out by Mary [96]. Better results can be expected from an Implicit LES with a more sophisticated wall-modeling approach based on the Thin Boundary Layer Equations (TBLE) [19]. Here some first results on a coarse grid will be shown. This test case proves that CIIM goes beyond other reported cut-cell methods [103] by being applicable to three-dimensional geometries of arbitrary shape.

5.1 Computational Setup

5.1.1 Numerical Method

The flow is described by the incompressible Navier-Stokes equations discretized on a staggered Cartesian grid. The convective terms are discretized with the Adaptive Local Deconvolution Method (ALDM) [64], in which Sub-Grid Scales (SGS) are implicitly modelled by the truncation error of the discretization. The explicit third-order Runge-Kutta scheme of Shu [142] is used for time advancement. The time-step is dynamically adapted to satisfy the Courant-Friedrichs-Lewy condition CFL = 0.3. The diffusive terms and the pressure-Poisson equation are discretized by second-order centered differences. The Poisson solver employs the stabilized Bi-Conjugate Gradient (BiCGstab) method [146, 174] in all flow directions. The Poisson equation is solved at every Runge-Kutta substep.

5.1.2 Computational Domain and Boundary Conditions

The computational domain is shown in Fig. 5.1. Since no vortex burst is expected at $\alpha = 13°$ simulating a half-model with symmetry conditions is suitable. The

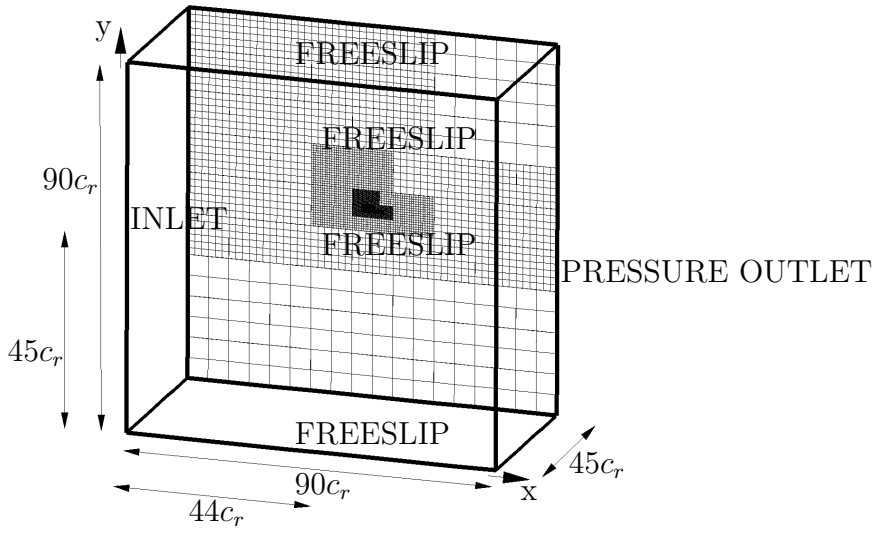

FIGURE 5.1: Computational setup for the flow over the VFE-2 Delta Wing at $Re = 0.5 \times 10^6$ and $\alpha = 13°$ (every third computational cell is shown, spanwise extent is 100 times magnified for better visualization).

farfield is chosen to be at least 45 c_r away from the profile. At the inlet a uniform velocity profile and at the outlet a pressure condition is defined. At the other sides free-slip boundary conditions are imposed.

Wall boundary conditions are imposed with CIIM in connection with a Thin-Boundary-Layer-Equation (TBLE) based wall-model [19]. The coupling position between wall-model and LES is located in the logarithmic region of the boundary layer.

5.1.3 Computational Grid

The computational domain is subdivided into 5400 blocks with 7 different grid refinement levels and consists of a total number of 16×10^6 cubic computational cells, see Fig. 5.2. In the vicinity of the immersed interface cell sizes correspond to $\Delta y^+ = 60$ being a good value based on the experiences made for turbulent boundary layers with a TBLE wall-model [19]. Refined regions are located on the upper surface of the wing up to the wall distance $d/c_r = 0.15$. Downstream of the wing the sting is not as well-resolved since it is assumed to have only displacement character.

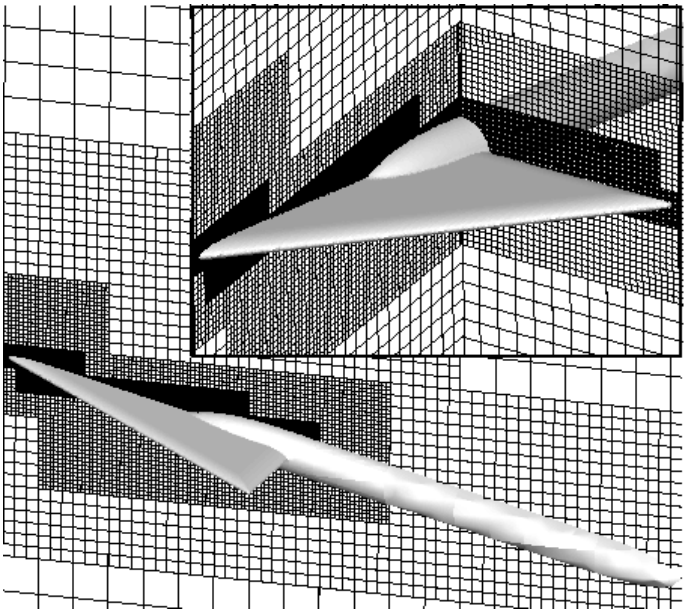

FIGURE 5.2: Computational grid for the flow over the VFE-2 Delta Wing at $Re = 0.5 \times 10^6$ and $\alpha = 13°$ (every third computational cell is shown).

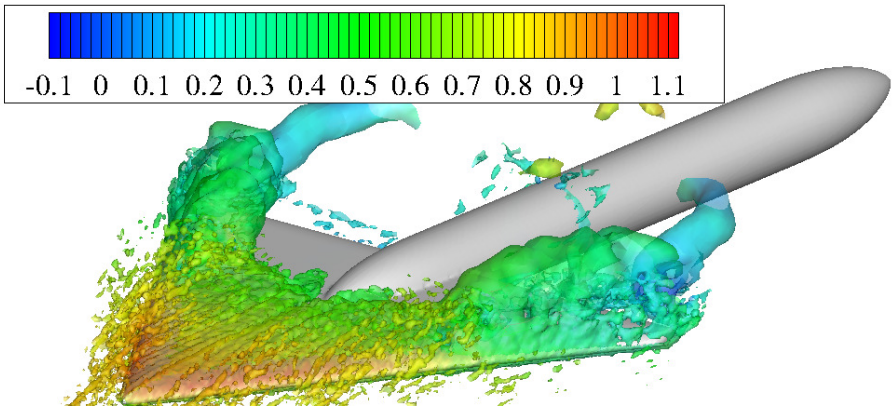

FIGURE 5.3: Isosurface of streamwise vorticity colored by streamwise velocity for the VFE-2 Delta Wing at $Re = 0.5 \times 10^6$ and $\alpha = 13°$.

5.2 Results

The results have been obtained for a Reynolds number $Re = 0.5 \times 10^6$ based on the root chord length c_r and $\alpha = 13°$. The objective is to reach a qualitative agreement with the respective experiments of Furman and Breitsamter [51].

For this angle of attack both, experiment [51] and the current simulation, show vortex formation over half chord length, see Fig. 5.3. Close to the apex the boundary layer flow accelerates over the leading edge and undergoes laminar-turbulent transition. This is also reflected by the high suction levels visible in Fig. 5.4. Severe pressure gradients in lateral direction provoke boundary layer separation further

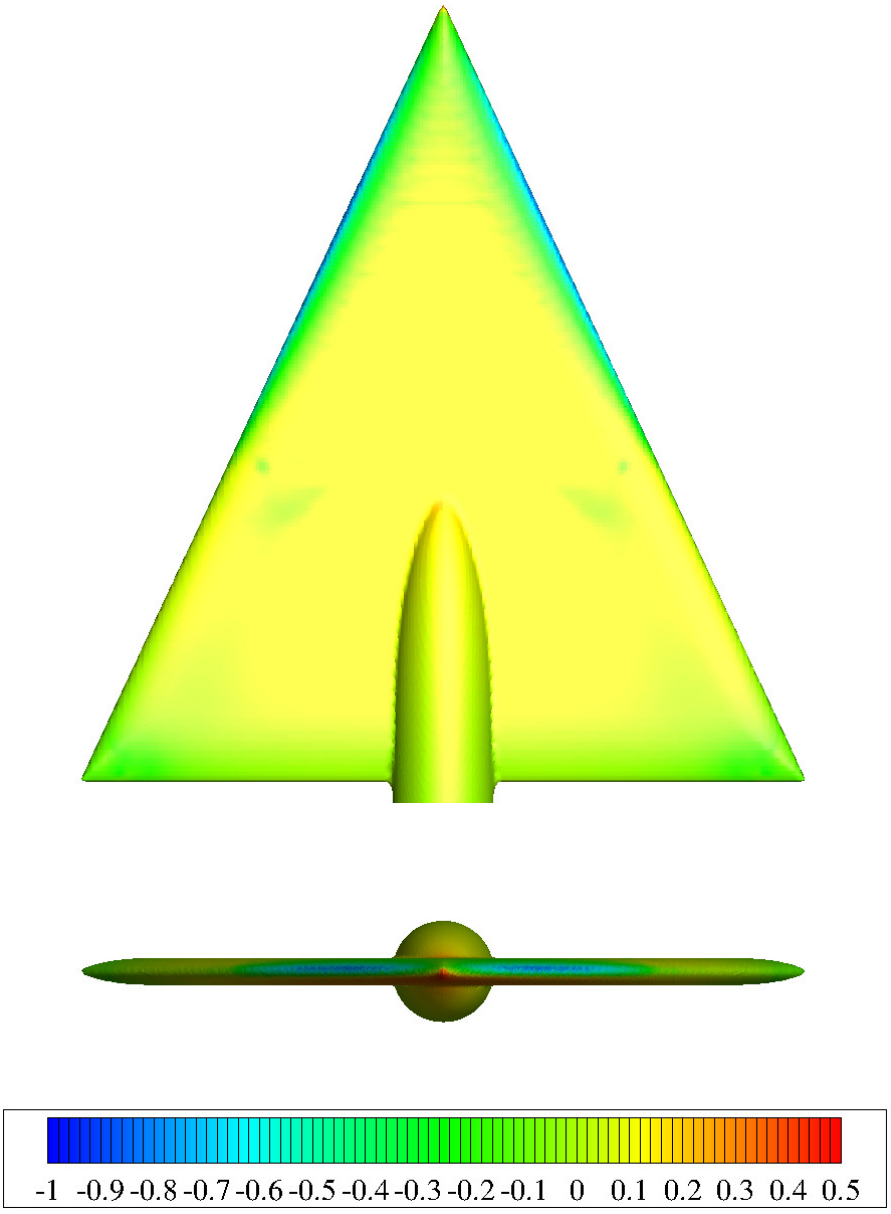

FIGURE 5.4: C_p distribution on the upper (top) and front (bottom) surface of the VFE-2 Delta Wing at $Re = 0.5 \times 10^6$ and $\alpha = 13°$.

downstream. The separation region is indicated by the low pressure regions on the upper surface of the wing (see Fig. 5.4).

Fig. 5.5 shows the shear in the vortex cross flow area at different streamwise positions ($x/c_r = 0.6, 0.7, 0.9$ and 1.1). The separated boundary layer rolls up by self-induction and creates a large-scale primary vortex at $x/c_r = 0.6$ inducing a secondary vortex at $x/c_r = 0.7$. At $x/c_r = 1.1$ only the wake vortices are visible. Similar findings have been made in the experiment [51].

Fig 5.6 shows the pressure coefficient distribution in the vortex cross flow area at

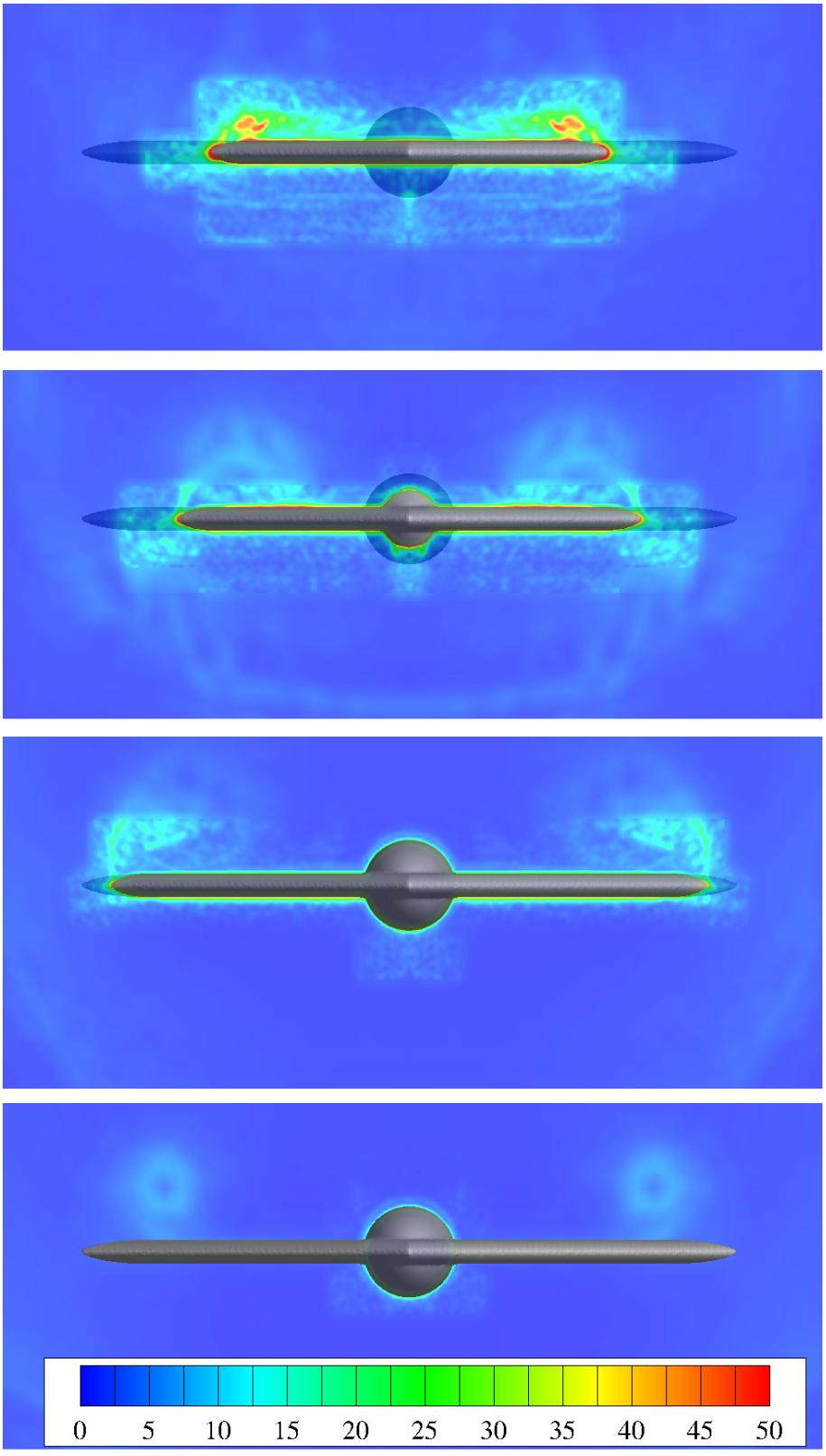

FIGURE 5.5: Slices at $x/c_r = 0.6,\ 0.7,\ 0.9$ and 1.1 showing τ for the VFE-2 Delta Wing at $Re = 0.5 \times 10^6$ and $\alpha = 13°$.

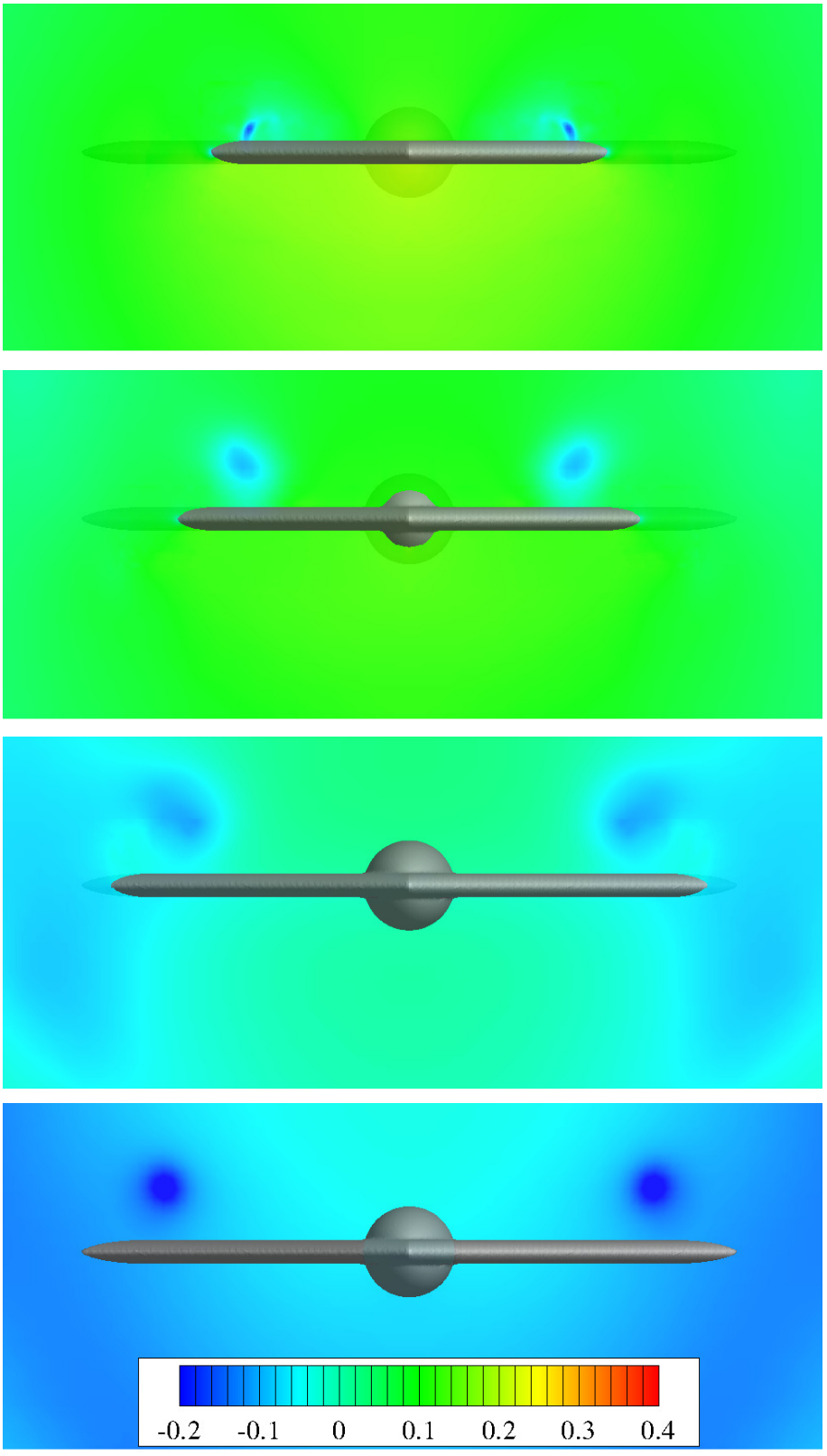

FIGURE 5.6: Slices at $x/c_r = 0.6,\ 0.7,\ 0.9$ and 1.1 showing C_p for the flow over the VFE-2 Delta Wing at $Re = 0.5 \times 10^6$ and $\alpha = 13°$.

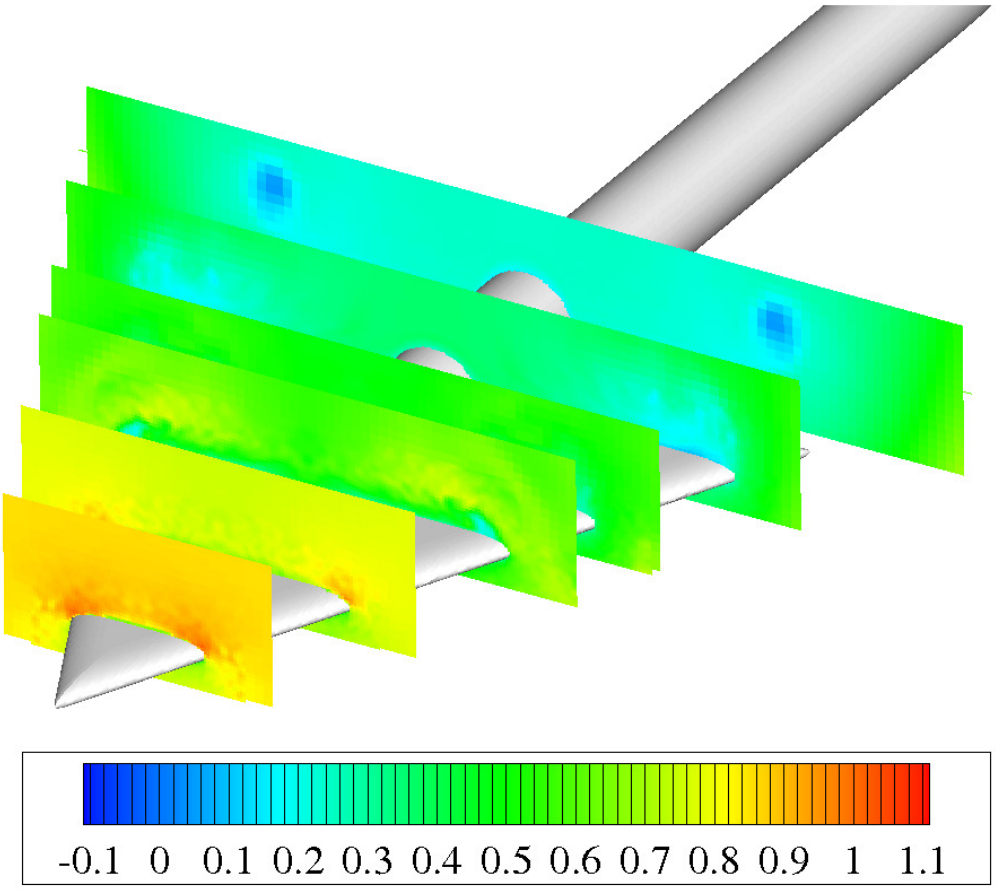

FIGURE 5.7: Slices at $x/c_r = 0.2,\ 0.4,\ 0.6,\ 0.7,\ 0.9$ and 1.1 showing the streamwise velocity for the flow over the VFE-2 Delta Wing at $Re = 0.5 \times 10^6$ and $\alpha = 13°$.

the same streamwise positions. In agreement with the previous findings, rotational cores at $x/c_r = 0.6$ with embedded subcores at $x/c_r = 0.9$ can be seen. The vortices on top of the wing are characterized by high axial velocities as indicated in Fig. 5.7. Please note that the high suction levels are not generated by the leading edge vortices themselves but by the induced vortices on top of the wing. With increasing angle of attack the induced vortices become stronger before they burst. This bursting process is not fully understood and thus the desire to fully exploit the beneficial effect of the induced vortices on the total lift gives the motivation for further investigation also at $\alpha = 18°$ and $23°$.

5.3 Summary

In this chapter CIIM has been applied in the simulation of the flow over the VFE-2 Delta Wing at an angle of attack of 13° and a Reynolds number of $Re = 0.5 \times 10^6$ based on the root chord length. While the industrial application of delta wings is vast and, their complex flow physics are yet not well understood. The good qualitative agreement with respective experiments gives proof that CIIM is also applicable to three-dimensional geometries of arbitrary shape and can be used in further investigations of this test case.

Chapter 6

Summary and Conclusion

In this thesis, a Conservative Immersed Interface Method (CIIM) has been developed for imposing the wall boundary condition of bodies of arbitrary shape in incompressible LES on Cartesian grids. For industrial applicability of LES computational resources should be minimal and grids should be generated automatically.

The generation of suitable structured body-fitted grids for LES of complex flows can be time-consuming and difficult. Contradictory requirements, such as adequate local resolution and minimum number of grid cells, can deteriorate the grid quality and therefore adversely affect accuracy and numerical convergence properties. Unstructured body-fitted grids without rather severe constraints on cell size and aspect ratio, however, are known to be not well-suited for time-resolving turbulent flow computations, in particular for LES. The alternative approach is to use Cartesian grids, which also facilitates automatic grid generation and local grid refinement. Cartesian grids imply fewer computational operations per grid point than body-fitted or unstructured grids. On the other hand, bounding surfaces of the flow or immersed obstacles need to be accounted for by mapping the boundaries onto the grid with an Immersed Interface Method (IIM).

For combined usage with LES, the IIM should maintain accuracy and conservation as well as should offer a sharp interface representation also for moving interfaces. In IIMs using a continuous forcing approach a distributed forcing function inserted into the momentum equations mimics the interaction at the interface. This approach smears sharp interfaces over an area corresponding to the local mesh width and lacks of discrete conservation. For IIMs with a discrete forcing function in the

momentum equations accurate representation of the boundary has been demonstrated while the approach also lacks discrete conservation. Similarly, ghost-cell approaches and reconstruction methods, both employing interpolation to impose the boundary conditions at the interface, are generally not conservative. Another discrete forcing approach is the cut-cell method in which cells cut by the immersed interface are truncated so that they conform to the shape of the boundary surface. The cut-cell method is based on a finite-volume discretization and generally maintains discrete conservation. A common problem of cut-cell methods is the creation of very small fluid cells that lead to numerical instability if left untreated but according to more recent publications this problem can be overcome. On the other hand, second-order accuracy has been achieved only by a small number of methods and methods based on a staggered formulation having better stability properties then those methods with a collocated formulation are even more scarce. Above all, for industrial applications, complex geometries and moving boundaries, not only accuracy and conservation but also a simpler geometry representation is desirable.

The purpose of this thesis has therefore been to develop CIIM, an efficient, conservative, second-order accurate Cartesian cut-cell method for the incompressible Navier-Stokes equations on three-dimensional non-uniform staggered grids which is suitable for an extension to moving boundaries and fluidstructure interaction. CIIM is applicable to any underlying finite volume discretization. A zero-level-set contour represents the interface, which also allows to handle topological changes naturally. CIIM operates on fluxes of cut cells only and therefore ensures both mass and momentum conservation. Friction forces on the immersed interface are accounted for by a friction term. The boundary condition of the normal velocity is satisfied by a momentum-exchange term and by imposing a homogeneous Neumann condition in the pressure projection. To ensure numerical stability a conservative mixing procedure is employed.

The performance of CIIM is studied in various validation cases. Second-order grid convergence has been proven for the decrease of the velocity profile error of the inclined channel flow at $Re = 20$ and for the decrease of the lift and drag coefficient error of the square and circular cylinder flow at $Re = 100$. For the flow over a circular cylinder at $Re = 100$ it was furthermore proven that the threshold for the small cell mixing does not significantly affect the accuracy of the results. The local flow physics at the interface are proven to be modeled

correctly for the developed laminar channel flow at $Re = 20$, the separated laminar circular cylinder flow at $Re = 40$, the separated circular cylinder flow with laminar-turbulent transition at $Re = 3900$ and the separated and reattached turbulent periodic hill flow at $Re = 10,595$. For all simulations conservation is ensured both locally and globally. Mass conservation is proven to be ensured discretely according to the accuracy threshold chosen in the POISSON solver, up to machine precision if desired. Even for the complex flow cases, i.e. the circular cylinder at $Re = 3900$ and the turbulent periodic hill flow at $Re = 10,595$, CIIM consumes only an insignificant amount of computational time and allows for a four times faster simulation compared to a respective simulation on a curvilinear grid with standard wall boundary conditions. It can be concluded that CIIM fulfills all desired features and shows a good performance.

To go a step beyond the scope of previously developed cut-cell methods CIIM is also applied in combination with a Turbulent-Boundary-Layer-Equations-based wall-model in two LES of industrial relevance: the flow over the RA16SC-1 3-element highlift airfoil and the flow over the VFE-2 delta wing. Both flows have never been studied with full LES on Cartesian adaptively refined grids before. The LES of the turbulent flow over the RA16SC-1 3-element highlift airfoil shows good agreement with experimental reference data and gives new insights into the prevailing flow physics. As opposed to former DES, the current investigation uses LES also for the representation of the merging process of the slat wake with the turbulent boundary layer on the main wing. Caused by the strong downstream influence of this process, the flow separation process on the flap observed in the experiment could be correctly predicted for the first time by this LES as opposed to previous DES. It is well-known, that this prediction-ability is an all-important feature for a simulation tool employed in highlift-system (preliminary) design. The LES of the flow over the VFE-2 delta wing shows that CIIM works for three-dimensional geometries of arbitrary shape. Qualitative flow physics are recovered in a coarse simulation. More thorough investigation on this test case will follow in subsequent works.

In conclusion, the novel Immersed Interface Method CIIM has been proven in various selected test cases to be an efficient, conservative and second-order accurate method with a sharp description of arbitrary bounding surfaces suitable for complex turbulent flow simulations on Cartesian (adaptive) grids.

Bibliography

[1] Adams, N. A., Hickel, S., and Franz, S. Implicit subgrid-scale modeling by adaptive deconvolution. *J. Comput. Phys. 200*, 2 (2004), 412–431.

[2] Almeida, G. P., Durao, D. F. F., and Heitor, M. V. Wake flows behind two-dimensional model hills. *Exp. Thermal Fluid Sci. 7* (1993), 87–101.

[3] Arakawa, A. Computational design for long-term numerical integration of the equations of fluid motion: two-dimensional incompressible flow part i. *J. Comput. Phys.*, 1 (1966), 119143.

[4] Arnott, A., Neitzke, K. P., Agocs, J., Sammer, G., Schneider, G., and Schröder, A. *Detailed Characterisation Using PIV of the Flow Around an Aerofoil in High Lift Configuration*, first ed. Springer-Verlag, Berlin, 2003. EUROPIV2 Image Velocimetry.

[5] Baggett, J. S., Jimènez, J., and Kravchenko, A. G. Resolution requirements in large-eddy simulations of shear flows. *Center for Turbulence Research Annual Research Briefs, NASA Ames/Stanford Univ* (1997).

[6] Batchelor, G. K. *An Introduction to Fluid Dynamics*, first ed. Cambridge University Press, Cambridge, 1967.

[7] Beaudan, P., and Moin, P. Numerical experiments on the flow past a circular cylinder at sub-critical reynolds number. *Center for Turbulence Research Annual Research Briefs, NASA Ames/Stanford Univ* (1994).

[8] Bell, J. B., Colella, P., and Glaz, H. M. A second-order projection method for the incompressible NavierStokes equations. *J. Comput. Phys.*, 85 (1989), 257–283.

[9] Breuer, M. New reference data for the hill flow test case. online, `http://www.hy.bv.tum.de/DFG-CNRS/`, 2005.

[10] Breuer, M., Jaffrézic, B., and Arora, K. Hybrid LESRANS technique based on a one equation near-wall model. *J. Theor. Comput. Fluid Dyn. 22*, 3-4 (2008), 157–87.

[11] Breuer, M., Jaffrézic, B., Peller, N., Manhart, M., Fröhlich, J., and Hinterberger, C. *A comparative study of the turbulent flow over a periodic arrangement of smoothly contoured hills.* ERCOFTAC Series. Direct and Large-Eddy Simulation VI, vol. 10. Springer-Verlag, New York, September 2006.

[12] Breuer, M., Jovicic, N., and Mazaev, M. Comparison of DES, RANS and LES for the separated flow around a flat plate at high incidence. *Int. J. Numer. Meth. Fluids 41* (2003), 357–388.

[13] Breuer, M., Peller, N., Rapp, C., and Manhart, M. Flow over Periodic Hills - Numerical and Experimental Study in a Wide Range of Reynolds Numbers. *J. Computers and Fluids 38*, 2 (2009), 433–457.

[14] Brunet, V., and Deck, S. F. *Zonal-detached eddy simulation of transonic buffet on a civil aircraft type configuration.* Springer-Verlag, Berlin, 2008.

[15] Canuto, C., Hussaini, M., Quarteroni, A., and Zang, T. A. *Spectral methods in fluid dynamics.* Springer-Verlag, Berlin, 1988.

[16] Cardell, G. S. Flow past a circular cylinder with permeable splitter plate. Data taken from R. Mittal, Progress on LES of flow past a circular cylinder, in Annual Research Briefs, pp. 233-241, Center for Turbulence Research, Stanford University, 1996.

[17] Chauvet, N., Deck, S., and Jacquin, L. Zonal detached eddy simulation of a controlled propulsive jet. *AIAA*, 45 (2007), 2458–73.

[18] Chen, S., and Doolen, G. D. Lattice Boltzmann method for fluid flows. *nnu. Rev. Fluid Mech.*, 30 (1998), 329–364.

[19] Chen, Z., Devesa, A., Meyer, M., Hickel, S., Lauer, E., Stemmer, C., and Adams, N. A. *Wall Modelling for Implicit Large Eddy*

Simulation of Favourable and Adverse Pressure Gradient Flows, first ed. Springer-Verlag, Heidelberg, 2010. Proceedings of WALLTURB Workshop Progress in Wall Turbulence - Understanding and Modelling, Lille 2009.

[20] Cheny, Y., and Botella, O. The LS-STAG method a new immersed boundary/levelset method for the computation of incompressible viscous flows in complex moving geometries with good conservation properties. *J. Comput. Phys.*, 229 (2009), 1043–1076.

[21] Choudhari, M. M., and Khorrami, M. R. Slat Cove Unsteadiness: Effect of 3D Flow Structures. *AIAA 200–0211* (2006), 0211.

[22] Choudhari, M. M., and Khorrami, M. R. Effect of Three-Dimensional Shear-Layer Structures on Slat Cove Unsteadiness. *AIAA 45*, 9 (2007), 2174–2186.

[23] Chung, M.-H. Cartesian cut cell approach for simulating incompressible flows with rigid bodies of arbitrary shape. *Comput. Fluids. 35*, 6 (2006), 607–623.

[24] Chyu, C. K., and Rockwell, D. Near-wake structure of an oscillating cylinder: effect of controlled shear-layer vortices. *J. Fluid Mech. 322* (1996), 21–49.

[25] Clark, R., Ferziger, J., and Reynolds, W. Evaluation of subgrid-scale models using an accurately simulated turbulent flow. *J. Fluid Mech. 91* (1979), 1–16.

[26] Clarke, D., Salas, M., and Hassan, H. Euler calculations for multi-element airfoils using cartesian grids. *AIAA 24*, 3 (1986), 353–358.

[27] Colella, P., Graves, D., Modiano, D., Puckett, E. G., and Sussman, M. An embedded boundary/volume of fluid method for free surface flows in irregular geometries. 3rd ASME/JSME Joint Fluids Engineering Conference, San Francisco, USA, July 1999. ASME/JSME.

[28] Courant, R. L. Variational Methods for the Solution of Problems of Equilibrium and Vibration. *Bulletin of the American Mathematical Society 49* (1943), 1–23.

[29] Coutanceau, M., and Bouard, R. Experimental determination of the main features of the viscous flow in the wake of a circular cylinder in uniform translation. *J. Fluid Mech 79*, 2 (1977), 231–256. Part 1. Steady flow.

[30] Davis, R. M., and Moore, E. F. A numerical study of vortex shedding from rectangles. *J. Fluid Mech. 116* (1982), 475–506.

[31] Deck, S. Zonal-Detached-Eddy Simulation of the Flow Around a High-Lift Configuration. *AIAA 43* (2005), 2372–2384.

[32] Dennis, S. C. R., and Chang, G. Numerical solutions for steady flow past a circular cylinder at Reynolds numbers up to 100. *J. Fluid Mech. 42*, 3 (1970), 471–489.

[33] Dillner, B., May, F. W., and McMasters, J. H. Aerodynamics Issues in the Design of Highlift Systems for Transport Aircraft. *AGARD 9* (1984).

[34] Dong, S., Karniadakis, G. E., and Rockwell, A. E. D. Combined direct numerical simulation particle image velocimetry study of the turbulent air wake. *J. Fluid Mech. 569* (2006), 185–207.

[35] Dröge, M. *Cartesian Grid Methods for Turbulent Flow Simulation in Complex Geometries*. PhD thesis, University of Groningen, 2007.

[36] Dröge, M., and Verstappen, R. A new symmetry-preserving cartesian-grid method for computing flow past arbitrarily shaped objects. *Int. J. Numer. Meth. Fluids 47*, 8–9 (2005).

[37] Ehrenfried, K. Processing calibration-grid images using the hough transformation. *Meas. Sci. Technol. 13*, 7 (2002), 975–983.

[38] Euler, L. Principes généraux du mouvement des fluides. *Hist. l'Acad. Roy. Sci. et belles lettres 11* (1757), 274–315.

[39] Fefferman, C. L. Existence and Smoothness of the NavierStokes Equation. online, `http://www.claymath.org/millennium/Navier-Stokes_Equations`.

[40] Ferziger, J. H., and Peric, M. *Computational methods for fluid dynamics*, third ed. Springer-Verlag, Berlin, 2002.

[41] Fey, U., König, M., and Eckelmann, H. A new Strouhal-Reynolds-number relationship for the circular cylinder in the range $47 < re < 2 \cdot 10^5$. *Phys. Fluids. 10*, 7 (1998), 1547–1549.

[42] Flaig, A., and Hilbig, R. *High-Lift Design for Large Civil Aircraft.* AGARD, 1993, pp. 31–31.

[43] Fornberg, B. *A practical guide to pseudospectral methods.* Cambridge University Press, Cambridge, 1998.

[44] Franke, J., and Frank, W. Large edy simulation of the flow past a circular cylinder at $re_d = 3900$. *J. Wind Eng. Ind. Aerod. 90*, 10 (2002), 1191–1206.

[45] Franke, R., Rodi, W., and Schönung, B. Numerical Calculation of Laminar Vortex Shedding Flow Past Cylinders. *J. Wind. Eng. Ind. Aerod. 35* (1990), 237–257.

[46] Frink, N. T. Assessment of an Unstructured-Grid Method for Predicting 3-D Turbulent Viscous Flows. *AIAA 96*, 0292 (1997), 1–11.

[47] Fröhlich, J. *Large Eddy Simulation turbulenter Strömungen*, first ed. B. G. Teubner Verlag, Wiesbaden, September 2006.

[48] Fröhlich, J., Mellen, C., Rodi, W., Temmerman, L., and Leschziner, M. Highly resolved large-eddy simulation of separated flow in a channel with streamwise periodic constrictions. *J. Fluid Mech. 526* (2005), 19–66.

[49] Fröhlich, J., Rodi, W., Kessler, P., S. Parpais, J. P. B., and Laurence, D. *Large eddy simulation of flow around circular cylinders on structured and unstructured grids*, first ed., vol. 66 of *in CNRS DFG Collaborative Research Programme.* Vieweg, Braunschweig, 1998. pp. 319–338.

[50] Fröhlich, J., and v. Terzi, D. Hybrid LES/RANS methods for the simulation of turbulent flows. *Prog. Aerosp. Sci. 44* (2008), 349–77.

[51] Furman, A., and Breitsamter, C. Experimental investigations on the VFE-2 configuration at TU munich, germany. *RTO-TR-AVT RTO-TR-AVT-113*, 21 (2008), 1–47.

[52] Gosman, A. D. Developments in CFD for industrial and environmental applications in wind engineering. *Journal of Wind Engineering and Industrial Aerodynamics 81*, 1-3 (1999), 21 – 39.

[53] Gottlieb, D., and Orszag, S. A. *Numerical analysis of spectral methods: Theory and Applications*. Society for Industrial and Applied Mathematics, Philadelphia, 1977.

[54] Gray, A., Abbena, E., and Salamon, S. *Modern Differential Geometry of Curves and Surfaces with Mathematica*, third ed. Chapman and Hall/CRC, 2006. in §12.7.

[55] Griffith, B., and Peskin, C. S. On the order of accuracy of the immersed boundary method: higher order convergence rates for sufficiently smooth problems. *J. of Comput. Phys. 208*, 1 (2005), 75–105.

[56] Grove, A. S., Shair, F. H., Petersen, E. E., and Acrivos, A. An experimental investigation of the steady separated flow past a circular cylinder. *J. Fluid Mech. 19* (1964), 60–80.

[57] Ham, F. E., Lien, F. S., and Strong, A. B. A fully conservative second-order finite difference scheme for incompressible flow on nonuniform grids. *J. Comput. Phys. 177* (2002), 117–133.

[58] Harten, A., Engquist, B., Osher, S., and Chakravarthy, S. Uniformly high order accurate essentially non-oscillatory schemes iii. *J. Comput. Phys. 71* (1987), 231–303.

[59] Hartmann, D., Meinke, M., and Schröder, W. An adaptive multilevel multigrid formulation for cartesian hierarchical grid methods. *Comput. Fluids 37*, 9 (2008), 1103–1125.

[60] He, X., and Luo, L. S. Theory of the lattice boltzmann method: From the boltzmann equation to the lattice boltzmann equation. *Phys. Rev. E 56*, 6 (1997), 6811–6817.

[61] Henderson, R. D. Details of the drag curve near the onset of vortex shedding. *Phys. Fluids 7*, 9 (1995), 2102–2104.

[62] Hickel, S., and Adams, N. A. On implicit subgrid-scale modeling in wall-bounded flows. *Phys. Fluids 19*, 10 (2007), 105106–105108.

[63] Hickel, S., and Adams, N. A. Implicit les applied to zero-pressure-gradient and adverse-pressure-gradient boundary-layer turbulence. *Int. J. Heat Fluid Flow 29*, 3 (2008), 626–639.

[64] Hickel, S., Adams, N. A., and Domaradzki, J. A. An adaptive local deconvolution method for implicit LES. *J. of Comput. Phys. 213*, 1 (2006), 413–436.

[65] Hickel, S., Kempe, T., and Adams, N. A. Implicit large-eddy simulation applied to turbulent channel flow with periodic constrictions. *Theor. and Comput. Fluid Dyn. 22*, 3 (2007), 227–242.

[66] Hickel, S., and N. A. Adams, N. N. M. Implicit subgrid-scale modeling for large-eddy simulation of passive-scalar mixing. *Phys. Fluids 19*, 9 (2007), 095102–095114.

[67] Hickel, S., v. Terzi, D., and Frhlich, J. *An adaptive local deconvolution method for general curvilinear coordinate systems. Advances in Turbulence*. Springer-Verlag, Berlin, 2008.

[68] Hinterberger, C. *Dreidimensionale und tiefengemittelte Large-Eddy-Simulation von Flachwasserströmungen*. PhD thesis, University of Karlsruhe, 2004.

[69] Hu, X. Y., Khoo, B. C., Adams, N. A., and Huang, F. L. A conservative interface method for compressible flows. *J. Comput. Phys. 219*, 2 (2006), 553–578.

[70] Jakirlic, S., Jester-Zrker, R., and Tropea, C. Workshop on refined flow modeling. 9th ERCOFTAC/IAHR/COST, 2001. Darmstadt University of Technology, Germany.

[71] Jenkins, L. N., Khorrami, M. R., and Choudhari, M. M. Characterization of Unsteady Flow Structures near Leading-Edge Slat: Part I. PIV Measurements. *AIAA 2004-2802* (2004).

[72] Jimenéz, J., and Moser, R. Large Eddy Simulation: Where are we and what can we expect. vol. 38 of *4*, AIAA, American Institute of Aeronautics and Astronautics, Reston, VA, USA, pp. 605–612.

[73] Johannsen, H., and Collela, P. A Cartesian Grid Embedded Boundary Method for Poisson's Equation on Irregrular Domains. *J. Comput. Phys. 147*, 1 (1990), 60–85.

[74] Kang, S., Iaccarino, G., and Moin, P. Accurate Immersed-Boundary Reconstructions for Viscous Flow Simulations. *AIAA 47*, 7 (2009), 1750–1760.

[75] Khorrami, M. R., Choudhari, M. M., and Jenkins, L. N. Characterization of Unsteady Flow Structures Near Leading-Edge Slat: PartII. 2D Computations. *AIAA*, 2004–2802 (2004).

[76] Khorrami, M. R., Singer, B. A., and Lockard, D. P. Time-Accurate Simulations and Acoustic Analysis of Slat Free-Shear Layer: Part II. *AIAA*, 2002–2579 (2002).

[77] Kim, J., Kim, D., and Choi, H. An immersed-boundary finite-volume method for simulations of flow in complex geometries. *J. Comput. Phys. 171*, 1 (2001), 132–150.

[78] Kirkpatrick, M., Armfield, S., and Kent, J. A representation of curved boundaries for the solution of the Navier-Stokes equations on a staggered three-dimensional cartesian grid. *J. Comput. Phys. 184*, 1 (2003), 1–36.

[79] Kolmogorov, A. N. The local structure of turbulence in incompressilbe viscous fluid for very large Reynolds numbers. *Dokl. Adad. Nauk SSSR*, 30 (1941), 299–303. in Russian.

[80] Kolmogorov, A. N. The local structure of turbulence in incompressilbe viscous fluid for very large Reynolds numbers. *Proc. R. Soc. London Ser. A*, 434 (1991), 9–13.

[81] Kompenhans, J., Raffel, M., Dieterle, L., Dewhirst, T., Vollmers, H., Ehrenfried, K., Willert, C., K, P., Khler, C. J., Schrder, A., and Ronneberger, O. Particle Image Velocimetry in Aerodynamics: Technology and Applications in Wind Tunnels. *J. Visualization 2* (2000), 229–244.

[82] Kravchenko, A., and Moin, P. Numerical studies of flow over a circular cylinder at $Re_d = 3900$. *Phys. Fluids 12*, 2 (2000), 403–417.

[83] Lai, M., and Peskin, C. S. An immersed boundary method with formal second-order accuracy and reduced numerical viscosity. *J. of Comput. Phys. 160*, 2 (2000), 705–19.

[84] Lax, P. D., and Richtmyer, R. D. Survey of the stability of linear finite difference equations. *Comm. Pure Appl. Math. 9* (1956), 267–293.

[85] Leray, J. Sur le mouvement d'un liquide visqueux emplissant l'espace. *Acta Math.*, 63 (1934), 193–248.

[86] Lockard, D. P., and Choudhari, M. M. Noise Radiation from a Leading-Edge Slat. *AIAA Conference,*, 2009-2101 (2009). Miami Florida.

[87] Lorensen, W. E., and Cline, H. E. Marching cubes: a high resolution 3D surface construction algorithm. *Computer Graphics, 21*, 4 (1987), 163–169.

[88] Lourence, D. *Large Eddy Simulation of industrial flows?* Closure Strategies for Turbulent and Transitional Flows. Cambridge University Press, Cambridge, 2002.

[89] Lourenco, L. M., and Shih, C. Characteristics of the plane turbulent near wake of a circular cylinder, a particle image velocimetry study. Unpublished results, data extracted from Dröge PhD thesis.

[90] Ludwieg, H. Zur Erklärung der Instabilität der bei angestellten Deltaflügeln auftretenden freien Wirbelkerne. *Z. Flugwiss. 10*, 3 (1962), 242–249.

[91] Ma, X., Karamanos, G.-S., and Karniadakis, G. E. Dynamics and low-dimensionality of a turbulent near wake. *J. Fluid Mech. 410* (2000), 29–65.

[92] Mahesh, K., Constantinescu, G., and Moin, P. A numerical method for Large-Eddy Simulation in complex geometries. *J. Comput. Phys. 197* (2004), 215–240.

[93] Manceau, R., Leschziner, J. P. B. M. A., and Menter, F. Workshop on refined flow modeling. 10th Joint ERCOFTAC(SIG-15)/IAHR/QNET-CFD, 2002. Universit de Poitiers, France.

[94] Mansy, H., Yang, P., and Williams, D. R. Quantitative measurements of three-dimensional structures in the wake of a circular cylinder. *J. Fluid Mech. 280* (1994), 277–296.

[95] Mark, A., and van Wachem, B. G. M. Derivation and validation of a novel implicit second-order accurate immersed boundary method. *J. Comput. Phys. 227*, 13 (2008), 6660–6680.

[96] Mary, I. Large eddy simulation of vortex breakdown behind a delta wing. *Int. J. Heat Fluid Flow 24*, 4 (2003), 596–605. Selected Papers from the Fifth International Conference on Engineering Turbulence Modelling and Measurements.

[97] Meier, H. F., Alves, J. J. N., and Mori, M. Comparison between staggered and collocated grids in the finite-volume method performance for single and multi-phase flows. *Computers and Chemical Engineering 23*, 3 (1999), 247 – 262.

[98] Mellen, C. P., Fröhlich, J., and Rodi, W. Large-eddy simulation of the flow over periodic hills. M. Deville and R. Owens, Eds., 16th IMACS world congress, August 2000. Lausanne, Switzerland.

[99] Mercier, B. *An introduction to the numerical analysis of spectral methods.* Springer-Verlag, Berlin, 1989.

[100] Meyer, M., Devesa, A., Hickel, S., Hu, X., and Adams, N. A conservative immersed interface method for large-eddy simulation of incompressible flows. *J. Comput. Phys. 229* (2010), 6300–6317.

[101] Meyer, M., Hickel, S., and Adams, N. Assessment of implicit large-eddy simulation with a conservative immersed interface method for turbulent cylinder flow. *Int. J. Heat Fluid Flow 31*, 3 (2010), 368–377.

[102] Meyer, M., Hickel, S., and Adams, N. A. Computational Aspects of Implicit LES ofComplex Flows. In *High Performance Computing in Science and Engineering, Garching/Munich 2009*, S. Wagner, M. Steinmetz, A. Bode, and M. M. Mller, Eds. Springer Berlin Heidelberg, 2010, pp. 133–146.

[103] Mittal, R., and Iaccarino, G. Immersed Boundary Methods. *Annual Review of Fluid Mechanics 37*, 1 (2005), 239–261.

[104] Mittal, R., and Moin, P. Suitability of upwind biased schemes for Large-Eddy Simulation. *AIAA 30*, 8 (2005), 1415–1417.

[105] Mittal, R., Seshadri, V., and Udaykumar, H. S. Flutter, tumble and vortex induced autorotation. *Theor. Comp. Fluid Dyn. 17*, 3 (2004), 165–70.

[106] Mittal, R., Utturkar, Y., and Udaykumar, H. S. Computational modeling and analysis of biomimetic flight mechanisms. *AIAA*, 2002–0865 (2002).

[107] Moens, F. CFD Prediction of Maximum Lift of a 2D High Lift Configuration. *proceedings Katnet/GARTEUR Highlift Workshop 44* (2002).

[108] Mohd-Yusof, J. Combined immersed-boundary/B-spline methods for simulations of flow in complex geometries. *Annual Research Briefs Center for Turbulence Research Stanford University* (1997), 317–328.

[109] Moriarty, P. J., and Heineck, J. T. PIV Measurements Near a Leading-Edge Slat. 3rd International Workshop on PIV, Santa Barbara, USA, September 1999. University of Santa Barbara.

[110] Morinishi, Y., Lund, T. S., Vasilyev, O. V., and Moin, P. Fully conservative higher order finite difference schemes for incompressible flow. *J. Comput. Phys.*, 143 (1998), 90–124.

[111] Muldoon, F., and Acharya, S. A divergence-free interpolation scheme for the immersed boundary method. *Int. J. Numer. Methods Fluids 56* (2008), 1845–1884.

[112] Navier, C. L. M. H. Sur les lois du mouvement des fluides. *Mèmoires de l'Acadèmie royale des Sciences de l'Institut de France*, 6 (1823), 389.

[113] Neitzke, K. P. Using Advanced Measurement Techniques in High Lift Validation Experiments. Aerospace Aerodynamics Research Conference, London, England, June 2003. Royal Aerospace Society.

[114] Nishino, T., Roberts, G. T., and Zhang, X. Unsteady RANS and detached-eddy simulations of flow around a circular cylinder in ground effect. *J. Fluids Struct.*, 24 (2008), 18–33.

[115] Nogueira, X., Khelladi, S., Colominas, I., Cueto-Felgureroso, L., Paris, J., and Gomez, H. High-Resolution Finite Volume Methods on Unstructured Grids for Turbulence and Aeroacoustics. *Arch. Comput. Method E.*, 18 (2011), 315–340.

[116] Norberg, C. Experimental investigation of the flow around a circular cylinder: influence of aspect ratio. *J. Fluid Mech.*, 258 (1994), 287–316.

[117] Okajima, A. Strouhal numbers of rectangular cylinders. *J. Fluid Mech. 123* (1982), 379–398.

[118] Ong, L., and Wallace, J. The velocity field of the turbulent very near wake of a circular cylinder. *Exp. Fluids 20*, 6 (1996), 441–453.

[119] Osher, S., and Fedkiw, R. *Level Set Methods and Dynamic Implicit Surfaces*, vol. 79. Springer-Verlag, 2003.

[120] Osher, S., and Sethian, J. A. Fronts Propagating with Curvature Dependent Speed: Algorithms Based on Hamilton-Jacobi Formulations. *J. Comput. Phys. 79*, 1 (1988), 12–49.

[121] Owen, S. J. A Survey of Unstructured Mesh Generation Technology. online, `http://citeseerx.ist.psu.edu/viewdoc/summary?doi=10.1.1.34.5079`. Department of Civil and Environmental Engineering, Carngie Mellon University, Pittsburgh, USA.

[122] Panton, R. L. *Incompressible Flows*, first ed. Wiley-Interscience, New York, 1984.

[123] Park, N., Yoo, J., and Choi, H. Discretization errors in Large Eddy Simulation: on the suitability of centered and upwind-biased compact difference schemes. *J. Comput. Phys. 198* (2004), 580–616.

[124] Parnaudeau, P., Carlier, J., Heitz, D., and Lamballais, E. Experimental and numerical studies of the flow over a circular cylinder at Reynolds number 3900. *Phys. Fluids 20*, 8 (2008), 085101–1–085101–14.

[125] Paschal, K., Jenkins, L., and Yao, C. Unsteady Slat-Wake Characteristics of a High-Lift Configuration. *AIAA*, 2000–0139 (2000), 0139.

[126] Peller, N., Duc, A. L., Tremblay, A., and Manhart, M. High-order stable interpolations for immersed boundary methods. *J. Numer. Methods in Fluids 52*, 11 (2006), 1175–1193.

[127] Peng, S. H., and Haase, W. *Advances in Hybrid RANS-LES Modelling*. Springer-Verlag, 2008.

[128] Perot, J. B. Discrete Conservation Properties of Unstructured Mesh Schemes. *Annual Review of Fluid Mechanics 43*, 1 (2011), 299–318.

[129] Peskin, C. S. *Flow patterns around heart valves: a digital computer method for solving the equations of motion*. PhD thesis, Albert Einstein College of Medicine, Bronx, 1972.

[130] Peskin, C. S. Numerical analysis of blood flow in the heart. *J. of Comput. Phys. 25* (1977), 220.

[131] Piomelli, U., and Balaras, E. Wall-layer models for large-eddy simulation. *Ann. Rev. Fluid Mech. 34* (2002), 349–374.

[132] Pope, S. B. *Turbulent Flows*, first ed. Cambridge University Press, Cambridge, 2000.

[133] Prandtl, L. Der Luftwiderstand von Kugeln. *Nachr. Ges. Wiss. Göttingen* (1914), 177–190.

[134] Rapp, C. *Experimentelle Studie der turbulenten Strömung ueber periodische Hügel*. PhD thesis, Technische Universität München, München, 2008.

[135] Reckzeh, D. Aerodynamic design of the high-lift-wing for a Megaliner aircraft. *Aerospace Science and Technology 7*, 2 (2003), 107 – 119.

[136] Reckzeh, D., and Hansen, H. *High Reynolds-Number Windtunnel Testing for the Design of Airbus High-Lift Wings*. Springer-Verlag, Berlin/ Heidelberg, 2006.

[137] Roma, A., Peskin, C. S., and Berger, M. An adaptive version of the immersed boundary method. *J. of Comput. Phys. 153*, 2 (1999), 509–34.

[138] Roux, J. P., Guillen, P., Sagaut, P., Lirvat, J., Chen, H., Belanger, A., and Shock, R. VLES of the Unsteady Flow Around a High Lift Wing Based on the Lattice Boltzmann Method. *EuroMech Colloquium*

449, Computational AeroAcoustics: From Acoustic Sources Modeling to Far-Field Radiated Noise Prediction (2003).

[139] Rumsey, C. L., Gatski, T. B., Ying, S. X., and Bertelrud, A. Prediction of High-Lift Flows Using Turbulent Closure Models. *AIAA 36* (1998), 765–773.

[140] Rumsey, C. L., and Ying, S. X. Prediction of High Lift: Review of Present CFD Capability. *Progress in Aerospace Sciences 38* (2002), 145–1801.

[141] Saric, S., Jakirlic, S., Breuer, M., Jaffrzic, B., Deng, G., and Chikhaoui, O. Evaluation of detached-eddy simulations for predicting the flow over periodic hills. E. Cancs and J. F. Gerbeau, Eds., ESAIM Proceedings CEMRACS 2005 (Centre dt Mathmatique de Recherche Avance en Calcul Scientifique), pp. 133–45. Computational aeroacoustics and computational fluid dynamics in turbulent flows.

[142] Shu, C.-W. Total-variation-diminishing time discretizations. *SIAM J. Sci. Stat. Comput. 9*, 6 (1988), 10731084.

[143] Shur, M., Spalart, P., Strelets, M., and Travin, A. A hybrid RANS-LES approach with delayed-DES and wall-modelled LES capabilities. *Int. J. Heat Fluid Flow 29*, 6 (2008), 1638–1649.

[144] Shur, M. L., Spalart, P. R., Squires, K. D., Strelets, M., and Travin, A. Three-dimensionality in unsteady Reynolds-averaged Navier-Stokes simulations of two-dimensional geometries. *AIAA*, 43 (2005), 1230–42.

[145] Simon, F., Deck, S., Guillen, P., Sagaut, P., and Merlen, A. Numerical simulation of the compressible mixing layer past an axisymmetric trailing edge. *J. Fluid Mech.*, 591 (2007), 215–53.

[146] Sleijpen, G. L. G., van der Vorst, H. A., and Fokkema, D. R. BiCGstab(l) and other hybrid Bi-CG methods. *Numerical Algorithms*, 7 (1994), 75–109.

[147] Slimon, S. Computation of internal separated flows using a zonal detached eddy simulation approach. ASME Int. Mech. Eng. Congr., pp. IMECE2003–43881.

[148] Smagorinsky, J. General circulation experiments with the primitive equations. *Mon. Weath. Rev. 91* (1963), 99–164.

[149] Smith, A. M. O. High-Lift Aerodynamics. *Numerical Algorithms 12*, 6 (1994), 501–530.

[150] Sohankar, A., Norberg, C., and Davidson, L. Low-Reynolds-number flow around a square cylinder at incidence: study of blockage, onset of vortex shedding and outlet boundary condition. *Int. J. Numer. Meth. Fluid 26*, 1 (1998), 39–56.

[151] Sommerfeld, A. Ein Beitrag zur hydrodynamischen Erklärung der turbulenten Flüssigkeitsbewegung. 5th Int. Congr. Math., 1908. Rome, Italy.

[152] Spalart, P. R. Detached-Eddy Simulation. *Annu. Rev. Fluid Mech. 41* (2009), 181202.

[153] Spalart, P. R., Deck, S., Shur, M. L., Squires, K. D., Strelets, M. K., and Travin, A. A new version of detached-eddy simulation, resistant to ambiguous grid densities. *Theor. Comp. Fluid Dyn. 20* (2006), 181–95.

[154] Stockie, J. M., and Wetton, B. R. Analysis of stiffness in the immersed boundary method and implications for time-stepping schemes. *J. Comput. Phys. 154*, 1 (1998), 41–64.

[155] Stokes, G. G. On the theories of the internal friction of fluids in motion, and of the equilibrium and motion of elastic solids. *Cambridge Philos. Soc. Trans.*, 8 (1845), 287–319.

[156] Strelets, M. Detached eddy simulation of massively separated flow. AIAA Aerosp. Sci. Meet. Exhib., 2001.

[157] Szepessy, S., and Bearmann, P. W. Aspect ratio and end plate effects on vortex shedding from a circular cylinder. *J. Fluid Mech.*, 234 (1992), 191.

[158] Takeda, K., and G. B. Aschcrott, X. Zhang, P. A. N. Unsteady Aerodynamics of Flap Cove Flow in a High-Lift Device Configuration. *AIAA 115*, 1 (2001), 2001–0707.

[159] Tau, E. Y. A second-order projection method for the incompressible Navier-Stokes equations in arbitrary domains. *J. Comput. Phys. 115*, 1 (1994), 147–152.

[160] Temmerman, L., and Leschziner, M. A. *Large-eddy simulation of separated flow in a streamwise periodic channel constriction.* Second international symposium turbulence and shear flow phenomena. Stockholm, Sweden, June 2001.

[161] Temmerman, L., Leschziner, M. A., Mellen, C. P., and Frhlich, J. Investigation of wallfunction approximations and subgrid-scale models in large-eddy simulation of separated flow in a channel with periodic constrictions. *Int. J. Heat Fluid Flow 24* (2003), 157–80.

[162] Thibert, J. J., Reneaux, J., Moens, F., and Priest, J. ONERA Activities on High Lift Devices for Transport Aircraft. *Aeronaut. J. 99*, 989 (1995), 395–411.

[163] Thom, A. Numerical solution for the flow around a cylinder at Reynolds numbers of 40, 200 and 500. *Proc. Roy. Soc. 141* (1933), 651–669.

[164] Thom, A., and Apelt, C. J. *Field Computations in Engineering and Physics.* Vab Nostrand, London, 1961.

[165] Tran, D. *Comparison of Numerical Simulation of the Flow around an Airfoil in High Lift Configuration with PIV Experiments Results*, first ed. Springer-Verlag, Berlin, 2003. EUROPIV2 Image Velocimetry.

[166] Travin, A., Shur, M., Strelets, M., and Spalart, P. R. Detached-eddy simulations past a circular cylinder. *Flow Turbul. Combust. 63* (2000), 293–313.

[167] Tritton, D. J. Experiments on the flow past a circular cylinder at low Reynolds number. *J. Fluid. Mech. 6* (1959), 547–567.

[168] Tseng, Y.-H., and Ferziger, J. A ghost-cell immersed boundary method for flow in complex geometry. *J. Comput. Phys. 192*, 2 (2003), 593–623.

[169] Tucker, P. G., and Pan, Z. A cartesian cut cell method for incompressible viscous flow. *Appl. Math. Modell 24*, 8–9 (2000), 591–606.

[170] Udaykumar, H. S., Mittal, R., Rampunggoon, P., and Khanna, A. A sharp interface cartesian grid method for simulating flows with complex moving boundaries. *J. Comput. Phys. 174*, 1 (2001), 345–380.

[171] Udaykumar, H. S., Mittal, R., and Shyy, W. Computation of solid-liquid phase fronts in the sharp interface limit on fixed grids. *J. Comput. Phys. 153*, 2 (1999), 534–574.

[172] Udaykumar, H. S., Shyy, W., and Rao, M. M. Mixed Eulerian-Lagrangian method for fluid flows with complex and moving boundaries. *Int. J. Numer. Meth. Fl. 22*, 8 (1996), 691–705.

[173] van Dam, C. P. The aerodynamic design of multi-element high-lift systems for transport airplanes. *Prog. Aerosp. Sci. 38* (2002), 101–144.

[174] van der Vorst, H. Bi-CGSTAB: A fast and smoothly converging variant of Bi-CG for the solution of nonsymmetric linear systems. *SIAM J. Sci. Statist. Comput. 13*, 631-644 (1992).

[175] Verstappen, R. W. C. P., and Veldman, A. E. P. *Fourth-order DNS of flow past a square cylinder at Re* = 22000, first ed. First results, in Direct and Large-Eddy Simulation II. Kluwer Academic Publishers, Dordrecht, 1997.

[176] Verstappen, R. W. C. P., and Veldman, A. E. P. Symmetry-preserving discretization of turbulent flow. *J. Comput. Phys.*, 187 (2003), 343–368.

[177] Verzicco, R., Mohd-Yusof, J., Orlandi, P., and Haworth, D. Les in complex geometries using boundary body forces. *AIAA 38*, 3 (2000), 427–433.

[178] Werner, H. *Grobstruktursimulation der turbulenten Strömung uber eine querliegende Rippe in einem Plattenkanal bei hoher Reynoldszahl.* PhD thesis, Technische Universität München, München, 1991.

[179] Williamson, C. H. K., Wu, J., and Sheridan, J. Scaling of streamwise vortices in wakes. *Physics of Fluids 7*, 10 (1995), 2307–2309.

[180] Winkler, C. M., Dorgan, A. J., and Mani, M. The Effect of Unstructured Grid Topology and Resolution on Simulations of Decaying Turbulence.

27th International Congress of the Aeronautical Sciences (ICAS), September 2010. Nice, France.

[181] Woodward, D. S., and Lean, D. E. Awhere is High-Lift Today? A Review of Past UK Research Programmes. High-Lift System Aerodynamics, AGARD CP-515, September 1993. Neuilly-sur-Seine, France.

[182] Ye, T., Mittal, R., Udaykumar, H. S., and Shyy, W. An accurate Cartesian grid method for viscous incompressible flows with complex immersed boundaries. *J. Comput. Phys. 156*, 2 (1999), 209–240.